UiO : University of Oslo

Henrik Andersen Sveinsson

Molecular dynamics modeling of mechanical failure processes in methane hydrates

Thesis submitted for the degree of Philosophiae Doctor

Faculty of Mathematics and Natural Sciences

2019

Series of dissertations submitted to the
Faculty of Mathematics and Natural Sciences, University of Oslo
No. 2179

ISSN 1501-7710

Cover: Hanne Baadsgaard Utigard.
Print production: Reprosentralen, University of Oslo.

Acknowledgements

The work with this thesis was carried out at the NJORD Centre at the Department of Physics at the University of Oslo from 2015 to 2019. The research presented here was conducted under the supervision of professor Anders Malthe-Sørenssen and funded by the Research Council of Norway.

I first met Anders when attending the introductory mechanics course on the first year of my Bachelor studies. Anders offered an extracurricular project on understanding dry friction, which I chose to participate in (that turned out to be a good choice). Therefore, prior to working on this thesis, I was sort of "PhD preschooled", working with Jørgen Kjoshagen Trømborg, Kjetil Thøgersen, David Skålid Amundsen, Julien Scheibert and Anders on understanding the onset of frictional slip. I thank you all for including me as a real member of your research group at such an early stage of my university studies. A special thanks to Kjetil, whom I have shared an office with for the better part of the last four years, for listening to me while babbling to structure my own thoughts, and for being clever enough to sometimes understand it and make good suggestions.

I have worked with Anders Malthe-Sørenssen ever since I was introduced to the friction project, and I particularly enjoy the increasing independence that Anders has facilitated. He contributes conceptual advice and ideas, but expects that I am the expert of the details, and trusts me to figure them out. As it appears to me, he has gradually pushed me towards becoming an independent researcher, by transitioning from supervising to mentoring. Anders has also always been willing to engage in and initiated conversations about what steps to take in order to pursue an academic career.

Anders Hafreager, thank you for endless hours of pair programming and discussions in front of blackboards to figure out mostly things about crystals (and percolation and whatever). You keep questions coming until we figure it out, for real, no cheating. And I really appreciated our research trips to University of Southern California. I would give a lot to recreate the feeling of stepping out of LAX in 2017 with the prospect of weeks of physics–programming–LA-time. I am sure we'll find projects to work on together in the future as well.

Marthe Guren for diligently trying ever new ideas to make hydrated periclase stable in MD simulations. We have learned valuable lessons from this, and it has been particularly useful for my crystal structure intuition. You weren't the only one needing a paper-cube crystal.

Carl Korsnes for insisting I was made for physics and not business administration[1], and generally for engaging in discussions about whatever aspects of life, philosophy and the universe.

[1] I actually started business administration, but Carl was right (as were others, but Carl put it most bluntly, and who knows what tipped the scales).

Dannelsesprogrammet for giving me the opportunity to think and talk about why I do what I do, what to do and how to be, and thereby navigating the difference between scientific performance and scientific discovery (both have their place). And for a thorough treatment of Stoicism just at the right time. But I will enjoy a couple of months with Epicurus now.

Fulong Ning for inviting me to Wuhan and for helpful discussions and suggestions about hydrates. Pinqiang Cao and Bin Fang for taking care of me every single day when I visited China, and for our collaboration on hydrate simulations, which I hope continues in the coming years.

The CACS group at University of Southern California, and in particular Rajiv Kalia, Aiichiro Nakano and Priya Vashishta for welcoming us several times to Los Angeles for research visits, for generously sharing research ideas for studying faceting of silicon carbide nanoparticles. I have learned a lot from you, in particular about the relation between statistical physics and molecular dynamics simulations.

The Science Library, where I was a physics library person/teacher/developer, for showing me a whole other side of academia, and for simply being an awesome place to work. And for making me think about research data. Section 3.5 is for you.

To my brother Jørgen, my sister Vilde and the rest of my family for always being curious and supporting about what I am doing. And Mamma og Pappa especially, for unconditional support and for having made my life frictionless except where necessary. For always challenging me before and supporting me after choices in life, and for installing the attitude that things should be done well.

Finally, thank you Julie for the fantastic life that we live together. I love you and (this is perhaps why) that we share so deeply an interest in nature and society, and what is wrong and right about them. This leads to endless enriching and enjoyable conversations. I look forward to our new life with (working title) Bjørnstjerne, who at the time of writing is kindly staying in the belly awaiting the submission of this thesis.

Henrik Andersen Sveinsson
Oslo, June 26, 2019

Contents

Acknowledgements **i**

Contents **iii**

1 Introduction **1**
1.1 Motivation 1
1.2 Structure of this thesis 2

2 Gas hydrates **5**
2.1 Basic physical properties 5
2.2 Gas hydrates in nature 6
2.3 Hydrate nucleation 10
2.4 Experiments with relevance to gas hydrate decomposition and mechanics 11
2.5 Molecular modeling of gas hydrate mechanics 14
2.6 Outstanding questions 16
2.7 A couple of related topics: Onset of dry friction and faceting of silicon carbide 16

3 Molecular dynamics simulations and analysis **19**
3.1 Interatomic potentials and choice of potential. 19
3.2 Building polycrystals 23
3.3 Analyzing particle trajectories 23
3.4 Micro-automation 24
3.5 Replicability and data management 26

4 Summary of papers **29**
4.1 Paper I 29
4.2 Paper II 30
4.3 Paper III 31
4.4 Paper IV 33
4.5 Paper V 33

5 Outlook **35**

Bibliography **37**

Papers **46**

I Molecular-scale thermally activated fractures in methane hydrates: A molecular dynamics study **47**

II Grain-size dependent failure behavior of polycrystalline methane hydrates **55**

III Intrinsic differences in strain accommodation mechanisms of ice and gas hydrate bicrystals under shear loading **63**

IV Slow slip and the transition from fast to slow fronts in the rupture of frictional interfaces **79**

V Direct atomic simulations of facet formation and equilibrium shapes of SiC nanoparticles **93**

Chapter 1

Introduction

1.1 Motivation

Gas hydrates are scientifically interesting, technologically and geologically important and aesthetically pleasing. Gas hydrates are ice-like hydrogen bonded crystalline cage structures with guests trapped in the cages. Each cage is comprised of around 20 water molecules and an appreciable proportion of these cages trap either one or two small guest gas molecules [1]. The *methane* hydrate (hydrate with methane as the guest gas) is the most abundantly occurring hydrate in nature. Methane hydrates form out of a methane–water solution at high pressure and moderate to low temperature conditions. Therefore, they can be found under the seabed on the continental slopes, and under the arctic tundra, where these conditions are prevalent. Beyond earth, hydrates have been inferred to exist on icy moons of our solar system [2], and recently they have even been synthesized under interstellar medium conditions [3]. The first gas hydrate (on the reliable experimental record) was synthesized by Humphrey Davy in 1810, but they were regarded as peculiarities until 1934, when Hammerschmidt [4] showed that the snow-like substance occasionally plugging gas pipes were gas hydrates. Only in 1965 was it discovered that gas hydrates occur naturally on earth [5], and eventually estimated that they make up a significant portion of the pore space in sediments on continental slopes [6].

Since gas hydrates can nucleate, agglomerate and form plugs in pipelines, the physical properties of hydrates are important for safe oil and gas flow in pipelines, so-called flow assurance. Moreover, the mechanical strength of hydrates is important for the strength of hydrate-bearing sediments. Therefore, the abundance of gas hydrates in nature makes understanding their mechanical and dissociation properties important for assessing risks of geological hazards such as slope failure, natural blow-outs [7] and methane emissions from hydrate reservoirs. If hydrates *are* released, they may traverse parts of the water columns as a hydrate-crusted methane bubbles, with plate-tectonic-like mechanisms at play on the crust of the bubble [8].

Hydrates offer surprising mechanical behavior, which makes them intrinsically scientifically interesting. Even though hydrates, like ice, are almost purely hydrogen-bonded structures, the mechanical properties of hydrates differ decisively from those of ice. The tensile strengths of hydrates and ice have been measured at similar values in a single experimental setup [9], but hydrates are still an order of magnitude more creep resistant than ice under compression [10] (see Figure 1.1a).

The nucleation kinetics of hydrates involve complex cage-structures, in what has been called the *Hydrate molecular ballet* [11]. At least that's what the author

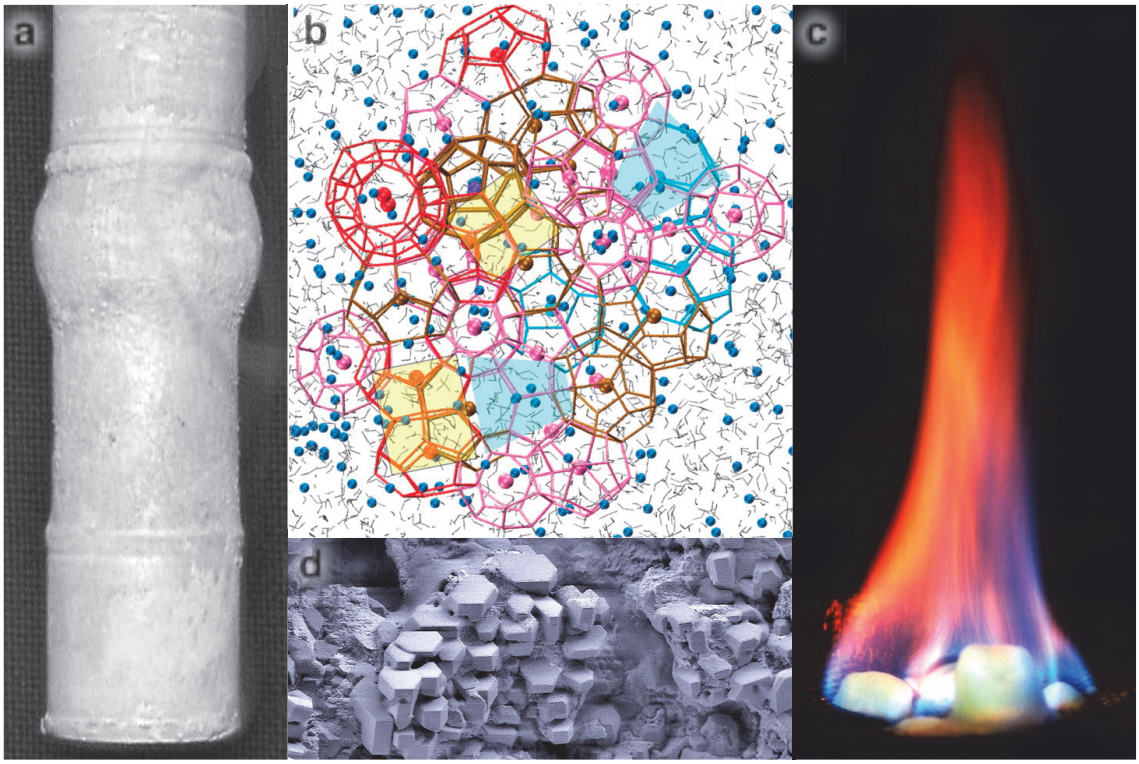

Figure 1.1: (a) Sample of ice and hydrate after compression experiment [10]. The upper part is ice (bulged) and the lower part is hydrate (still perfectly cylindrical). This illustrates the contrast in creep resistance between hydrate and ice. (b) Gas hydrate nucleated in a molecular dynamics simulation [12]. (d) Burning hydrate. (d) Hydrate crystals in a sedimentary matrix. The scale is around 50 microns. Scanning electron microscope. Image permissions and credits: (a) AGU, no permission needed. (b) Reprinted from [12] with permission from The American Association for the Advancement of Science. (c–d) US Geological Survey, public domain.

of the perspective article accompanying the first report of hydrate nucleation in a brute-force molecular dynamics simulation [12] called it. Figure 1.1b shows a molecular configuration from this first nucleation-simulation. In addition to these aesthetically pleasing properties, hydrates have the impressive feature of being a combustible ice, as shown in Figure 1.1c.

One of the challenges in understanding hydrate mechanics (as in many topics) is figuring out the mechanisms acting on the molecular scale, such as the formation and destruction of single hydrate cages, and link them to processes at macroscopic time and spatial scales. There is still no satisfactory explanation for why the mechanical properties of hydrates are so different from those of ice.

The goal of this thesis is to improve the molecular-scale description of mechanical and failure properties of methane hydrates.

1.2 Structure of this thesis

This thesis is structured as follows. In chapter 2 I give a background on gas hydrates, with a focus on mechanical properties, and lay out some outstanding

questions. In chapter 3 I describe briefly the method we use to investigate the molecular-scale processes of gas hydrate mechanics, molecular dynamics simulations. Additionally, chapter 3 describes some software implementations that were not appropriate to describe in the papers. Chapter 4 summarizes the publications that report the research outputs of this thesis. The main story of this thesis is contained in papers I–III, which aim towards answering some of the outstanding questions of chapter 2. Paper IV is an illustration of how up-scaled behavior can be described, and Paper V shows how similar methods can be used to approach a different problem. Finally, chapter 5 provides an outlook.

Chapter 2

Gas hydrates

In this chapter, I give some general background on gas hydrates, and gradually turn the focus toward microscale processes and mechanical properties, to justify that studying hydrate mechanical properties with molecular dynamics simulations is worthwhile.

2.1 Basic physical properties

Gas hydrates are ice-like crystalline substances where a host lattice captures–enclathrates–guest molecules. The lattice is composed of hydrogen-bonded water molecules, and the guests interact with the lattice through van der Waals forces. Gas hydrates are sometimes referred to as "clathrate hydrates" or "clathrates"[1].

Gas hydrates may form in different structures, of which structure I (sI), structure II (sII) and structure H (sH) are the most common. The structure is determined by the temperature and pressure conditions and by the size of the guest molecules [13]. Figure 2.1 shows the cage-network of a hydrate in the sI structure.

Structure I is the most common naturally occurring structure type, and consists of eight cages. Two of the cages are composed of 12 pentagonal faces[2], thus they are dodecahedra. The other six cages are composed of 12 pentagonal faces and 2 hexagonal faces. It is common to use a notation x^y where x is the number of corners in a polygon (eg. 6 for hexagon) and y is the number of such polygons in a cage. The large cage of the sI structure is thus denoted $5^{12}6^2$. Other hydrate structures have other cage combinations, involving other cage types, such as the $5^{12}6^4$ cage in structure II, and $5^{12}6^8$ and $4^35^66^3$ in structure H.

Methane is the most common hydrate former in nature, and thus in geoscience contexts it is common to refer to methane hydrates simply as "gas hydrates" or just "hydrates". Methane forms sI hydrate under the conditions that are relevant in natural gas hydrate reservoirs. Structure II and structure H hydrates have

[1] A clathrate is any guest–host substance. Gas hydrates are clathrates with a water lattice and a gas guest. Technically, we could call them "gas clathrate hydrates". *The* book on hydrates is Sloan, E. D. & Koh, C. a. *Clathrate hydrates of natural gases* (CRC press, 2007), but inside this book, the words "hydrate", "gas hydrate" etc. are used interchangeably where appropriate.

[2] Any polyhedron with exclusively triple-joints must have 12 pentagons. Water prefers tetrahedral coordination, and thus if we consider every water molecule to be a vertex, then 4 edges meet at each vertex. However, only 3 of these belong to any polyhedron. In fact, any unique combination of 3 edges connecting to a water molecule will belong to different polyhedra. Therefore, all polyhedra of clathrates have triple joints, and therefore need to have 12 pentagonal faces.

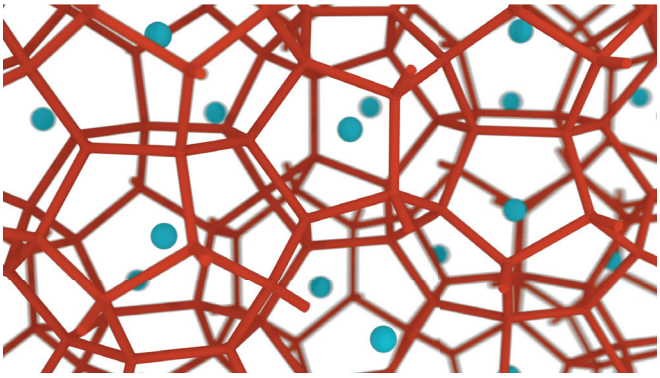

Figure 2.1: Oxygen structure of gas hydrate in the sI structure. Two large, $5^{12}6^2$ cages (left and right) connect to each other through a small 5^{12} cage (the middle). In the sI structure there are 6 large cages for every 2 small cages. There are many other interconnections as well. The $5^{12}6^2$ cage has 14 faces, and thus connects to 14 different cages.

also been found in nature, where a sufficient proportion of thermogenic gas [14, 15] facilitated the formation of these other structures.

Hydrates form out of a solution of water and guest molecules, for example a water–methane solution. They generally need high pressures to be stable, but this criterion can be relaxed by lowering the temperature. At a pressure of 10 MPa, methane hydrates can form at up to around 15°C, while at −5°C they may form at pressures down to 2 MPa [13, p. 7].

2.2 Gas hydrates in nature

Even though the first encounter between humanity and gas hydrates was in the lab, then in pipelines, and only lately (1960's) by the discovery of hydrates in nature, there is now a major interest in naturally occurring hydrates, both for their resource potential and for geological hazard prediction and prevention. Hydrates can typically be found on continental slopes, under offshore arctic permafrost (arctic shallow shelf) and in the arctic tundra [16]. Figure 2.2 shows schematically where hydrates may occur.

2.2.1 On the global inventory of gas hydrates

There have been made numerous estimates of the global gas hydrate inventory over the years, and the high end members of these estimates are often cited. A particular number–the largest one–is the one made by Klauda & Sandler [17] at 74400 gigatons of carbon. This number is an *upper* estimate assuming that what is now thought to be an unrealistically high proportion of pore space in the oceanic gas hydrate stability zone[3] contains hydrate. A more conservative

[3]The oceanic gas hydrate stability zone is the part of the sub-seafloor where the pressure and temperature is compatible with the existence of gas hydrates.

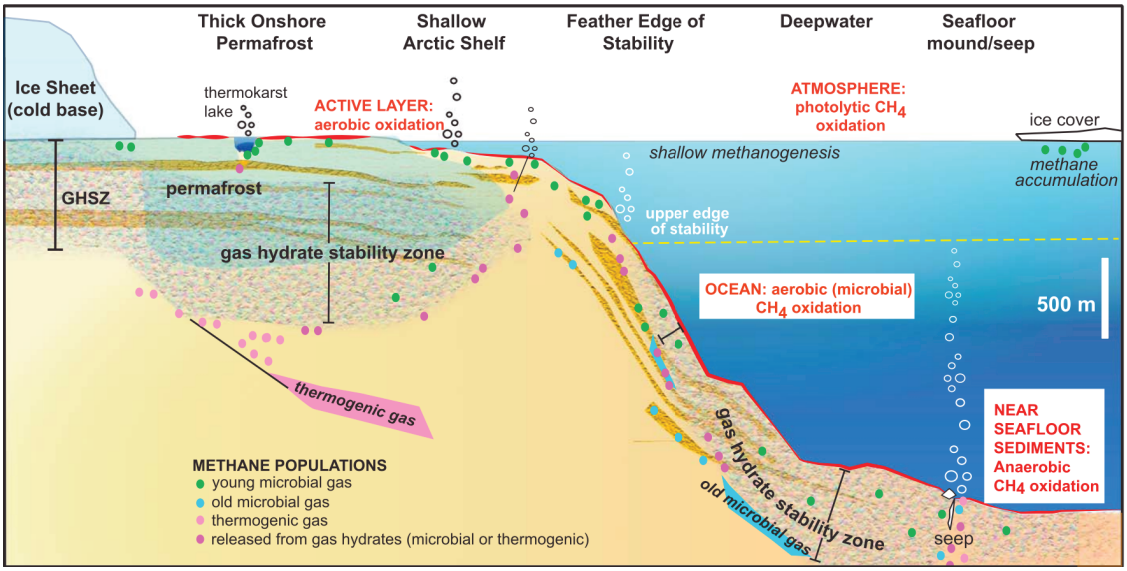

Figure 2.2: Methane hydrate distribution in different geological settings. This figure is reproduced from [16] under a CC BY-NC-ND 4.0 license.

estimate is the one made by Archer *et al.* [18] at 1600–2000 gigatons of carbon, or by Boswell & Collett [19] at 1500 gigatons of carbon.

Providing occurrence estimates for climate science and resource estimates for hydrate exploitation are two completely different games. Just like for other carbon resources, there is a resource pyramid for gas hydrates, of which only a small part is technically and economically viable [20]. It has been postulated that around 150 gigatons of carbon is technically recoverable from hydrates. For the sake of methane recovery, anomalies such as small but highly concentrated hydrates may be of great interest [19]. If one is concerned about methane release to the water column or atmosphere, on the other hand, large amounts of finely dispersed may be at risk of escaping if a reservoir is taken out of hydrate stability conditions. Such finely dispersed hydrates may be both technologically and economically unviable to recover, but nature doesn't need to collect it in a concentrated manner in order to release it.

2.2.2 Risk of methane emissions

It seems that slow, steady seepage of methane from hydrates does not increase the atmospheric methane levels nor contribute to global warming [16]. However, massive sudden blow-out events may let methane reach the atmosphere before it is absorbed in the water column. Craters from such blow-outs have been found in the northern Barents sea [7]. Another concern is that hydrate dissociation may trigger marine slope failure [21]. The ancient Storegga-slide [22] may act as an example of a worst-case scenario of such landslides. Accurately understanding the stability of formations containing methane hydrates would allow us to make better predictions about slope-stability and blow-outs.

There are several ongoing projects aiming at making gas hydrate recovery

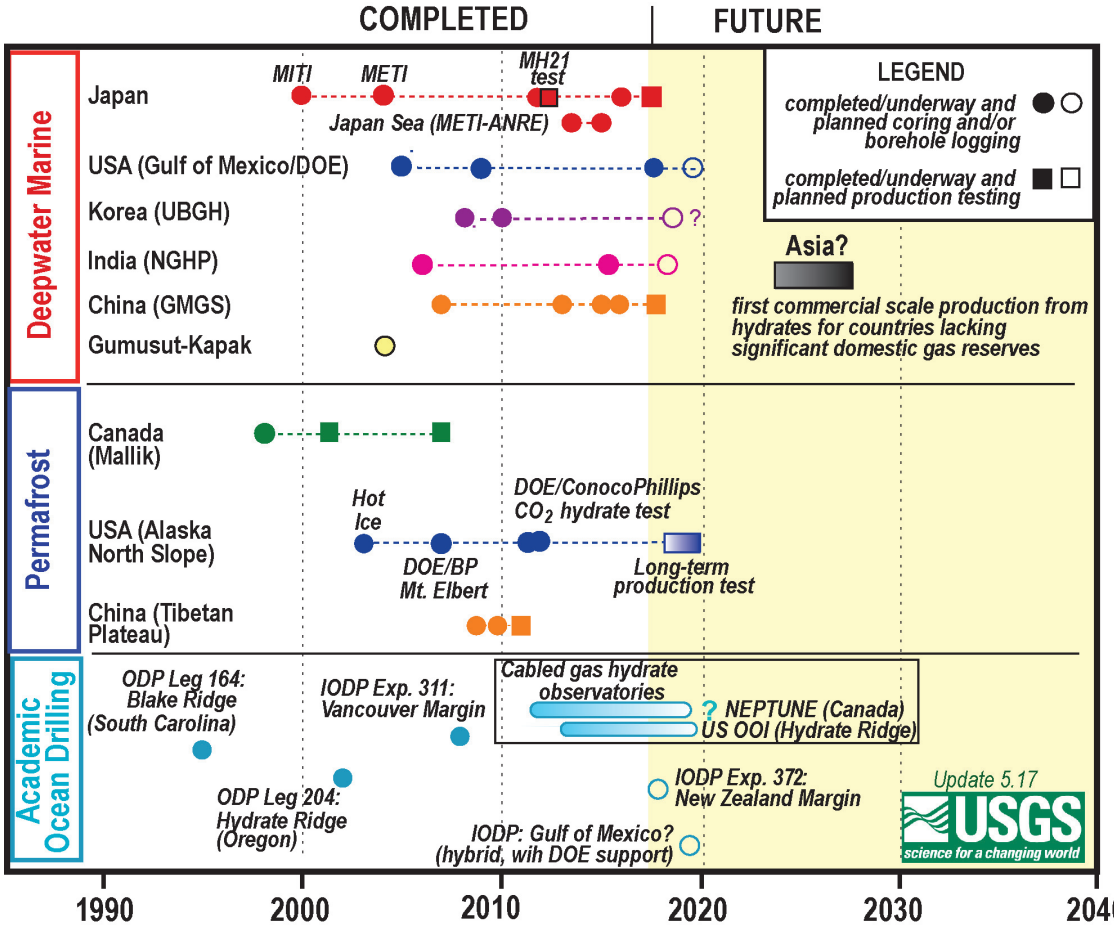

Figure 2.3: Current gas hydrate exploitation programs. Reprinted from Ruppel [23] Image credit: US Geological Survey, Public domain.

technologically and economically viable. Resource exploitation, as seen from the point of view of the sediment, is a form of methane emission, and accurately estimating the consequences of removing solid material gas hydrate is a prerequisite for doing this safely. There are several ongoing programs for exploiting hydrates as an energy resource. These programs are listed in (Figure 2.3 [23].

2.2.3 Hydrate-bearing sediments

Hydrates in nature occur in various types of surroundings: Sands, silts and clays, and they may be dispersed in several ways. The physical properties of hydrate-bearing sediments were reviewed by Waite *et al.* [24] in 2009. Regarding mechanical properties, a main take-home message is that the stiffness and mechanical strength of hydrate bearing sediments increase with an increasing hydrate saturation. There are other factors, but this simple fact tells us that hydrates are important to the sediments, and perhaps that the mechanical properties of the hydrates themselves influence those of the hydrate bearing sediment.

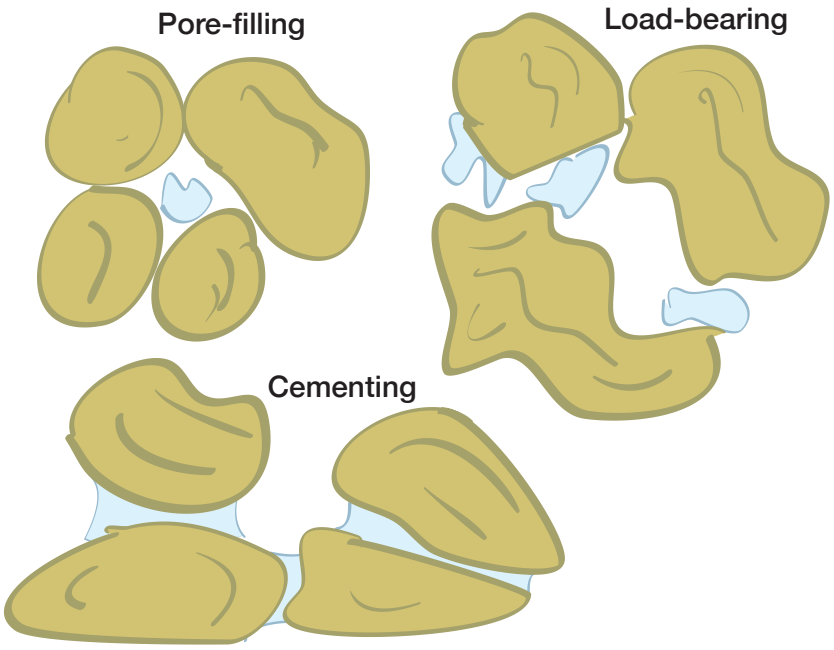

Figure 2.4: Illustration of hydrate pore habit. In the pore-filling case, the hydrate will not care about mechanical loading (except perhaps if the pore pressure changes). In the load bearing case the hydrate will be deformed. In the cemented case, the hydrate will interact with (in this illustration) the rotational frustration of the sedimentary grains, and thus influence for instance the friction between grains.

Pore habit

It is common to distinguish between pore-filling, load-bearing and cementing pore habits (Figure 2.4). Real hydrates in nature don't automatically submit to this categorization, but the pore habit is a valuable tool when thinking about hydrate bearing sediments. The pore habit is paramount both to what the hydrate will experience under strains on a hydrate bearing sediment, and for the fate of the sediment itself. Pore-filling hydrates are hydrates that partially fill voids in the sedimentary matrix. Such hydrates don't influence the mechanical properties of the sediment, at least not at low strains. Load bearing hydrates are part of the elastic response of the sediment. Cementing hydrates glue particles making up the sedimentary matrix together, and is thus part of the mechanical response both directly through the deformation of the hydrate, and indirectly by influencing the frictional properties of the host mineral, because hydrate must either be crushed or debonded from sedimentary grains in order for sediment grains to be displaced relative to each other. Both debonding and crushing have been inferred in experiment by failure envelope analysis [25].

2.3 Hydrate nucleation

Many of the past molecular studies of hydrates have focused on nucleation and growth kinetics. We may therefore rely on experiences from this field and try to apply relevant approaches to mechanical and failure properties.

Equilibrium properties of hydrates are generally well established. In a review paper from 2011 by Koh *et al.* of Colorado School of Mines [26], it was stated that the state of the art of hydrate thermodynamics were sufficiently developed for the community to focus on time-dependent phenomena. Also from a molecular modeling point of view, the equilibrium existence properties are well described, at least for simple systems. The three-phase coexistence of methane hydrate, water and methane in the TIP4P models was determined by Conde & Vega [27]. They showed that temperature–pressure coexistence line of TIP4P/Ice matched experimental values well, while TIP4P/2005 and TIP4P had offsets of around $-20\,\mathrm{K}$ and $-40\,\mathrm{K}$ respectively.

But hydrates don't simply appear in a system of methane in water solution as soon as it is taken into temperature–pressure conditions at which hydrates are stable. First, a hydrate has to nucleate. In flow loop-tests using natural gas, it has been shown that the gas-water mixture needs a subcooling of around $3.6\,\mathrm{K}$ with respect to the stability boundary in order to form hydrate [28]. In 2009, the first simulations of spontaneous nucleation of hydrates in atomic-scale simulations were reported [12], using the TI4P/Ice [29] potential to model water. This achievement allows for the study of formation kinetics, and thus associated hydrate inhibition strategies, such as how the pathways from gas–water mixtures to hydrates may be blocked. New strategies that allow hydrate to form, but not agglomerate to form a plug have also been developed, so called anti-agglomerants. The goal is to let hydrate form, but to form a slurry rather than a plug so that it can move safely in the pipeline. Several other studies have investigated the crystallization process, for instance Hall *et al.* [30] (group of Peter Kusalik) borrowed from protein-folding the funnel-shaped crystallization landscape for gas hydrate crystallization. Hall *et al.* used a different parametrization, TIP4P/2005 [31], of the same water model as the one used by Walsh *et al.* for the first nucleation-simulations.

The same year as the nucleation of hydrates in molecular dynamics simulations was reported, Molinero & Moore reported a new coarse-grained interatomic potential for water, the mW potential. The following year, they made a methane–water model to be used with mW [33]. This gave more than two orders of magnitude of speedup in terms of simulated mass×time of liquid or solid water per CPU-hour. This potential has also been used to simulate crystallization of both water [34] and methane hydrates [35]. Later on, the mW potential has also been used in non-brute-force simulations of hydrate nucleation [36]. This allows for sampling more of the *interesting* behavior and less of the waiting for something to happen.

Studying hydrates for application to flow assurance and to studying them for applications for geological hazards and resource exploitation is fundamentally different. The main concern in flow assurance is whether hydrates may nucleate,

agglomerate and finally form a hydrate plug in a pipeline. For resource exploitation and geological hazard prediction, the concern is the opposite: How may an already existing hydrate occurrence respond to some external driving force such as a spinning wellhead or anthropogenic temperature rise?

2.4 Experiments with relevance to gas hydrate decomposition and mechanics

Time-dependent phenomena of hydrates are not limited to the formation kinetics. Decomposition, plasticity and mechanical failure are coupled non-equilibrium processes. Thermodynamically, a hydrate chunk would prefer to be a single crystal embedded in an ideal isotropic pressure bath. But thankfully, the world is full of systems out of equilibrium. Hydrates exhibit prolonged non-equilibrium behavior due to, in lack of a more precise expression, complex kinetics. In this section, I lay out some experimental observations that motivate the study of molecular scale processes in hydrate failure.

Studies by Durham *et al.* [10, 37] showed that laboratory-grown methane hydrates are more than an order of magnitude more creep-resistant than their ice counterparts, and that hydrates are strain hardening at strains much higher than or ice. With both hydrates and ice being primarily hydrate-bonded substances, it must be fair to say that this is surprising.

Hydrate adhesive and tensile strengths have been tested in experiments by Jung & Santamarina [9]. They grew a hydrate meniscus between two mineral plates, and measured the pull-out strength. They found a pull-out strength for the hydrate itself of 0.20 MPa, but also that the failure may happen either by debonding of the hydrate from the mineral substrate or by a tensile fracture of hydrate, depending on the mineral surface type. The strength in this experiment was compared directly to ice specimens, and the pull-out strength of ice and hydrate were about the same when the failure was a fracture of the meniscus.

Experiments on hydrate-bearing sediments [38] have shown that hydrates themselves get crushed during the failure of hydrate-bearing sediments, warranting studying pure hydrates for understanding the strength of hydrate bearing sediments.

In a series of experiments on methane bubbles rising in a synthetic water column [8], Warzinski *et al.* created hydrate crusted bubbles by tuning the thermodynamic conditions and gas concentration. Figure 2.5 shows a picture of such a bubble along with an overview of the physical processes related to the rising bubble. The crusted bubble does not looks neither like a regular bubble nor like a balloon, because the hydrate crust is not elastic in the same way as a gas–liquid interface. Perhaps this bubble is more like a stiff, punctured balloon. There are several processes going on, for instance cracks driven by a plate tectonic like process. The exchange of gas between such bubbles and the water outside of it has been speculated to depend on the fracture properties of the crusting hydrate. Hydrate crusted bubbles have been observed in methane seeps on the seafloor [39]. The evolution of a hydrate crust on methane bubbles

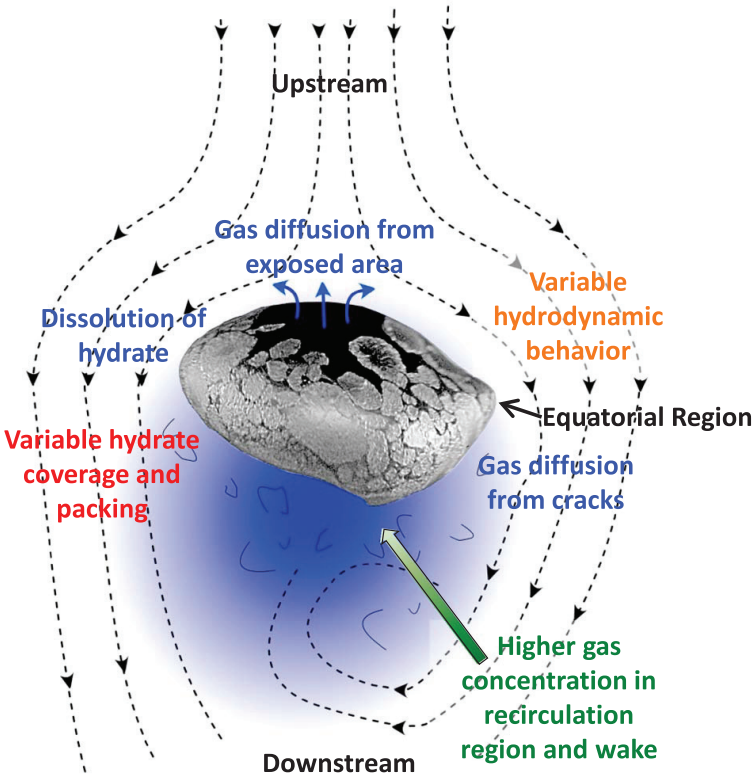

Figure 2.5: Bubble rising in an experimental water column. In reality, a downward water flow is keeping the bubble at a constant height to be observed and the height in the water column is determined by a pressure that is imposed on the riser. Reprinted from [8].

has also been studied by keeping a bubble at rest, but changing the confining pressure to simulate the rise of the bubble in the water column [40]. Cracks develop on the hydrate crust in these experiments as well, and these cracks have cleaner cleavage than those in the synthetic water column.

In a slightly different setup, at Colorado School of Mines, cohesion between hydrate particles suspended in oil using a cantilever that measures forces has been studied (eg. Aman *et al.* [41]). Often, the goal is to figure out what substance to add to the water surrounding the bubble in order for it not to attach cohesively to other hydrate crusted bubbles. In these experiments, the hydrate shell thickness, cohesion force between hydrate crusts and the force required to puncture a hydrate crusted bubble can be measured [42]. Similar experiments on tetrahydrofuran (THF) hydrates have shown logarithmic ageing effects [43]. This was interpreted as being due to a capillary bridge of liquid between two hydrophilic crystals rather than evolution of direct contact between two crystals.

Mechanical failure of hydrates may be induced by different means. External stress application is perhaps the most obvious and direct way to induce it, but there are other ways. For instance, it has been shown that cracks can appear on hydrate–ice interfaces [44] during dissociation of methane hydrate. It has been

speculated that these cracks are driven by differences in thermal expansion of hydrate and ice. Macroscopic cracks have recently been shown appear during thermally induced decomposition of CO_2 hydrates as well [45]. Here, it is speculated that a combination of thermal expansion and decomposition of hydrate itself drives the crack. The thermal expansion contrast between hydrate and ice creates stresses, and gas freed from decomposition builds pore pressure. Decomposition-driven cracks highlights the importance of including cracks in a predictive model for gas hydrate decomposition.

Strength behavior is usually influenced by the grain size distribution of a material, as shown for polycrystalline metals in the middle of last century [46, 47]. Chaouachi *et al.* [48] showed that laboratory grown methane hydrate coarsen extremely slowly, resulting in a grain size distribution with small grain sizes of around 1 µm even after several weeks of ripening. In the recent years, a new reactor that uses a thermal gradient in order to sample hydrate formation at several temperatures at the same time has been developed [49]. It seems like this reactor has the favorable side-effect of enabling growth of enormous–millimeter-sized–methane hydrate single crystals. If hydrate crystals grown in this reactor could be subjected to controlled mechanical loading, it would enable more robust comparison of mechanical properties in simulation and experiment.

Lastly, a comment on the usage of experimental analog hydrates: Since methane hydrates form under high pressure conditions, it is hard to keep them stable while performing measurements. Therefore, it is common to resort to experimental analogs: Hydrates of other guests than methane, such as THF, carbon dioxide, xenon and krypton. These have various advantages and disadvantages. For example, THF is a liquid and fully miscible in water at hydrate-forming conditions. Thus, phenomena like nano-bubbles are impossible, and mechanisms involving such bubbles will not be present. Another example: The density contrast between methane hydrates and pure water in X-ray computed tomography microscopy is weak. To look at hydrates while they fail mechanically, one can therefor make xenon hydrates instead, as these have a clearer density contrast due to the high molecular weight of xenon [50]. Xenon hydrate also forms under milder (closer to ambient) conditions than methane hydrates, and form the sI structure up tot 1.8 GPa [51]. It is worth keeping in mind that these analog hydrates are being used, and that they may have different properties. For example, phase-field simulations by Fu *et al.* [52] predict xenon hydrate layers forming on xenon–water interfaces to be thicker than their methane counterparts under the same forcing conditions.

In summary, there is experimental evidence for a range of physical processes involving the mechanical failure of methane hydrates, but where the nature of that mechanical failure is not understood. In particular, we believe that the studies of microscopic processes related to fracture and grain boundaries of hydrates are warranted.

2.5 Molecular modeling of gas hydrate mechanics

According to a review by Ripmeester [53] in 2000, hydrate research has matured from a correlation-based science up to the 1950's, to become a science where we can actually characterize and make predictions about hydrates using statistical physics and thermodynamics. In the last two decades, growth and nucleation kinetics (eg. Walsh *et al.* [12]) have been elucidated by molecular dynamics simulations. A natural continuation of this tradition is to use molecular dynamics simulations to learn about the processes of mechanical failure of hydrates.

It has also been suggested to use molecular dynamics simulations for mechanical and failure properties simply because it is difficult to produce pure hydrate samples, and simulations can avoid the difficulties associated with impurities [54].

With molecular dynamics studies of nucleation of hydrates becoming a mature field, it is somewhat surprising that studies of mechanical properties are so scarce. Perhaps it has to do with the requirements on system sizes in order to properly resolve a stress field driving mechanical failure.

Wu *et al.* [55] showed that polycrystalline hydrates under compression and tension exhibit grain size strengthening at low grain sizes and grain size weakening at larger (but still small) grain sizes in molecular dynamics simulations. The transition from the strengthening to the weakening regime happened around a critical grain size of 20 nm. Simulating a polycrystal of 16 grains, they needed simulations of millions of water molecules for the systems to be big enough to observe the critical grain size. Figure 2.6 shows some snapshots of damaged grain boundaries, stress–strain curves and quantitatively the grain-size effect. A strength that decreases with increasing grain size is often referred to as the Hall–Petch effect [46, 47]. For a grain size d, the strength in this grain size weakening regime follows a $\sigma \propto \frac{1}{\sqrt{d}}$ relationship. A grain size strengthening behavior in the nanocrystalline regime is often called the reverse Hall–Petch effect. If only *one* grain size strengthening and *one* grain size weakening regime occurs for small and large grains respectively, then there must necessarily be a grain size of maximum strength. This is referred to as the critical grain size d_c. The critical grain size is typically around 10–20 nm in polycrystalline metals [56, 57], but it is worth noting that much of the data underlying the determination of the critical Hall–Petch grain size are somewhat messy, and the aforecited papers mention a debate about whether the reverse Hall–Petch effect exists at all. In ceramics, the critical grain size has been measured as high as 130 nm [58] and as low as 18 nm [59]. Exploring grain size effects in more detail for more materials could provide clues both for hydrates themselves and for the mechanisms of the regular and reverse Hall–Petch effects.

More recently, Cao *et al.* studied high symmetry ice bicrystals and polycrystals of ice [60] and compared ice and hydrate bicrystals under tension [61]. They find that the tensile strength of hydrates is insensitive to the load directions.

The role of guest molecules have been investigated using several all-atom potentials [62]. It was predicted that there are subtle differences of the high strain mechanical and failure properties due to the polarity and size of guest

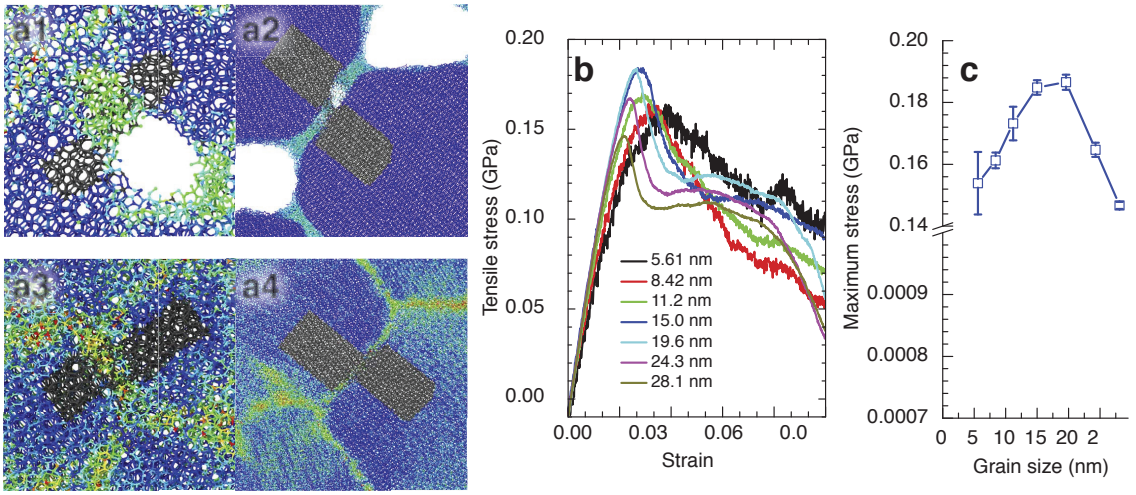

Figure 2.6: Figure composed from Wu *et al.* [55]. Grain boundary and junction details for tension of small-grained (a1) and large-grained (a2) and compression of small-grained (a3) and large-grained (a4) hydrate polycrystals. Stress–strain curve (b) for hydrate polycrystals of various sizes under tension. (c) Maximum stress plotted against the grain size, showing grain-size strengthening followed by grain-size weakening behavior.

molecules.

Jia *et al.* show differences in high-strain behavior of flawless hydrate and ice under tension [63]. They observed strain hardening of hydrates under extreme compression, in the giga-pascal range. Even though it would be surprising if what they observe is responsible for the strain-hardening of polycrystalline hydrates in the lab, which likely have grain size sensitive creep [48], the study by Jia *et al.* shows that the behavior of the ice and hydrate unit cells may diverge at high strains.

High strain behaviors have also been studied with density functional theory, showing that the structure I hydrate single crystal is isotropic [64]. This isotropic nature of hydrate was shown in a study comparing hydrate and ice, and where the ice unit cell was anisotropic (as expected). Such characterization has also been performed on hydrates in structure II [65].

The role of grain boundaries of hydrates has been brought up lately [48], in relation to mechanical properties. Grain boundaries of hydrates is not a mature field like the study of grain boundaries of metals [66]. In general, the possible topological complexity of a hydrate grain boundary surpasses that of a metal grain boundary. Molecular dynamics simulations indicate that grain boundary sliding is the main deformation mechanism in polycrystalline hydrates [55].

To summarize, the molecular modeling efforts have provided some insights, but there are still significant gaps in the knowledge. Most of the studies report on qualitative behaviors and mechanisms, but don't seek to fit these to laws that allow for upscaling. Molecular dynamics studies of polycrystals have only studied tension and compression, not shear. It seems that currently only a narrow selection of model systems have been simulated. There is for example

no account of the effect of gradually changing the orientation of neighboring grains with respect to each other. There is no molecular-scale evidence on the evolution of the shape of the parts of a hydrate polycrystal.

2.6 Outstanding questions

Many of the examples in this chapter highlight the importance of fracturing or fracture-like phenomena for understanding deformation of gas hydrates and the sediments bearing them in many natural systems.

(a) How does fracture initiation in hydrates depend on stress and temperature?

(b) Can emergent mechanical properties from high-throughput simulations be described mathematically for simple upscaling?

(c) What mechanisms are in play at the Hall–Petch breakdown under shear loading of hydrates?

(d) Why are ice and hydrates mechanically different?

(e) Why is the coarsening of hydrates so slow?

(f) What mechanisms may let grain boundaries move to evolve a hydrate polycrystal?

In Paper I, we bring insights to questions (a) and (b), in Paper II, we address (c) and to some degree (d). In Paper III we find that there are intrinsic differences in the shear coupling of ice and hydrates, proposing mechanisms for (d), (e) and a special case of (f).

2.7 A couple of related topics: Onset of dry friction and faceting of silicon carbide

The following two sections introduces extensions of the methods and approaches developed in this thesis to problems beyond gas hydrates, and methods that have been developed for multi-scale interface dynamics that also are relevant for mechanical deformation, fracture and friction in gas hydrates, although the main application has been to other physical systems. Since these topics are not part of the main story of this thesis, the relevant scientific background has been limited to not deviate from the main exposition.

2.7.1 Effective properties and upscaling to friction

In the dry friction community, we have seen major developments in descriptions of the relation between microscopic forces and macroscopic behavior. Several models have been developed in order to describe the effective behavior of a frictional interface, of which the rate and state friction model is probably the

most popular. Dry frictional systems exhibit stochastic stick-slip behavior, with characteristic timescales and lengthscales.

The onset of frictional slip and the failure of a crystal interface are closely related processes. At least in the case of hydrates, where the grain boundary stays flat during the onset of grain boundary sliding. The onset of frictional slip is mediated by a rupture front–a shear crack. Precursory cracks, which are cracks that don't span the entire interface that is to slip, can in fact be described by fracture mechanics [67].

One of the puzzles of the onset of frictional slip was the occurrence of slow fronts that were observed in an experiment by Rubinstein *et al.* [68] in 2004. These fronts occurred after the apparent arrest of a fast sub-Rayleigh shear crack. Rather than completely stopping, however, the crack continues growing slowly, at a speed more than an order of magnitude slower than the fast crack. Then, suddenly, the cracks starts moving fast again through the rest of the frictional interface. This sparked some interest among modelers, and several models were proposed to describe these phenomena (eg. [69, 70]). However, these approaches did not spontaneously produce fast and slow fronts and the transitions between them. There is a fundamental difference between a slow front propagating itself, with a speed determined by the frictional system itself, and a quasistatic slow front, which will necessarily depend on the external driving force.

Paper IV [71] deals with the emergent behavior of a model where an elastic medium is coupled to an interface consisting of an array of elastic micro-junctions with time-dependent healing properties. The healing process can for instance be cooling after a slip-heat induced glass transition [72]. With the model of Paper IV, we propose a possible mechanism for the dynamic slow fronts observed in experiment.

The approach in Paper IV may be used for building a multi-scale model for the fracture and friction of gas hydrates.

2.7.2 Normal grain growth barrier in silicon carbide

Barriers to normal growth are present in other systems than icy polycrystals. An example is faceting and normal grain growth on a nanoparticle. Ideally, a nanoparticle wants to assume its equilibrium shape [73], but the kinetics won't allow it to. The magnitude of this barrier is assumed to grow quickly with the face area of the nanoparticle face to grow new layers, to an extent where a face size of only a few nanometers can be prohibitive of normal grain growth [74]. Such shape-changes have been studied before with monte-carlo techniques [75], but not in a brute-force molecular dynamics way. When working with hydrates, which seems to be a substance with strong kinetic barriers both in terms of nucleation and normal grain growth of a polycrystal, lessons learned from studying other substances with barriers that are hard to surpass in molecular dynamics simulations may be instructive. Paper V deals with the evolution of the equilibrium shape and energy barriers no normal crystal growth related to reaching that equilibrium shape.

Chapter 3

Molecular dynamics simulations and analysis

This chapter briefly describes molecular dynamics simulations, some of the tools that I have made in order to perform and analyze such simulations, and some thoughts on replicabiblity and data management.

The world on the nano-scale consists of atoms and molecules. The basic assumption of molecular dynamics simulations, is that atoms may move as point particles according to Newton's second law. The full state of a system can thus be described by only the positions and momenta of the particles. Forces between particles are determined only based on their relative positions.

Molecular dynamics have essentially two ingredients: A function $U(\mathbf{r})$ that determines the energy of a system as a function of particle positions, and rules for how to explore different places $(\mathbf{r}, \mathbf{v})$ in phase space. The simplest rule is to let particles move according to Newton's second law, which entails micro-canonical dynamics. There are many other ways to obtain different dynamics to investigate other parts of phase spaces. A common way is dynamics coupled to a pressure- and heat bath in order to mimic an NPT enseble. NPT dynamics have Newtonian mechanics in addition to Parinello–Rahman stress tensor coupling [76] and Nosé–Hooover temperature coupling [77, 78]. Such temperature- and stress coupling is implemented in LAMMPS [79], and the formulation actually implemented in LAMMPS is by Tuckerman *et al.* [80]. When a system is out of equilibrium, I prefer to call it thermo-baro coupled molecular dynamics rather than NVT or NPT, because out of equilibrium we are not truly sampling an ensemble.

As all simulations, molecular dynamics simulations are explorations of the consequences of a model. We observe the emergent behavior, and hope to learn something about the world.

3.1 Interatomic potentials and choice of potential.

The contents of the function U is the whole model for how the substance we are modeling shall behave. Ideally, one would want to be able to describe all interactions by the most accurate theory there is: quantum field theory. But this is not computationally viable. We are simply unable to use the rules of quantum field theory to study the emergent behavior of complex large systems. The whole is different from the sum of the parts [81]. A next level, ab-initio methods based on the Schrödinger equation, allows for simulations of systems up to a few nanometers for tens of picoseconds. To be able to model grain boundaries and fractures in hydrates we need simulation sizes on the orders of tens of nanometers.

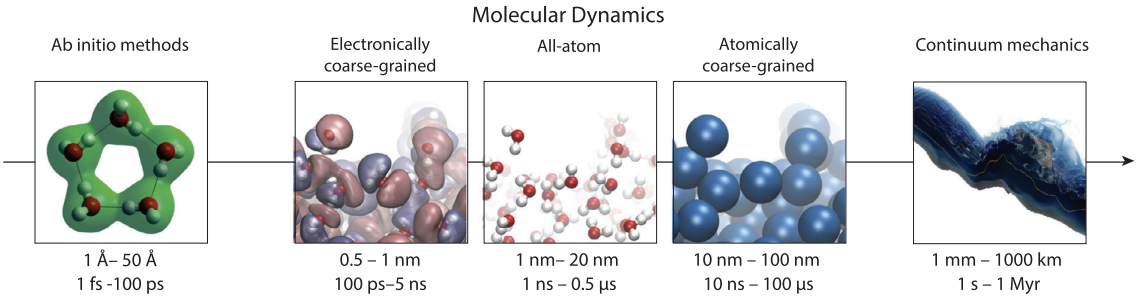

Figure 3.1: Reproduced from [82] with permission from Elsevier.

Figure 3.1 shows an overview of simulation techniques sorted by timescales and length-scales. As computers become faster and algorithms more efficient, these scales will increase for all of the methods, but Figure 3.1 shows what the state was around 2016.

Traditionally, the TIP4P potential has been a popular choice for modeling water when the properties of the water itself is of importance. It was for example a variant of the TIP4P potential, TIP4P/Ice, that was used to perform the first simulations of spontaneous nucleation of methane hydrates in molecular dynamics simulations [12]. TIP4P is an all-atom potential, though with rigid covalent bonds between oxygen and hydrogen, but still it requires that the interactions are calculated for all atoms, and that the time discretization is able to resolve the rotational motion of the water molecule.

3.1.1 Monatomic water potential

The simulations in Paper I, Paper II and Paper III rely on a specific intermolecular potential, the mW potential. I will therefore assess the applicability of molecular dynamics simulations with this potential for mechanical and failure properties simulations.

The development of a monatomic water potential [32] increased the spatio-temporal range of molecular dynamics simulations of water by two orders of magnitude. This enables modeling hydrate and water ice polycrystals of sizes where both grain size strengthening and grain size weakening is present. Since we are modeling such phenomena, we need to perform atomistically coarse-grained simulations and the only available potential is the monatomic water potential by Molinero & Moore [32], with the extension for treating methane and methane–water interactions [33]. Some very recent developments of new coarse grained water potentials are commented in Chapter 5.

Since simulations for mechanical and failure properties of hydrates are scarce, there is naturally not too much verification data available in the literature. In any case, we may start with the clues we can get from the original publications of the mW water potential [32] and the methane–water extension [33].

The functional form of the mW potential identical to the Stillinger–Weber

potential for silicon [83]:

$$E = \sum_i \sum_{j>i} \phi_2(r_{ij}) + \sum_i \sum_{j\neq i} \sum_{k>j} \phi_3(r_{ij}, r_{ik}, \theta_{ijk}) \tag{3.1}$$

$$\phi_2(r_{ij}) = E\epsilon \left[B \left(\frac{\sigma}{r_{ij}} \right)^4 - 1 \right] \exp\left(\frac{\sigma}{r_{ij} - a\sigma} \right) \tag{3.2}$$

$$\phi_3(r_{ij}) = \lambda\epsilon \left[\cos\theta_{ijk} - \cos\theta_0 \right]^2 \exp\left(\frac{\gamma\sigma}{r_{ij} - a\sigma} \right) \exp\left(\frac{\gamma\sigma}{r_{ik} - a\sigma} \right), \tag{3.3}$$

where the parameters A, B, γ, a and θ_0 are equivalent to those of the original Stillinger–Weber potential, whereas σ, ϵ and λ are changed in order to make it behave like water rather than silicon. These parameters were fitted in order for the potential to reproduce the enthalpy of vaporization, ΔH_{vap}, the density of liquid water at 298 K, $\rho_{298\,\text{K}}$ and the melting point of hexagonal ice, $T_{\text{m, Ih}}$ For the methane–water and methane–methane interactions, $\lambda = 0$ so that only the two-body term ϕ_2 applies, and the parameters ϵ and σ are different for each pair of particle species: water–water, water–methane and methane–methane.

The parameters σ and ϵ of the methane–methane and methane–water model of Jacobson & Molinero [33] were chosen close to the border between sI and sII preferential stability, based on experimental data. This property of the potential should be of importance to grain boundary structures of bi- and polycrystalline hydrates under shear in Paper II and Paper III, where destruction and formation of hydrate competes and crystallographic mismatch along grain boundaries leads to polymorphism. The methane of this model is reported in the original publication [33] to be a bit too compressible compared to experiments, thus methane freed from hydrate in simulations will possibly not create as high a pore pressure as it would in reality. On a general note, I would assume that the same applies to the high-strain regime of hydrates, since the Stillinger–Weber form of the water potential is soft for small particle separations (compared to Lennard–Jones).

When performing simulations of mechanical and failure properties, the mechanical properties of the intermolecular potential is crucial. If hydrates are isotropic (which they are), we can use the Young's modulus, E, and Poisson's ratio, ν to verify the potential against experimental results. E and ν are straightforward to calculate by molecular dynamics simulations, and I did therefore check them before I started using the mW potential for fracture simulations. After all, this potential was never fitted to the elastic properties of methane hydrates. Elastic constants taken from simulations of sI methane hydrate systems containing $3 \times 3 \times 3$ unit cells are shown in Figure 3.2. For temperatures ranging from 160 K to 300 K. Young's modulus varies from 8.6 to 7.4 GPa, and Poisson's ratio from 0.30 to 0.32.[1] These estimates were made using the averages

[1]The simulations underlying these data were NVT simulations with deformations imposed along all coordinate directions, one at a time. The sample was first relaxed at a confining pressure of 10 MPa for 1 ns, and then run for 1 ns over which the average box dimensions were sampled. The system was then subjected to deformation with respect to those average box

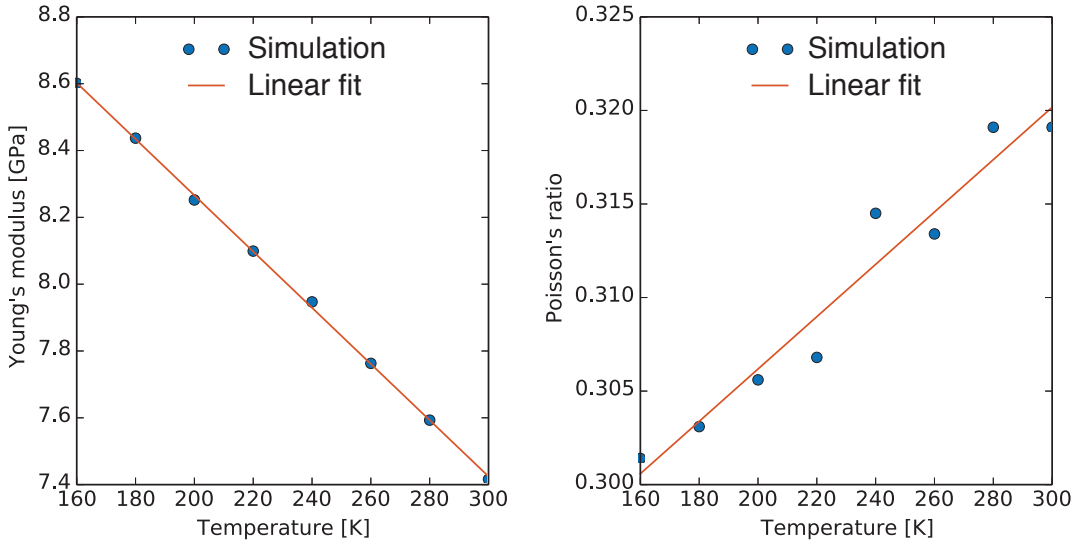

Figure 3.2: Young's modulus (left) and Poisson's ratio of fully occupied sI methane hydrate modeled with the mW model as a function of system temperature. The estimates are made using the stress response of strains up to 1%.

of the relevant components of the stress tensor ($C_{ii}, C_{i\neq j}$) after identifying from the stiffness matrix that the material was isotropic ($\pm 1\%$) both at (0 K, 0 MPa) and at (260 K, 10 MPa). Experimentally, it has been shown previously that sI methane hydrates are isotropic, and that they have a Young's modulus of 7.4 GPa and Poisson's ratio of 0.34 at 20 MPa and 296 K [84].[2] We therefore conclude that the mW potential reproduces well the low-strain mechanical properties of methane hydrates. For the high-strain regime, I have not been able to find experimental values for comparison.

We chose to use the mW model to simulate hexagonal ice in Paper III in order to compare the properties of mW hydrate to mW hexagonal ice. It is reasonable to believe that some of the differences between these substances in nature are observable also in these mW models, although it is not certain. The elastic constants of mW hexagonal ice has recently been assessed and compared to other water models [85]. The main features is that the mW model quantitatively reproduces the elastic constants more precisely than common all-atom models, mW fails to reproduce the elastic anisotropy.

There is also some evidence that the mW model deviates from the behavior of TIP4P/Ice at high pressures. In particular, under extreme compression, mW hexagonal ice just keeps shrinking, whereas TIP4P undergoes a transition to a

dimensions, and then equilibrated over 1 ns. Finally, the stress tensor was sampled over 2 ns, and this stress tensor entered the subsequent calculation of the Young's modulus and Poisson's ratio.

[2]Reading the data points of Fig. 5 in [84] visually, I find $C_{11} = 11.6$ GPa, $C_{12} = 6.1$ GPa and $C_{44} = 3.4$ GPa. We obtain Poisson's ratio by assuming an isotropic medium and therefore using $\nu = (1 + \frac{C_{11}}{C_{12}})^{-1}$, and Young's modulus by using $E = \frac{C_{11}+C_{12}}{(1+\nu)(1-2\nu)}$

high-density liquid around 0.7 GPa [86]. This is attributed to the mW model favoring tetrahedral order, which is natural since this is explicitly forced. This means that there are some relevant physics that are missing from ice mechanics. But that does not prohibit differences between ice and hydrates to be discovered, it just narrows down the range of possible mechanisms that can be revealed with this methodology.

Having the aforementioned limitations in mind, we use the mW potential for hydrates, and hexagonal ice for comparison. We also keep in mind that simulation results are just computations of the consequences of a model under certain conditions. If the consequences are not reproducible by experiments, it means that the model is not suited to describe the phenomenon at hand. But if computing the consequences of a model using a simulation reveals something interesting, it can help suggest what experimentalists should look for.

For completeness: After the simulations of Paper III were performed and analysed, we found that some new bond-order coarse-grained water models had been recently published [87]. At least one of these is specified as particularly suited for friction simulations and ice mechanics. A natural next step would therefore be to validate whether these bond-order potentials reproduce what we see in grain boundary simulations of hexagonal ice using the mW potential.

3.2 Building polycrystals

In Paper II we needed to create polycrystals by Voronoi tesselation. I therefore made a python script for that, using `voro++`. This unfortunately makes the script depend on `pyvoro`, which complicates usage. I also use `glumpy` to let the user (in this case only me) visually inspect the created polycrystal. Glumpy is hard to install. Therefore, it is not straightforward to use this polycrystal builder. It is almost or completely impossible with Python 3, but somewhat easier to get it to work with Python 2. However, this polycrystal builder must not be expected to be simple to install. Anyway, it is on Github: https://github.com/henriasv/voronoi-crystals. Regardless of being cumbersome to install, the implementation provides documentation of how the polycrystals were made.

3.3 Analyzing particle trajectories

The state $(\mathbf{r}, \mathbf{v})$ of a molecular dynamics simulation can be represented by the velocity and position of all of its particles. The time-propagation of the system also involves computing the force between particles, so we may consider also forces as immediately available. If a simulation is run a thermo-couple or a thermo-baro-couple, then the simulator also needs to compute the temperature and the pressure in order to perturb the simulation towards the designated pressure and/or temperature. This is the basic information that is available. In order to learn more, we either need to use build-in analysis capabilities of the simulator, make our own extensions to the simulator, or do post-simulation analysis on data that we store from the simulation.

For the analyses performed in the papers in this thesis, I have mainly used the following:

Simulation cell stress tensor calculated by LAMMPS. In all of the gas hydrate papers, stress–strain curves have been central, and thus the built-in stress calculations have been very useful. To efficiently work with these data, which LAMMPS provides through log files, I made a python module for reading such log files.

Per-atom stress tensor calculated by LAMMPS. In Paper I I use this for visualization and in Paper II I use this to determine the local fracture mode at the grain boundaries of a polycrystal.

Chill+ for structure visualization. In Paper II I use Chill+ to show visually the differences in how hydrate polycrystals fail, based on their grain size. In Paper III I use Chill+ to show how the grain boundary structure is different for ice and hydrates. I could not find a reasonably user-friendly implementation of Chill+ anywhere on the internet, so I chose to implement it for The Open Visualization Tool (OVITO) [88].

To simplify high throughput analyses, I made a tool, `regex-file-collector`, that uses regular expressions to find files and structures them in a parameter-hierarchy based on their path name.

3.3.1 Chill+ implementation for OVITO

The Chill+ algorithm [89] from 2015 is an algorithm that detects several solid phases of water: Hydrate, hexagonal ice, cubic ice, interfacial hydrate and interfacial ice. During the work with this thesis I made an implementation of this algorithm for my personal use. At some point I realized that this implementation would get a longer life if I accommodated it to the popular molecular visualization tool OVITO [88]. This contribution has been included in the current development version of Ovito on Gitlab[3] per merge request 21[4].

3.4 Micro-automation

In order to work efficiently with atomistic simulations, or other kinds of simulations for that matter, I have made a couple of small python packages. These can be installed using `pip`.

3.4.1 `lammps-logfile`

When I started using Lammps for molecular simulations, I used the log reader (`log.py`) from the *pizza* package for Lammps. This turned out to have two major disadvantages: First, it was slow, because it hadn't been sufficiently optimized. This made the analyses of thermodynamic data from multiple simulations cumbersome, because each analysis took several minutes, when it

[3] gitlab.com/stuko/ovito

[4] gitlab.com/stuko/ovito/merge_requests/21

could have taken only seconds. Second, it is fundamentally wrong, from a software engineering point of view, to put some file (`log.py`) in the `PYTHONPATH` on the system if the contents of that file is being used in production and not only for developement. This python package extracts the per-timestep thermodynamic output from LAMMPS log files, and makes them available as vectors by a `get`-function. Install with

```
pip3 install git+https://github.com/henriasv/lammps-logfile
```

A basic usage example if you have a log-file in `/home/log.lammps` with columns of (amongst others) `Time` and `Pxz` is

```
from lammps_logfile import File
log = File("/home/log.lammps")

t = log.get("Time")
pxz = log.get("Pxz")

import matplotlib as plt
plt.plot(t, pxz)
plt.show()
```

In addition to reading LAMMPS log files, `lammps-logfile` also exports to Exdir [90], a directory-based hierarchical storage format. If a set of simulations is finished, then their log file contents can be exported to Exdir for faster access at a later point. Reading from Exdir is faster because (i) only the requested data (eg. temperature) needs to be read and (ii) the data is stored in binary files, and thus need not be parsed. This is useful when log files are sufficiently large for it to take human-noticeable time to read them.

3.4.2 `regex-file-collector`

When running a large number of simulations, being able to access them in a hierarchical manner may be convenient, for instance when doing parameter sweeps. This is the purpose of `regex-file-collector`. It takes a path and a regex pattern, and finds any file in the directory structure beyond path that matches pattern. The files that are found are then identified by capturing groups of the pattern they matched. Double matches are not allowed.

A simple example of the usage of this package, if a directory called `/boundary/interface_simulations` contains thermodynamic output in the form of LAMMPS log files, and you want to plot the tensile stress in the z direction of the simulation box for all of those simulations, is:

```
from regex_file_collector import Collector, floating_number_pattern
from lammps_logfile import File
import matplotlib.pyplot as plt

path = "/boundary/interface_combinations"
pattern = floating_number_pattern("T") + "_" + floating_number_pattern("erate")
      + "_" + floating_number_pattern("Nrot") + "/log.lammps"

collection = Collector(path, pattern)
```

```
for T, value_T in collection.get_tree().items():
    for erate, value_erate in value_T.items():
        for Nrot, filename in value_erate.items():
            log = File(filename)
            t = log.get("Time")
            pzz = log.get("Pzz")
            plt.plot(t, pzz)
plt.xlabel("Time")
plt.ylabel("Tensile stress")
plt.show()
```

In this particular example I use a helper function that generates regular expression patterns for floating point numbers. In a general usage case, one simply creates a pattern that contains the "catching groups" of the parameters that vary.

3.5 Replicability and data management

Replicability is important in computational sciences. It is also currently fashionable. With the introduction of FAIR principles [91] for data, pushing the availability of the data underlying scientific studies, which improved the replicability of studies. This comes in addition to an increased push for open access to scientific papers [92]. Some communities are leading in replicability, like the high-energy physics community (CERN). An important message from the high-energy physics community is that "Open is not enough" [93]. It is not enough to provide the data, you also need to take extra action to make replication possible, beyond just writing down exactly what you did. Of course, such large collaborations have access to support facilities that most researchers can only dream of in terms of help with data openness and analysis documentation. But they lay out reasonable principles that we can all learn from, and in particular principles that the molecular simulations community can use in order to create replicable simulation results.

FAIR principles, PowerPoint presentations containing clouds[5] of data, the wheel of the research data cycle and best practices are buzzing out there. But to go from these ideals to real-world implementations on a day-to-day basis under time and resource restrictions is not straightforward. Therefore, in the next few paragraphs, I share some thoughts and considerations I have made on this topic during the work on this thesis. This may serve as a realistic example of how things can be done in practice in a small group.

Molecular simulations produce a lot of data, and there are mainly two classes of data. The first is simulation cell-wide data. Typically scalars and vectors pertaining to the thermodynamic and geometrical state of the system as a whole. The second is particle-level data. Positions and velocities of all particles, forces, virial stresses, anything that may be calculated for a given particle. The particle-level data are usually orders of magnitude bigger than the simulation-cell level data. It is uncommon to store all particle-level data from each simulation step,

[5] One must always remember that there is no cloud, only other peoples computers. The cloud gives a false sense of data safety.

so this is the first point at which data is being thrown overboard. We decide on a proportion of data to actually store from a simulation for subsequent analysis. Sometimes this proportion is determined by a gut feeling, and sometimes we calculate how much we are able to store.

During the work with my thesis I had access to some tens of terabytes of local hard drive space. This is approximately as much as one can efficiently work with when performing post-processing of results on a desktop computer. Based on the amount of disk space available, we choose a sampling rate of the state of the system in our simulations. Failed simulations and pilot simulations and so on are often deleted. We make a backup of as much as possible of the data from simulations whose results are reported in publications.

Around publication time, I upload enough input data to zenodo.org for the simulations to be reproduced, and enough thermodynamic data from the simulations to redo some of the analyses. In practice, this means *all* LAMMPS input scripts and *all* LAMMPS log files. The input files facilitate straightforward replication, and the log files contain the version date of LAMMPS to ensure that the simulation can be run agin with the exact same version of LAMMPS. This dataset is referenced as supplementary data in the publication itself. Zenodo is a storage service by CERN, and it is backed by the EU Commission. This ensures that the data will be archived for as long as CERN is operating. Zenodo currently accepts datasets up to 50 gigabytes, so some datasets are too big for upload. In particular, it is not feasible to leave a lot of particle trajectory data there. Trajectory data can be provided upon reasonable request as long as we have them. Since reproducing trajectory data is straightforward and not too expensive, we don't have a long-term storage plan for trajectory data, save for selected frames from simulations. Table 3.1 summarizes the different strategies we choose for different types of data.

The absolutely most valuable data, is the final processed data that makes it into the figures and equations of a scientific paper. This is the data in its most condensed form (at time of publication, anyway). We consider this data to be so important that we pay a publisher to keep and curate it for the foreseeable future.

A part of replicability is also to make tools that facilitate replication. In that sense, `lammps-log-plotter` and the `regex-file-collector` are tools that makes it easier to set up a structured analysis pipeline. An ideal situation, which I did not get to during this work, is to set up an automated pipeline containing all the software at the right versions. An automated pipeline can for instance be achieved using Docker images to run the whole analysis on a virtual machine on some cloud service. That way, one ensures that none of the analysis is hidden in some script or environment variable or random number generator hardware unit or *something* that is specific to the computer or setup that the researcher is using. Also, it ensures that mistakes aren't introduced by day-to-day mistakes like running two scripts in the wrong order.

Data type	**Amount**	**Data lifetime**
Full trajectories	Petabytes	Thrown during simulation
Samples from trajectories	10's of terabytes	Till the backup crashes (yes, really)
Critical atomic positions	10's of gigabytes	Till CERN closes
LAMMPS log data	Gigabytes	Till CERN closes
Scientific papers	Megabytes	max{Publisher, UiO}

Table 3.1: Caption

Chapter 4

Summary of papers

The publications appear in full later in the text. In this chapter, I summarize our findings and comment on how the different papers relate to each other. Since papers I–III are the main story, they are treated more thoroughly than papers IV and V.

4.1 Paper I

Paper I is [Henrik Andersen Sveinsson and Anders Malthe-sørenssen. Molecular-scale thermally activated fractures in methane hydrates: a molecular dynamics study. *Physical Chemistry Chemical Physics* vol. 21, 13539–13544 (2019)]. I presented an early version of this work at the International Conference on Gas Hydrates 2017, Denver CO.

4.1.1 Summary

In Paper I we study the initiation of tensile cracks in monocrystalline hydrates with a penny-shaped crack. This is the first treatment of the molecular structure of methane hydrates using fracture mechanics. We perform a series of simulations over a range of temperature and strains allowing a systematic study of the fracture initiation waiting time of methane hydrate single crystals. We show that the hydrate cracks in a brittle manner, cage by cage, and that the waiting time before the crack starts propagating fast is consistent with a thermal activation model for fracture [95]. In this model, the system needs to pass a local elastic barrier in order for the crack to grow slowly.

Paper I is different from similar studies on hydrates in that it (i) studies fracture initiation from an intentionally pre-existing flaw and that it (ii) fits the results to a model so that the results in principle can be scaled up.

4.1.2 Comparison to other work

Paper I is inspired by a suggestion from Ning *et al.* [54]. We only have methane in the cavity, whereas Ning *et al.* also suggested to put liquid water in the cavity. Wu *et al.* [55] measured the tensile strength of flawless methane hydrates and of polycrystalline hydrates. Cao *et al.* [61] studied tension of hydrate–hydrate bicrystals, but focus on the difference between different high symmetry bicrystals, and does not investigate temperature and strain sensitivity. The yield strength of hydrates has been predicted using density functional theory [64], but this is fundamentally different from what we do, because they look at flawless crystals. Thus, one finds the high strain behavior, but without describe how the strains gets focused to certain locations and the anisotropic stress state resulting from

stress concentration at sharp cracks. The closest experimental study I have found is one by Jung & Santamarina [9]. Jung & Santamarina study the tensile failure of a gas hydrate meniscus between two mineral plates, using both methane and other gases as the guest gas. Some of their methane hydrate samples fail by a crack spanning a plane of the meniscus. Being a methane hydrate formed in the lad, this hydrate meniscus must have been a polycrystal, unlike the single crystal of our study. Furthermore, finite element analysis indicated that the fracture was initiated by dissociation in the core of their hydrate meniscus rater than a Griffith-type crack. However, one could also speculatively think of this initial dissociation as the seed of a crack that can go unstable in a thermally activated manner. Shameless extrapolation from Paper I would indicate that an initial flaw of 10 microns should go critical in a few microseconds. The microsecond timescale could be relevant to compare to crack blunting effects such as melting or healing effects such as freezing. Interestingly, 10 microns is approximately the highest crystal size recorded in newly formed methane hydrate. However, one should be very careful not make strong conclusions based on such extrapolations.

Since it is hard to make experimental measurements of the fracture strength of pure hydrates, molecular dynamics simulations may provide the best estimate of the fracture toughness.

4.2 Paper II

Paper II is [Henrik Andersen Sveinsson, Fulong Ning, Pinqiang Cao, Bin Fang, Anders Malthe-Sørenssen. Grain-size dependent deformation and failure behavior of polycrystalline methane hydrates (Ready for submission)]. I presented an early version of this work at the Gordon Research Seminar on Natural Gas Hydrate Systems in 2018 and as a poster on the related Gordon Conference, Galveston TX.

4.2.1 Summary

In Paper II, we seek to model a more complex system than in Paper I. We apply simple shear to hydrate polycrystals over a range of grain sizes and temperatures, to model more of what hydrates actually look like in nature.

First, we show that, under simple shear loading, hydrate polycrystals exhibit grain boundary strengthening up to a critical grain size of around 20 nm and grain boundary weakening at higher grain size. We indicate that the maximum strength of the polycrystal depends on the grain size d as $d^{1/3}$ up to the critical grain size.

Second, we show that qualitatively, the crossover from grain size strengthening to grain size weakening behavior is accompanied by a change in the damage pattern on he grains of the polycrystal. For small grain sizes, there is appreciable wear and cracking of the corners o the crystals, whereas for larger grains, the failure happens by the opening of grain boundaries, and no damage to the interior of the grains.

Second, we show that the behavior is accompanied by a change in the local failure mode from shear to tensile, by analyzing the normal and shear tractions over the grain boundaries. The relative magnitude of the tensile traction increases with respect to the shear traction as the grain size increases. This relation seems to saturate around the critical grain size, but at different levels depending on the temperature. Therefore, this study also indicates that the grain size distribution influences the temperature-sensitivity of hydrate strength.

4.2.2 Comparison to other work

Paper II is yet another study showing Hall–Petch-like behavior and the breakdown of the Hall–Petch effect at nanoscale. This type of behavior is well-established for metals, but not that well established for other substances. For instance for ceramics, the critical grain size has been reported as high as 130 nm [58] and as low as 18 nm [59]. A similar set of simulations as in Paper II were performed by Wu *et al.* [55], showing a critical grain size around 20 nm, but under tensile and compressional loading conditions. Cao *et al.* has shown grain size strengthening of ice polycrystals modeled by the mW potential, but the grain size range of their simulations (up to 16 nm grain size) was not sufficient to establish the critical grain size. The perhaps most novel result of Paper II is the clearly visible and simultaneously quantitatively measurable transition from shear to tensile failure when approaching the critical grain size.

The state of the art of hydrate polycrystals is nowhere as sophisticated as for metals [66], but this is only to expect with such a topologically complex substance.

4.3 Paper III

Paper III is [Henrik Andersen Sveinsson, Kjetil Thøgersen, Anders Malthe-Sørenssen. Intrinsic differences in stress accommodation mechanisms of ice and gas hydrate bicrystals under shear loading (In preparation)].

4.3.1 Summary

In Paper III we take a step back from Paper II, to examine thoroughly what happens on grain boundaries. We do so because stress build-up from grain boundary sliding seemed to be an important mechanism for failure of polycrystalline methane hydrates in Paper II, thus requiring a deeper understanding of such sliding processes. Paper III shows differences in shear deformation mechanisms between ice and hydrate bicrystals. These differences may contribute to their divergent failure behavior. The main purpose of this paper is to contrast the behaviors of hydrate and ice interfaces under shear loading. We find that symmetric tilt grain boundaries tilted around the basal and a prismatic plane of ice and the basal plane of hydrates behave differently.

First, we investigate ice–ice symmetric tilt boundaries. The tilt axis is parallel to the ice $\overrightarrow{c}$-axis, which is the normal of the basal plane. We observe that the

boundary accommodation structure is composed of 5-membered and 7-membered rings, and that for the low and moderate tilt angles, the crystal structures mainly fit together, with the non-hexagonal rings forming isolated accommodation wires parallel to $\overrightarrow{c}$. We show that in this regime, the grain boundary migration speed can be related to the applied shear stress and the dislocation density through a simple formula. The migration velocity is highly dependent on both the dislocation density and the shear stress. We also show that for symmetric tilt grain boundaries around an axis in the basal plane, ice still exhibits grain boundary migration, but not to the same extent as for tilts around the $\overrightarrow{c}$ axis. The behavior for this near-basal-gliding-plane tilt boundary is stick-slip-like, and the average value of the stress–strain curve is between 50 and 100 MPa, with a significant systematic angular dependence and some dependence on the shear rate.

Second, we report simulations of methane hydrates under similar conditions, showing a very different behavior from the $\overrightarrow{c}$-axis tilted ice, and quite different from the basal plane tilted ice. Most of the hydrate–hydrate interface may be regarded as boundary structure, rather than the accommodation structure being localized as wires. We show that under these conditions, the grain boundary of the hydrate does not migrate, except for the highly specific case of the 53.13° angle, which does migrate. Also, there is no structural transformations of the hydrate, except for the formation of sI and sH-like motifs right on the grain boundary. The lack of migration and structural transformation results in grain boundary sliding being the only strain accommodation mechanism, and consequently completely different stress–strain behavior. The strain-rate dependence of the (now frictional) strength vanishes, and the shear stress values typically vary between 100 and 150 MPa, without any clear tilt angle dependence.

Even though the grain boundary migration we observe in the ice simulation are not directly flow of ice, we provide evidence that there is a range of possible flow mechanisms of ice that seem to be unavailable to hydrates over the strain rates we looked at, and in particular that shear coupling of hydrate grain boundary migration is weak compared to that of ice.

4.3.2 Comparison to other work

Paper III is similar to a study by Cao *et al.* [60] in that is studies the shear properties of ice, and similar to another study by the same author in that it compares ice and hydrate [61]. A difference is that in Paper III we study the gradual change of tilt and quantify the differences, rather than exclusively looking at high-symmetry grain boundaries. The downside of our approach is that we don't cover the same richness of grain boundary combinations. We also show that for ice, tilting the grain boundary a bit away from the direction most suited for basal slip, has consequences, and we observe tilt angle dependence of the ice–ice grain boundary. To our knowledge, this is also the first grain boundary of hydrates to migrate in brute-force molecular dynamics simulations.

The differences we show in molecular dynamics simulations using the *same* interaction potential for ice and hydrate are compatible with experimental

observations: Coarsening of hydrates is orders of magnitude slower than water ice [48], and hydrates subjected to the same strain rate as ice creeps at a higher stress [10]. The magnitude of the difference measured in the latter study is larger than what we measure in Paper III, but the rate-dependence we measure in Paper III is in favor of the relative strength difference increasing with decreasing loading rates.

4.4 Paper IV

Paper IV is Trømborg, J. K. *et al.* Slow slip and the transition from fast to slow fronts in the rupture of frictional interfaces. *Proceedings of the National Academy of Sciences* (2014).

4.4.1 Summary

Paper IV introduces a multi-junction friction law coupled with 2D spring-block elasticity. Under loading conditions that closely match those of an experiment with slow fronts [68], slow fronts emerge spontaneously in this model. We find that the slow fronts are accompanied by slow slip, like in experiments [72], and find a scaling relation between the slow slip speed and the slow front speed.

We find that the mechanism of slow fronts is the following. A precursory event arrests, but the healing of the interface behind the arrest point facilitates slow slip–creep–that drives the slow front. When the slow front reaches a part of the interface with sufficient pre-loading, it speeds up again and continues as a fast crack to the other end of the interface.

In the setting of this thesis, Paper IV serves as an example of how an interface consisting of many micro-contacts can be modeled on a larger scale.

4.5 Paper V

Paper V is Henrik Andersen Sveinsson, Anders Hafreager, Rajiv Kalia, Aiichiro Nakano, Priya Vashishta and Anders Malthe-Sørenssen. Direct atomic simulations of facet formation and equilibrium shapes of SiC nanoparticles (In review in Crystal Growth & Design). I presented an early version of this work at the APS March Meeting 2018, Los Angeles CA.

4.5.1 Summary

In Paper V we use molecular dynamics to simulate the process of shape-changes of silicon carbide nanoparticles. In particular, we study the development of facets on (i) an initially spherical (ii) an initially cylindrical and (iii) an initially cubic nanoparticle at 2200 K.

The initially cubic and spherical particles reach the same shape after some tens of nanoseconds in the simulation. The initially cylindrical nanoparticle does not assume the equilibrium crystal shape in the initial simulation at 2200 K, but

rather an oblated shape, even after 1 µs. In order to reach its equilibrium shape, the particle needs to move material to grow new crystal layers on the largest facet. By heating the particle even closer to the melting point, we push the particle over the energy barrier for normal growth, and it reaches its equilibrium shape, the same shape as the initially cubic and spherical particles reached. This equilibrium shape contains ⟨110⟩ and ⟨111⟩ family facets, with the ⟨110⟩ being the largest ones.

By repeating the heating process from the metastable shape at many temperatures, we use Arrhenius' equation to obtain the energy barrier for the nucleation and growth of a new layer on the nanoparticle.

In the setting of this thesis, Paper V serves as an example of molecular dynamics simulations on a different problem where crystal layers need to grow. For the silicon carbide nanoparticle, we needed a long simulation time and a wisely chosen temperature to make the crystal layers grow, whereas for the hydrate bicrystal in Paper III we needed precisely the right tilt angle to move the grain boundary.

Chapter 5

Outlook

Here I outline possible paths for future research. I have chosen to classify them into straightforward extensions and new approaches. The heuristic for classifying them as straightforward is that I would know where to start and believe that we can find the answer within a reasonable amount of time. For the new approaches I mostly don't have the overview to make such estimates neither on scope, difficulty or viability.

5.0.1 Straightforward extensions

Correlations between cage types and mechanical properties. I think an important next step for hydrate micromechanics is to establish relationships between cage structure and mechanical properties. For instance, how does the cage distribution evolve quantitatively during elastoplastic deformation. Can we use the geometric information of the atomic positions to predict the strength of a hydrate interface without running the forward model? Can the interfacial structure be described by a state parameter to be modeled like friction?

Use new machine-learning trained monatomic water potentials. During the last few months of the work with this thesis, new machine-learning trained potentials with efficiency comparable to mW for water appeared [87]. As soon as these are trained to work with methane hydrates it would be straightforward to redo simulations of this thesis to see whether the mechanisms reported are sensitive to details of the water potential. These new models perform much better than mW, based in the established test by Vega & Abascal [99].

Modeling experimental analog hydrates for more robust comparisons. Experimentalists need to know the differences between the hydrates they are studying in the lab, and the ones the are trying to make predictions about. For phase field models, this has been done to compare methane and xenon hydrates [52]. The same simulations as performed in this thesis could be performed with a different guest molecule.

The role of liquid water and ice on the fracture surface. The system of Paper I could be extended by modeling the fracture of an under-occupied hydrate or by placing water on the hydrate surface in the cavity. Thus the effect of liquid and solid water could be assessed, to see what we can infer about the mechanisms leading to enhanced hydrate decomposition near cracks in water-containing hydrate systems [44, 45].

Crack instabilities. It has been known for a while that the details of molecular interaction potentials are important to crack instabilities [100]. Such instabilities result in crack branching, which increases the fracture area. If such crack instabilities happen in hydrates, and the cracks don't heal, they must have consequences for the dissociation behavior or hydrates. Looking at crack instabilities requires

spatially long systems, so that the crack can accelerate up to a speed where instabilities occur.

5.0.2 New or other approaches

Coarse-graining hydrate–mineral potentials. Since we can generally assume there will be grain size effects with a crossover for grain sizes around 20 nm, it may be worthwhile examining how such a grain size crossover interacts with mineral surfaces. For instance, how does hydrate grain size distributions evolve in nanopores, and what happens at hydrate–mineral–hydrate triple junctions. In experiments, such triple junctions have been associated with a liquid-filled notch [50].

Machine learning structure clustering. Use unsupervised machine learning to see whether structures cluster in other ways than the cage types. Recent advances in crystal structure identification for ices using machine learning [101, 102] paves the way for such crystal structure analysis.

Phase-field description of hydrate polycrystals. Paper II predicts that polycrystals of large methane hydrate crystal grains only suffer damage on the grain boundaries during shear loading and Paper III indicates that hydrate grain boundaries generally don't move on short timescales. Therefore, a phase field description could be used to model larger polycrystals, by a grain boundary field between crystal grains, and describing the interior of grains as an elastic medium. This would require checking more permutations of grain boundaries than we did in Paper III. Possibly, one could create a polycrystal, figure out the crystallography, run molecular dynamics simulations of the grain boundaries that are present, and incorporate that as a phase field. Phase field descriptions has been used to model both hydrate–liquid–gas interfaces [52, 103] and polycrystals of other substances [104].

Bibliography

1. Sloan, E. D. Fundamental principles and applications of natural gas hydrates. *Nature* vol. 426, 353–63 (2003).
2. Busarev, V. V., Tatarnikov, A. M. & Burlak, M. A. Comparison and Interpretation of Spectral Characteristics of the Leading and Trailing Hemispheres of Europa and Callisto. *Solar System Research* vol. 52, 301–311 (2018).
3. Ghosh, J. *et al.* Clathrate hydrates in interstellar environment. *Proceedings of the National Academy of Sciences* vol. 116, 1526–1531 (2019).
4. Hammerschmidt, E. G. Formation of gas hydrates in natural gas transmission lines. *J. Ind. Eng. Chem. (Washington, D. C.)* Vol. 26, 851–855 (1934).
5. Makogon, Y. Hydrate formation in the gas-bearing beds under permafrost conditions. *Gazov. Promst.* Vol. 5. cited By 52, 14–15 (1965).
6. Kvenvolden, K. A., Ginsburg, G. D. & Soloviev, V. A. Worldwide distribution of subaquatic gas hydrates. *Geo-Marine Letters* vol. 13, 32–40 (1993).
7. Andreassen, K. *et al.* Massive blow-out craters formed by hydrate-controlled methane expulsion from the Arctic seafloor. *Science* vol. 356, 948–953 (2017).
8. Warzinski, R. P. *et al.* Dynamic morphology of gas hydrate on a methane bubble in water: Observations and new insights for hydrate film models. *Geophysical Research Letters* vol. 41, 6841–6847 (2014).
9. Jung, J. W. & Santamarina, J. C. Hydrate adhesive and tensile strengths. en. *Geochemistry, Geophysics, Geosystems* vol. 12, Q08003 (2011).
10. Durham, W. B., Kirby, S. H., Stern, L. A. & Zhang, W. The strength and rheology of methane clathrate hydrate. en. *Journal of Geophysical Research: Solid Earth* vol. 108, 2182 (2003).
11. Debenedetti, P. G. & Sarupria, S. Hydrate Molecular Ballet. Vol. 326, 1070–1071 (2009).
12. Walsh, M. R., Koh, C. a., Sloan, E. D., Sum, A. K. & Wu, D. T. Microsecond simulations of spontaneous methane hydrate nucleation and growth. *Science (New York, N.Y.)* Vol. 326, 1095–8 (2009).
13. Sloan, E. D. & Koh, C. a. *Clathrate hydrates of natural gases* (CRC press, 2007).

14. Sassen, R. *et al.* Thermogenic gas hydrates and hydrocarbon gases in complex chemosynthetic communities, Gulf of Mexico continental slope. *Organic Geochemistry* vol. 30, 485–497 (1999).

15. Lu, H. *et al.* Complex gas hydrate from the Cascadia margin. *Nature* vol. 445, 303–306 (2007).

16. Ruppel, C. D. & Kessler, J. D. The interaction of climate change and methane hydrates. *Reviews of Geophysics* vol. 55, 126–168 (2017).

17. Klauda, J. B. & Sandler, S. I. Global distribution of methane hydrate in ocean sediment. *Energy and Fuels* vol. 19, 459–470 (2005).

18. Archer, D., Buffett, B. & Brovkin, V. Ocean methane hydrates as a slow tipping point in the global carbon cycle. *Proceedings of the National Academy of Sciences* vol. 106, 20596–20601 (2009).

19. Boswell, R. & Collett, T. S. Current perspectives on gas hydrate resources. *Energy and Environmental Science* vol. 4, 1206–1215 (2011).

20. Boswell, R. Is gas hydrate energy within reach? *Science* vol. 325, 957–958 (2009).

21. Maslin, M. *et al.* Gas hydrates: Past and future geohazard? *Philosophical Transactions of the Royal Society A: Mathematical, Physical and Engineering Sciences* vol. 368, 2369–2393 (2010).

22. Bugge, T. *et al.* A Giant Three-Stage Submarine Slide Off Norway. *Geo-Marine Letters* vol. 7, 191–198 (1987).

23. Ruppel, C. D. *The U.S. Geological Survey's Gas Hydrates Project* English. Tech. rep. (Reston, VA, 2018).

24. Waite, W. F. *et al.* Physical properties of hydrate-bearing sediments. en. *Reviews of Geophysics* vol. 47, RG4003 (Dec. 2009).

25. Pinkert, S. & Grozic, J. L. H. Failure mechanisms in cemented hydrate-bearing sands. *Journal of Chemical and Engineering Data* vol. 60, 376–382 (2015).

26. Koh, C. A., Sloan, E. D., Sum, A. K. & Wu, D. T. Fundamentals and Applications of Gas Hydrates. *Annual Review of Chemical and Biomolecular Engineering* vol. 2, 237–257 (2011).

27. Conde, M. M. & Vega, C. Determining the three-phase coexistence line in methane hydrates using computer simulations. *The Journal of chemical physics* vol. 133, 064507 (Aug. 2010).

28. Matthews, P. N., Notz, P. K., Widener, M. W. & Prukop, G. Flow Loop Experiments Determine Hydrate Plugging Tendencies in the Field. *Annals of the New York Academy of Sciences* vol. 912, 330–338 (2000).

29. Abascal, J. L. F., Sanz, E., García Fernández, R. & Vega, C. A potential model for the study of ices and amorphous water: TIP4P/Ice. *The Journal of chemical physics* vol. 122, 234511 (June 2005).

30. Hall, K. W., Carpendale, S. & Kusalik, P. G. Evidence from mixed hydrate nucleation for a funnel model of crystallization. *Proceedings of the National Academy of Sciences* vol. 113, 12041–12046 (2016).

31. Abascal, J. L. & Vega, C. A general purpose model for the condensed phases of water: TIP4P/2005. *Journal of Chemical Physics* vol. 123 (2005).

32. Molinero, V. & Moore, E. B. Water modeled as an intermediate element between carbon and silicon. *The journal of physical chemistry. B* vol. 113, 4008–16 (Apr. 2009).

33. Jacobson, L. C. & Molinero, V. A methane-water model for coarse-grained simulations of solutions and clathrate hydrates. *The journal of physical chemistry. B* vol. 114, 7302–11 (June 2010).

34. Moore, E. B. & Molinero, V. Structural transformation in supercooled water controls the crystallization rate of ice. *Nature* vol. 479, 506–508 (Nov. 2011).

35. Jacobson, L. C., Hujo, W. & Molinero, V. Nucleation pathways of clathrate hydrates: effect of guest size and solubility. *The journal of physical chemistry. B* vol. 114, 13796–807 (Nov. 2010).

36. Bi, Y., Porras, A. & Li, T. Free energy landscape and molecular pathways of gas hydrate nucleation. *Journal of Chemical Physics* vol. 145 (2016).

37. Stern, L. a., Kirby, S. H. & Durham, W. B. Polycrystalline Methane Hydrate : Synthesis from Superheated Ice, and Low-Temperature Mechanical Properties. *Energy and Fuels* vol. 12, 201–211 (1998).

38. Yoneda, J., Jin, Y., Katagiri, J. & Tenma, N. Strengthening mechanism of cemented hydrate-bearing sand at microscales. en. *Geophysical Research Letters* vol. 43, 7442–7450 (2016).

39. Wang, B., Socolofsky, S. A., Breier, J. A. & Seewald, J. S. Observations of bubbles in natural seep flares at MC 118 and GC 600 using in situ quantitative imaging. *Journal of Geophysical Research: Oceans,* 2203–2230 (2016).

40. Li, S. L. *et al.* Measurements of hydrate film fracture under conditions simulating the rise of hydrated gas bubbles in deep water. *Chemical Engineering Science* vol. 116, 109–117 (2014).

41. Aman, Z. M., Joshi, S. E., Sloan, E. D., Sum, A. K. & Koh, C. A. Micromechanical cohesion force measurements to determine cyclopentane hydrate interfacial properties. *Journal of Colloid and Interface Science* vol. 376, 283–288 (2012).

42. Brown, E. P. & Koh, C. A. Micromechanical measurements of the effect of surfactants on cyclopentane hydrate shell properties. *Physical Chemistry Chemical Physics* vol. 18, 594–600 (2016).

43. Taylor, C. J., Dieker, L. E., Miller, K. T., Koh, C. A. & Sloan, E. D. Micromechanical adhesion force measurements between tetrahydrofuran hydrate particles. *Journal of Colloid and Interface Science* vol. 306, 255–261 (2007).

44. Takeya, S. *et al.* Nondestructive imaging of anomalously preserved methane clathrate hydrate by phase contrast x-ray imaging. *Journal of Physical Chemistry C* vol. 115, 16193–16199 (2011).

45. Arzbacher, S. *et al.* Macroscopic defects upon decomposition of CO 2 clathrate hydrate crystals. *Physical Chemistry Chemical Physics* vol. 21, 9694–9708 (2019).

46. Hall E. O. The deformation and ageing of mild steel: II Characteristics of the Lüders deformation. *Proceedings of the Physical Society. Section B* vol. 64, 742–747 (1951).

47. Petch, N. The cleavage strength of polycrystals. *Journal of the Iron and Steel Institute* vol. 174, 25–28 (1953).

48. Chaouachi, M., Neher, S. H., Falenty, A. & Kuhs, W. F. Time Resolved Coarsening of Clathrate Crystals: The Case of Gas Hydrates. en. *Crystal Growth & Design* vol. 17, 2458–2472 (2017).

49. DuQuesnay, J. R., Diaz Posada, M. C. & Beltran, J. G. Novel gas hydrate reactor design: 3-in-assessment of phase equilibria, morphology and kinetics. *Fluid Phase Equilibria* vol. 413, 148–157 (2016).

50. Chaouachi, M. *et al.* Microstructural evolution of gas hydrates in sedimentary matrices observed with synchrotron X-ray computed tomographic microscopy. *Geochemistry, Geophysics, Geosystems* vol. 16, 1711–1722 (June 2015).

51. Sanloup, C., Mao, H.-k. & Hemley, R. J. High-pressure transformations in xenon hydrates. *Proceedings of the National Academy of Sciences* vol. 99, 25–28 (2002).

52. Fu, X., Waite, W. F., Cueto-Felgueroso, L. & Juanes, R. Xenon hydrate as an analogue of methane hydrate in geologic systems out of thermodynamic equilibrium. *Geochemistry, Geophysics, Geosystems,* 1–11 (2019).

53. Ripmeester, J. A. Hydrate Research–From Correlations to a Knowledge-based Discipline. *Annals New York Academy of Sciences* vol. 912, 1–16 (2000).

54. Ning, F., Yu, Y., Kjelstrup, S., Vlugt, T. J. H. & Glavatskiy, K. Mechanical properties of clathrate hydrates: status and perspectives. *Energy & Environmental Science* vol. 5, 6779 (2012).

55. Wu, J. *et al.* Mechanical instability of monocrystalline and polycrystalline methane hydrates. *Nature Communications* vol. 6, 8743 (2015).

56. Meyers, M. A., Mishra, A. & Benson, D. J. Mechanical Properties of Nanocrystalline Materials. *Progress in Materials Science* vol. 51, 427–556 (2006).

57. Carlton, C. E. & Ferreira, P. J. What is behind the inverse Hall-Petch effect in nanocrystalline materials? *Acta Materialia* vol. 55, 3749–3756 (2007).

58. Ehre, D. & Chaim, R. Abnormal Hall-Petch behavior in nanocrystalline MgO ceramic. *Journal of Materials Science* vol. 43, 6139–6143 (2008).

59. Ryou, H. *et al.* Below the Hall-Petch Limit in Nanocrystalline Ceramics. *ACS Nano* vol. 12, 3083–3094 (2018).

60. Cao, P. *et al.* Mechanical properties of bi- and poly-crystalline ice. *AIP Advances* vol. 8 (2018).

61. Cao, P., Wu, J., Zhang, Z., Fang, B. & Ning, F. Mechanical Properties of Methane Hydrate: Intrinsic Differences from Ice. *Journal of Physical Chemistry C* vol. 122, 29081–29093 (2018).

62. Shi, Q. *et al.* Role of Guest Molecules in the Mechanical Properties of Clathrate Hydrates. *Crystal Growth and Design* vol. 18, 6729–6741 (2018).

63. Jia, J., Liang, Y., Tsuji, T., Murata, S. & Matsuoka, T. Microscopic Origin of Strain Hardening in Methane Hydrate. *Scientific Reports* vol. 6, 23548 (2016).

64. Jendi, Z. M., Servio, P. & Rey, A. D. Ideal Strength of Methane Hydrate and Ice Ih from First-Principles. *Crystal Growth and Design* vol. 15, 5301–5309 (2015).

65. Vlasic, T. M., Servio, P. & Rey, A. D. Atomistic modeling of structure II gas hydrate mechanics: Compressibility and equations of state. *AIP Advances* vol. 6, 085317 (2016).

66. Thomas, S. L., Chen, K., Han, J., Purohit, P. K. & Srolovitz, D. J. Reconciling grain growth and shear-coupled grain boundary migration. *Nature Communications* vol. 8, 1–12 (2017).

67. Bayart, E., Svetlizky, I. & Fineberg, J. Fracture mechanics determine the lengths of interface ruptures that mediate frictional motion. *Nature Physics* vol. 12, 166–170 (2016).

68. Rubinstein, S., Cohen, G. & Fineberg, J. Detachment fronts and the onset of dynamic friction. *Nature* vol. 430, 1005–1009 (2004).

69. Braun, O. M., Barel, I. & Urbakh, M. Dynamics of transition from static to kinetic friction. *Phys. Rev. Lett.* Vol. 103, 194301 (2009).

70. Bar-Sinai, Y., Spatschek, R., Brener, E. A. & Bouchbinder, E. Instabilities at frictional interfaces: Creep patches, nucleation, and rupture fronts. *Phys. Rev. E* vol. 88, 60403 (2013).

71. Trømborg, J. K. *et al.* Slow slip and the transition from fast to slow fronts in the rupture of frictional interfaces. *Proceedings of the National Academy of Sciences* (2014).

72. Ben-David, O., Rubinstein, S. M. & Fineberg, J. Slip-stick and the evolution of frictional strength. *Nature* vol. 463, 76–79 (2010).

73. Einstein, T. L. eng. in *Handbook of crystal growth. Vol. 1 Pt. B: Fundamentals Transport and stability* (ed Nishinaga, T.) 2. ed, 215–264 (Elsevier, Amsterdam, 2015).

74. Mullins, W. W. & Rohrer, G. S. Nucleation Barrier for Volume-Conserving Shape Changes of Faceted Crystals. en. *Journal of the American Ceramic Society* vol. 83, 214–16 (Jan. 2000).

75. Combe, N., Jensen, P. & Pimpinelli, A. Changing shapes in the nanoworld. *Physical Review Letters* vol. 85, 110–113 (2000).

76. Parrinello, M. & Rahman, a. Polymorphic Transitions in Single Crystals: a New Molecular Dynamics Method. *Journal of Applied Physics* vol. 52, 7182–7190 (1981).

77. Nosé, S. A unified formulation of the constant temperature molecular dynamics methods. *The Journal of Chemical Physics* vol. 81, 511–519 (1984).

78. Hoover, W. G. Canonical dynamics: Equilibrium phase-space distributions. *Physical Review A* vol. 31, 1695–1697 (1985).

79. Plimpton, S. Fast Parallel Algorithms for Short – Range Molecular Dynamics. *Journal of Computational Physics* vol. 117, 1–19 (1995).

80. Tuckerman, M. E., Alejandre, J., López-Rendón, R., Jochim, A. L. & Martyna, G. J. A Liouville-operator derived measure-preserving integrator for molecular dynamics simulations in the isothermal-isobaric ensemble. *Journal of Physics A: Mathematical and General* vol. 39, 5629–5651 (2006).

81. Anderson, P. W. More is different. *Science* vol. 76, 30–33 (1972).

82. Cipcigan, F. S., Sokhan, V. P., Crain, J. & Martyna, G. J. Electronic coarse graining enhances the predictive power of molecular simulation allowing challenges in water physics to be addressed. *Journal of Computational Physics* vol. 326, 222–233 (2016).

83. Stillinger, F. H. & Weber, T. a. Computer simulation of local order in condensed phases of silicon. *Physical Review B* vol. 31, 5262–5271 (1985).

84. Shimizu, H., Kumazaki, T., Kume, T. & Sasaki, S. Elasticity of single-crystal methane hydrate at high pressure. *Physical Review B - Condensed Matter and Materials Physics* vol. 65, 1–4 (2002).

85. Franco Pinheiro Moreira, P. A., Gomes De Aguiar Veiga, R. & De Koning, M. Elastic constants of ice I h as described by semi-empirical water models. *Journal of Chemical Physics* vol. 150 (2019).

86. Guo, Q., Ghaani, M. R., Nandi, P. K. & English, N. J. Pressure-Induced Densification of Ice Ih under Triaxial Mechanical Compression: Dissociation versus Retention of Crystallinity for Intermediate States in Atomistic and Coarse-Grained Water Models. *Journal of Physical Chemistry Letters* vol. 9, 5267–5274 (2018).

87. Chan, H. *et al.* Machine learning coarse grained models for water. *Nature Communications* vol. 10, 1–14 (2019).

88. Stukowski, A. Visualization and analysis of atomistic simulation data with OVITO-the Open Visualization Tool. *Modelling and Simulation in Materials Science and Engineering* vol. 18 (2010).

89. Nguyen, A. H. & Molinero, V. Identification of Clathrate Hydrates, Hexagonal Ice, Cubic Ice, and Liquid Water in Simulations: the CHILL+ Algorithm. *The Journal of Physical Chemistry B* vol. 119, 9369–9376 (2015).

90. Dragly, S.-A., Mobarhan, M. H. & Lepperød, M. E. Experimental Directory Structure (Exdir): An Alternative to HDF5 Without Introducing a New File Format. Vol. 12, 1–13 (2018).

91. Wilkinson, M. D. *et al.* The FAIR Guiding Principles for scientific data management and stewardship. *Scientific Data* vol. 3, 160018 (2016).

92. Else, H. Radical open-access plan could spell end to journal subscriptions. *Nature* vol. 561, 17–18 (2018).

93. Chen, X. *et al.* Open is not enough. *Nature Physics* vol. 15, 113–119 (2019).

95. Vanel, L., Ciliberto, S., Cortet, P.-P. & Santucci, S. Time-dependent rupture and slow crack growth: elastic and viscoplastic dynamics. *Journal of Physics D: Applied Physics* vol. 42, 214007 (Nov. 2009).

99. Vega, C. & Abascal, J. L. F. Simulating water with rigid non-polarizable models: a general perspective. *Physical Chemistry Chemical Physics* vol. 13, 19663 (2011).

100. Buehler, M. J. & Gao, H. Dynamical fracture instabilities due to local hyperelasticity at crack tips. *Nature* vol. 439, 307–310 (2006).

101. Spellings, M. & Glotzer, S. C. Machine learning for crystal identification and discovery. *AIChE Journal* vol. 64, 2198–2206 (2018).

102. Reinhart, W. F. & Panagiotopoulos, A. Z. Automated crystal characterization with a fast neighborhood graph analysis method. *Soft Matter* vol. 14, 6083–6089 (2018).

103. Fu, X., Cueto-Felgueroso, L. & Juanes, R. Nonequilibrium Thermodynamics of Hydrate Growth on a Gas-Liquid Interface. *Physical Review Letters* vol. 120, 144501 (2018).

104. Gránásy, L. *et al.* Phase-field modeling of polycrystalline solidification: From needle crystals to spherulites - A review. *Metallurgical and Materials Transactions A: Physical Metallurgy and Materials Science* vol. 45, 1694–1719 (2014).

Papers

Paper I

Molecular-scale thermally activated fractures in methane hydrates: A molecular dynamics study

Henrik Andersen Sveinsson and Anders Malthe-sørenssen

In: *Physical Chemistry Chemical Physics*

PCCP

PAPER

View Article Online
View Journal

Cite this: DOI: 10.1039/c9cp01337g

Molecular-scale thermally activated fractures in methane hydrates: a molecular dynamics study†

Henrik Andersen Sveinsson * and Anders Malthe-Sørenssen

Received 8th March 2019,
Accepted 28th May 2019

DOI: 10.1039/c9cp01337g

rsc.li/pccp

We perform multiple large molecular dynamics simulations to study the fracture behaviour of monocrystalline methane hydrates under tension. We examine the fracture initiation phase and find that the fracture process can be divided into two phases: slow crack growth and rapid crack propagation. The time of the slow crack growth phase can be predicted by a thermal activation model [L. Vanel *et al.*, *J. Phys. D: Appl. Phys.*, 2009, **42**, 214007] where an energy barrier has to be overcome in order for the crack to propagate. Our simulations predict that the slow growth phase vanishes when the stress intensity factor approaches $K_{\mathrm{Ic}} = 0.08\ \mathrm{MPa}\sqrt{\mathrm{m}}$.

Introduction

Clathrates are substances consisting of a lattice trapping-enclathrating-molecules. Gas hydrates are realizations of clathrates where the lattice is made up of water molecules and the enclathrated molecules would be gaseous under standard atmospheric conditions. The most common gas hydrate is the methane hydrate. Methane hydrates form out of an aqueous methane solution at moderate pressure and low temperature conditions.[1] They are common in marine sediments on continental margins and in the arctic tundra, where these conditions are prevalent.[2]

Hydrates make up an important, sometimes essential, part of the mechanical and failure properties of hydrate bearing sediments.[3] In particular, hydrates make their surrounding sediments sensitive to pressure and temperature changes that may result either from geological driving forces, such as climate change or resource exploitation. Producing natural gas from methane hydrates is inherently different from producing from a conventional reservoir with a porous matrix, since the process destroys solid material. This destruction of the sediment itself has mechanical consequences, and it is therefore crucial to establish the strength of hydrate-bearing sediments under changing thermodynamic conditions.

Methane is frequently found to seep out of reservoirs below the seafloor.[4] Under the right thermodynamic circumstances, this leads to hydrate crusted methane bubbles rising in the water column. These bubbles may persist for longer periods of time, even though they are thermodynamically unstable, because the initial creation of a hydrate shell shuts of the methane supply, hindering further growth.[5] Such bubbles show clearly visible crack-like damage as they move in the water column both in nature[4] and in controlled experiment.[6] These cracks have been hypothesized to play an important role in bubble gas exchange. The mechanical response of hydrate crusted bubbles at rest has been studied more in detail experimentally,[7] but it remains difficult to obtain accurate data, and the detailed mechanisms on the molecular level remain experimentally unavailable.

Beyond Earth, hydrates have been suggested to be of importance to ice shell thickness of Jupiter's moon Europa,[8] since the lower thermal conductivity of clathrates[9] would isolate the heat generated by tidal flexing more efficiently than pure water ice. The presence of methane hydrates have been inferred on Europa based on reflectance spectra.[10] Estimates of seismic activity on Europa have been made, based on tidal cracking of the ice shell,[11] and these estimates would have to be adjusted if it turns out that Europa's icy shell contains a significant proportion of clathrates.

All of these phenomena rely on the mechanical and failure properties of methane hydrates. Due to the high water content and hydrogen-bonded nature of clathrates, one could expect the mechanical properties to be similar to those of ice. However, experiments have shown that methane hydrates are more than an order of magnitude more creep resistant than ice.[12] Therefore, fundamental micro-mechanical properties of methane hydrates have to be established specifically. Micro-mechanical properties of pure methane hydrates are largely unknown because measuring the failure properties of methane hydrates experimentally is hard.[13]

Molecular dynamics simulations can provide important complementary information to the problem, suggest mechanisms, and shed light on the following rather simple question: What is the behaviour of small cracks in methane hydrates when they are close to mechanical failure conditions?

The NJORD Centre, Department of Physics, University of Oslo, Norway.
E-mail: henriasv@fys.uio.no

† Data set available from Zenodo, http://doi.org/10.5281/zenodo.3229900

Previous molecular-scale modeling studies of the mechanical properties of hydrates have explained the strain hardening of polycrystalline systems[14] and the mechanical and tensile failure of perfect monocrystalline crystal lattices.[15–17] However, the failure of monocrystalline hydrates with preexisting flaws have not been studied. This is the fracture mechanics way: using an imperfect sample to account for the way materials actually fail, through the growth of existing impurities. A notch impurity may for instance form at the triple junction between two hydrate monocrystals and a mineral surface.[18]

In this paper, we describe the fracture initiation process in crystalline methane hydrates from direct molecular dynamics simulations of samples with a penny-shaped crack. We find that the failure initiation can be divided into two phases: slow crack growth and rapid crack propagation, and that the slow phase can be explained as thermally activated brittle fracture. The waiting time associated with this slow phase follows a simple Arrhenius-based functional relationship[19] incorporating the stress and the temperature of the hydrate. The range of stresses that result in a thermally activated fracture is wide enough for failure to happen at stresses well below the nominal fracture toughness.

Simulations

To study the failure of monocrystalline methane hydrates, we performed large-scale molecular dynamics simulations of the fracture initiation in flawed hydrate single crystals. We prepared an unstrained cubic sample with $L = 29$ nm of structure I methane hydrate at full occupancy and introduced a controlled flaw in the hydrate cube. This flaw was an 8 nm wide oblate ellipsoidal cavity at the centre of the sample. The system was equilibrated at a designated temperature, and then gradually subjected to uniaxial strain normal to the major plane of the ellipsoidal cavity to induce mechanical failure. The simulation setup is shown in Fig. 1.

When the uniaxial strain reaches a sufficient level, the sample fails by fracturing. Snapshots from a typical crack propagation event are shown in Fig. 2. The crack evolves by opening subsequent hydrate cages, and all material destruction happens in the failure plane, that is with no dislocations away from the crack, thus the hydrate behaves brittle under our simulation conditions.

Quantification–scaling relation

To systematically determine the effect of the temperature and the strain on the fracture initiation, we performed multiple simulations with temperatures ranging from 120 K to 325 K and strains from 4.9% to 7.3%. The choice of the strain level is particular to the geometry of the system; the combination of the system size and crack length were chosen in order to give a stress intensity that allows us to study the fracture initiation phase on the timescales of molecular dynamics simulations. The general trend from this series of simulations is that warm and highly strained samples fail immediately, or even before the strain has reached its final value, and that cold samples

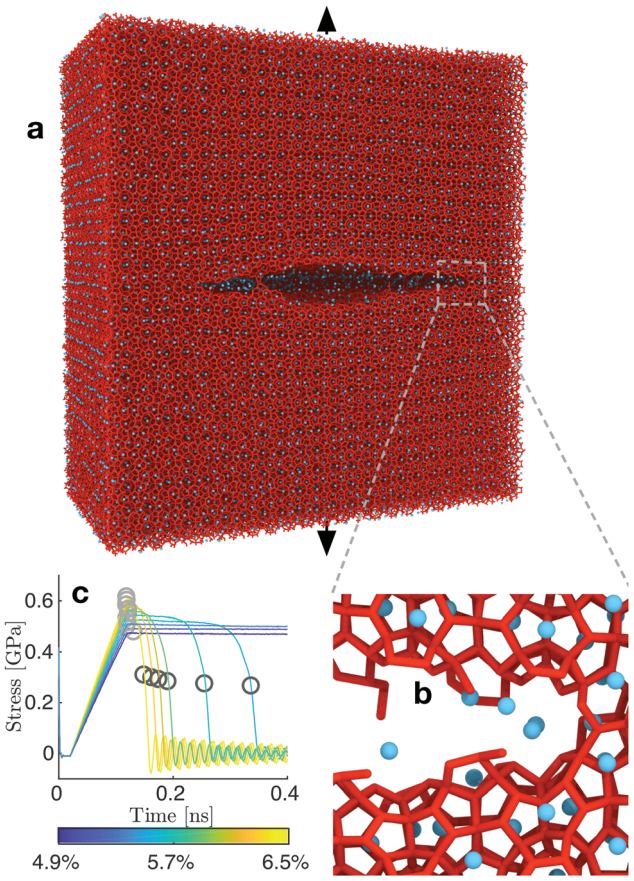

Fig. 1 Modeled system (a) and close-up of the crack (b). (a) is the system cut in half to show the crack. (c) Tensile stress through time in several simulations at 280 K. The stress decreases after applying strain, and the plot shows that the stress decrease can be divided into a slow phase and a rapid phase. Furthermore, high strains lead to high stresses and a short slow phase, whereas lower strains lead to lower stresses and longer slow phases of the crack development. The light gray markers indicate the point of largest stress, and the dark grey markers indicate the measured corresponding waiting time for fracture. Colors of the curves indicate the strain applied to the system during the loading phase.

subjected to a low strain do not fail at all during the simulation. For samples at an intermediate stress level, however, the crack development can be separated into two distinct phases: slow crack growth and rapid crack propagation. This shows up in the time-evolution of the tensile stress in the system after straining (Fig. 1c). A relatively long phase of slow crack evolution can be seen from the slowly decreasing tensile stress. Then, a relatively short period of fast crack propagation can be seen from a sudden and rapid stress decrease. At some point, the crack spans a whole plane of the simulation box, at which point the sample has been divided into two parts and vibrates such that the measured tensile stress fluctuates around zero. Furthermore, the crack growth during the slow crack evolution looks irreversible in all of our simulations – the crack area is growing monotonously.

To quantify this behaviour, we measure the waiting time, t_w, from the conclusion of the ramp up of strain until a critical crack has developed. Because the slow crack evolution phase is

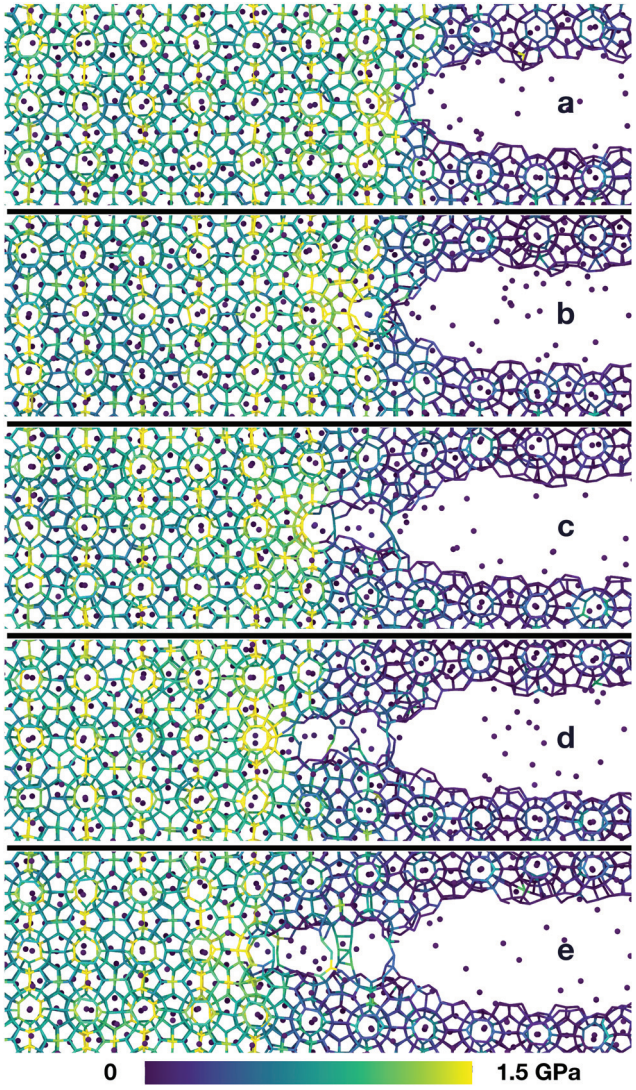

Fig. 2 Molecular mechanism during fracture along the (001) plane. First, a small cage opens (a), then a large one (b). In (c) we see how the stress concentrates on a half-cage when a large cage is open on one side, but not yet broken on the other side. Panels (d) and (e) show that this process continues, and that the cages open sequentially. There are no dislocations forming far from the crack tip, and there is no reformation of the hydrate after a cage has opened. The colors indicate the virial stress in the direction of the applied tension, averaged over 1 ps. The snapshots are taken from a simulation at 280 K with a maximum strain level of 5.7%. The stress peak moves as the crack propagates.

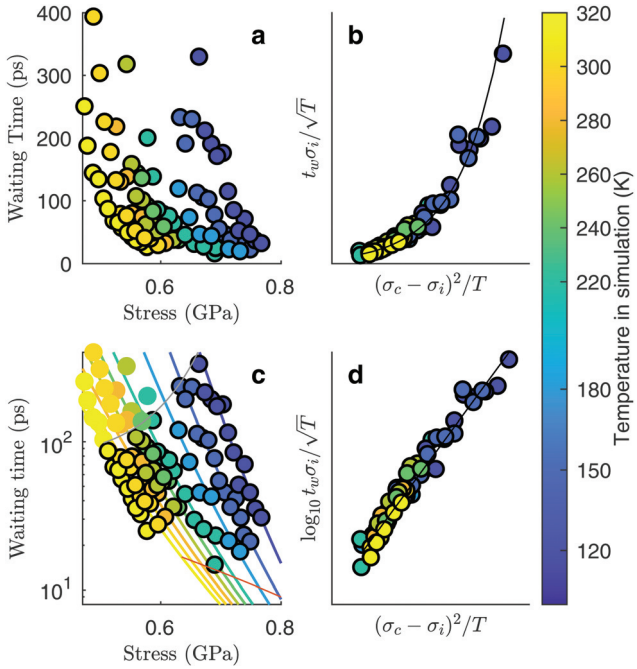

Fig. 3 Slow cracks follow the equation of thermally activated brittle fracture. Simulations at different temperatures according to the colour bar. (a) Waiting time from maximum stress to the stress has fallen to half of that maximum value, as measured in Fig. 1c, but with more data points. (b) Data collapses onto a common scaling function. (c) Data points plotted together with the fitted functional relationship. The validity range of the local elastic barrier model is the region between the gray lines, and points within this range are drawn with a black border. The region below the lower line is the region where the energy requirement does not hold, and the region above the upper line is the region where the initial crack length requirement does not hold. Only points within the validity range are included in the subsequent fitting of the data to the model. (d) A linear data collapse on a logarithmic y-axis shows that the scaling function is an exponential function.

the relatively longer period, we define t_w as the time it takes for the tensile stress along the axis of applied strain to be reduced from its maximum level (typically when straining stops) to half of that maximum value. Whether we choose half of the maximum stress level or a different fraction is unimportant, since the fast stress drop associated with rapid fracture is much more abrupt than the slow stress drop associated with slow cracks. The measured waiting times as a function of the applied stress for different temperatures are shown in Fig. 3a. It shows that the waiting time decreases with maximum stress for a given temperature. Also, the waiting time decreases with increasing temperature for a given stress. Interestingly, we see that over the relatively short range of waiting times that are accessible when doing many large-scale simulations, the maximum stresses vary by almost a factor of two.

To obtain the functional relationship between the waiting time, the maximum stress level and the temperature, we try to explain our data by a thermal activation model. This means we expect a process supporting crack growth to operate at a rate given by Arrhenius' equation: $k \propto e^{\Delta U/k_B T}$, with ΔU an energy barrier, T the system temperature and k_B the Boltzmann constant. For crack propagation, the relevant energy barrier is the energy difference between the system at its actual stress level and the system at its nominal critical stress level. A detailed calculation of such a waiting time, assuming irreversible fracture propagation that has to overcome a local elastic barrier leads to the following model:[19]

$$t_w = A(T, l_i, \sigma_i) \exp\left(\frac{\Delta U(\sigma_c, \sigma_i)}{k_B T}\right) \quad (1)$$

$$= \frac{l_i}{\sigma_i v_0}\sqrt{\frac{2\pi Y T k_B}{V}} \exp\left(\frac{(\sigma_c - \sigma_i)^2 V}{2 Y k_B T}\right), \quad (2)$$

where l_i is the initial crack length, σ_i the initial stress near the crack tip, σ_c the critical (failure) stress level near the crack tip, v_0 a characteristic propagation velocity, Y the Young's modulus, T the system temperature, k_B the Boltzmann constant and V an activation volume. This equation is valid when the energy barrier is sufficiently big compared to the temperature, $(\sigma_c - \sigma_i)^2 V \gg 2Yk_BT$ and when the initial crack length is close to the crack length at which the system would fail immediately, that is the critical crack length, $l(\sigma_c) \sim l(\sigma_i)$. We indicate in Fig. 3c what points fulfill these conditions with $\frac{(\sigma_c - \sigma_i)^2 V}{2Yk_BT} > e$ and $\frac{l(\sigma_c)}{l(\sigma_i)} < 1 - \frac{1}{e}$. The stresses σ_c and σ_i are stresses over the activation volume.

The values of the parameters of eqn (2) translated to the present study are as follows: the initial crack length is a the width of the initial flaw we introduce, l_i = 8 nm. Youngs modulus for the force field we use has been reported to vary between 9.71 GPa at 283.15 K to 7.68 GPa at 200 K.[14] For simplicity in the scaling analysis, we choose to regard the Young's modulus as constant, Y = 9 GPa, since the temperature variation is a second order effect. V and v_0 are model parameters that will be determined by the subsequent scaling analysis.

The activation energy, ΔU, can also be written in terms of the stress intensity factor, and therefore in terms of the faraway stress (in our case the stress over the simulation cell) and the crack length:

$$\Delta U = \frac{(K_c - K_i)^2 V}{2Y\lambda} = \frac{V}{2Y}\left(\sigma\sqrt{\frac{2l_c}{\pi\lambda}} - \sigma\sqrt{\frac{2l_i}{\pi\lambda}}\right)^2, \qquad (3)$$

where λ is the cut-off length of stress divergence due to the discrete nature of matter on atomic scales. The rightmost expression above assumes the stress intensity factor of the penny-shaped crack under tension on an infinite domain, $K = \sigma\sqrt{\frac{2l}{\pi}}$ (see *e.g.* Anderson[20]). This form of the activation energy resolves an apparent unphysical property of eqn (2), namely that the waiting time seems to be proportional to the initial crack length. Using the latter form of the activation energy, we see that an increase in the initial crack length results in a smaller energy barrier.

We choose λ = 3 Å because this is approximately the distance between water molecules in hydrates and thus the cut-off distance of the hydrogen-bonding. We then insert $\sigma_i = \sigma\sqrt{\frac{2l_i}{\pi\lambda}}$ in the scaling analysis, and try to choose an appropriate value for our only fitting parameter, $\sigma_c = \sigma\sqrt{\frac{2l_c}{\pi\lambda}}$, in order to make the data collapse onto a common scaling function. If such a common scaling function is consistent with eqn (2), we may calculate the characteristic propagation velocity v_0 and the activation volume V from the parameters obtained when fitting the data to eqn (2).

We find that the data collapse onto a common scaling function for σ_c = 4.7 GPa on the axes shown in Fig. 3b. Note that this value is much larger than the stresses measured over the simulation box (Fig. 3a and c). This is due to stress concentration. The simulation cell stress corresponding to this number is σ = 1.15 GPa, giving an estimate of which stress level would make the waiting time vanish in the local elastic barrier model for a methane hydrate with an 8 nm penny-shaped crack. We may also express this in terms of the stress intensity factor, which gives us an upper limit of the fracture toughness: $K_{Ic} = 0.08\ \text{MPa}\sqrt{\text{m}}$ for this molecular hydrate model. This value is close to the experimentally reported fracture toughness of water ice, which typically comes out around $K_{Ic} = 0.1\ \text{MPa}\sqrt{\text{m}}$.[21,22] The data collapse indicates that we have chosen the right governing parameters, and the linearity of the collapsed data on logarithmic axes (Fig. 3d) shows that the data is consistent with an exponential functional form.

Even though the functional form of the waiting time is an exponential function, the variance of the data compared to the fit line is lower that one would expect from an exponential distribution. This indicates that the failure of the system is the result of several successive bond opening events, rather than a single activation event. This is in line with the assumptions of the local elastic barrier model: The crack is assumed to maintain a slow propagation velocity v for some time. Our simulations therefore provide an estimate for the relation between stress, σ_i, temperature, T, and the time until failure, t_w:

$$\frac{t_w\sigma_i}{\sqrt{T}} = A\exp\left(\frac{B(\sigma_c - \sigma_i)^2}{T}\right), \qquad (4)$$

with $A = \sqrt{\frac{2\pi Yk_B}{V}}\frac{l_i}{v_0}$ and $B = \frac{V}{2Yk_B}$.

The data collapse allows us to extract parameters to be used to compare the effect of thermally activated cracks to other mechanisms of failure and deformation. By fitting the collapsed data to eqn (4) we find $A = 1.6 \times 10^{-4}\ \text{s Pa}/\sqrt{\text{K}}$ and $B = 1.9 \times 10^{-16}\ \text{kPa}^{-2}$. Since the model formula includes both the length of the initial cavity and the critical stress level, these parameters should hold when changing the system size, allowing for the prediction of thermal activation times of larger hydrate systems. We can also estimate the values of v_0 and V. By rearranging the expressions for A and B, we find that $V^{1/3}$ = 3.6 Å, which is consistent with the thermal activation process happening on the scale of hydrate cages and hydrogen bonds. We also find the characteristic propagation velocity v_0 = 6.3 km s^{-1}. Since this value is on the same order of magnitude as the sound velocity in the material, it suggests an attempt rate on the order of the natural oscillation frequency of the crystal lattice.

Simulation details

We performed a series of simulation using the mW water potential combined with a united atom methane model.[23] All simulations were performed using LAMMPS.[24] The equations of motion were integrated using the Velocity Verlet scheme with a timestep of 10 fs. We performed simulations using the following procedure: a methane hydrate in the sI structure at full occupancy was initialized. Atoms were then deleted in the cavity region, which was an oblate ellipsoid with a major plane

of diameter 8 nm parallel to the (001) crystal plane, and a height of 1.2 nm. Mathematically, this cavity can be represented as $\frac{x-x_0}{a}+\frac{y-y_0}{a}+\frac{z-z_0}{c}<1$ with a = 4 nm, c = 0.6 nm and (x_0, y_0, z_0) being the geometrical center of the simulated system. Particle velocities were set to the Boltzmann distribution at $1.8T$ with T the wanted system temperature, since approximately half of the kinetic energy will move to the potential degrees of freedom during equilibration. The system was then allowed to equilibrate during 20 ps subjected to a Nosé–Hoover thermo-barostat (*NPT*) at P = 10 MPa with time constants of 2 ps. This equilibration was performed to allow the hydrate to assume its preferred shape at the temperature of that simulation. After equilibration, the barostat was turned off, while the thermo-couple was kept on, but with the simulation box expanding in the z direction to induce a prescribed strain level on the hydrate sample during 100 ps. Expansion was turned off upon arrival at the prescribed strain level, and the simulation was then continued at constant volume with the thermo-couple still on. To reach strains of 4.9–7.3% in 100 ps, we applied a strain rate of $4.9–7.3 \times 10^8$ s^{-1}. We chose to use a high strain rate to get the system quickly to a strained state without allowing the crack to start propagating before the prescribed strain level was reached. At the same time, the strain rate was chosen sufficiently low to prevent oscillations of the whole system. The stress–strain curves of Fig. 1c show that there are no significant stress oscillations in the bulk, and the upward slope of the stress–strain curve is much steeper just before expansion is turned off than just after, showing that the loading phase and the waiting phase do not interfere significantly. For further details, see LAMMPS input scripts and thermodynamic output data from the simulations.†

Discussion

We have shown simulations indicating that the mechanical failure of a methane hydrate crystal can happen at loads well below the nominal fracture toughness of the hydrate, and thermally activated fracture leads to catastrophic failure of a sample under high stress. Furthermore, the duration of the slow thermal initiation phase before rapid fracture obeys consistently and accurately a simple functional relationship. From visual inspection of the simulations, we could have anticipated this because we see that the structure decomposes cage by cage in an irreversible manner as seen in Fig. 2.

Due to the limited spatial range of molecular dynamics simulations, sizes are small, timescales short and the stresses high in this study. This does not mean that the stresses must be this high to observe the effects of thermal activation in a laboratory setting, where the stresses are on the order of MPa or tens of MPa.[25] The relevant parameter for observing this effect is stress intensity, *i.e.* the stress near the crack tip. Stress intensity goes like $\sqrt{l}$, where l is the size of flaws in the material subjected to stress. Extrapolating with this formula yields that materials with flaws of for instance 1 μm will reach the same stress intensity as our simulations at a stress of around 20 MPa, which is a relevant stress in a natural hydrate setting. For instance, the dissociation of hydrates itself can increase the pore pressure by tens of megapascals in tight sediments.[26] Increasing the flaw size and reducing the stress level within the validity range of the local elastic barrier model should lead to longer waiting times, and in the above-mentioned extrapolation scenario, the waiting time would translate to around 0.1 μs. When the timescale increases, the effect of dissociation may become important, so one should for instance consider whether dissociation of the hydrate could interfere with the crack propagation, either by promoting crack growth or by blunting the crack.

Further progress in understanding hydrates in nature from a microscopical scale depends on also studying shear properties of hydrates, both in monocrystalline, bi-crystalline and polycrystalline systems. Shear is fundamentally different from tension, since it allows for inducing mechanical failure without changing the confining pressure, and thus failure of the hydrate can be studied without worrying about going outside the stability thermodynamic conditions of the hydrate. Shear also allows for a thorough study of grain boundary sliding properties of hydrate interfaces. That could be pure hydrate–hydrate interfaces with some crystal mismatch to create a grain boundary, or interfaces that combine hydrates with other substances such as minerals, water and water ice, which are coexisting with hydrates in natural reservoirs.[3]

Finally, we want to stress the fracture mechanics approach. Stresses concentrate around preexisting weaknesses, leading to materials becoming much weaker than one would expect from the strength of atomic bonds. Therefore, when possible, strengths should be reported in fracture toughness rather than fracture stress. This is of course not always viable, for instance when the size of preexisting cracks is unknown. But from a fracture mechanics point of view, it is unsurprising that the strength of hydrates is reported to be relatively weak in experiments,[25] stronger in molecular dynamics simulations,[14] and even stronger in DFT simulations.[27]

Conflicts of interest

There are no conflicts to declare.

Acknowledgements

This work was financially supported by the Research Council of Norway, FRINATEK, grant number 231621. Some of the simulations were performed using computer resources provided by Notur, project number NN9272K.

References

1 E. D. Sloan, *Nature*, 2003, **426**, 353–363.
2 C. D. Ruppel and J. D. Kessler, *Rev. Geophys.*, 2017, **55**, 126–168.
3 W. F. Waite, J. C. Santamarina, D. D. Cortes, B. Dugan, D. N. Espinoza, J. Germaine, J. Jang, J. W. Jung, T. J. Kneafsey,

H. Shin, K. Soga, W. J. Winters and T.-S. Yun, *Rev. Geophys.*, 2009, **47**, RG4003.
4 B. Wang, S. A. Socolofsky, J. A. Breier and J. S. Seewald, *J. Geophys. Res.: Oceans*, 2016, 2203–2230.
5 X. Fu, L. Cueto-Felgueroso and R. Juanes, *Phys. Rev. Lett.*, 2018, **120**, 144501.
6 R. P. Warzinski, R. Lynn, I. Haljasmaa, I. Leifer, F. Shaffer, B. J. Anderson and J. S. Levine, *Geophys. Res. Lett.*, 2014, **41**, 6841–6847.
7 S. L. Li, C. Y. Sun, G. J. Chen, Z. Y. Li, Q. L. Ma, L. Y. Yang and A. K. Sum, *Chem. Eng. Sci.*, 2014, **116**, 109–117.
8 K. P. Hand, C. F. Chyba, R. W. Carlson and J. F. Cooper, *Astrobiology*, 2006, **6**, 463–482.
9 E. D. Sloan and C. A. Koh, *Clathrate hydrates of natural gases*, CRC Press, 2007.
10 V. V. Busarev, A. M. Tatarnikov and M. A. Burlak, *Sol. Syst. Res.*, 2018, **52**, 301–311.
11 M. P. Panning, S. C. Stähler, H. H. Huang, S. D. Vance, S. Kedar, V. C. Tsai, W. T. Pike and R. D. Lorenz, *J. Geophys. Res.: Planets*, 2018, **123**, 163–179.
12 W. B. Durham, S. H. Kirby, L. A. Stern and W. Zhang, *J. Geophys. Res.: Solid Earth*, 2003, **108**, 2182.
13 F. Ning, Y. Yu, S. Kjelstrup, T. J. H. Vlugt and K. Glavatskiy, *Energy Environ. Sci.*, 2012, **5**, 6779.
14 J. Wu, F. Ning, T. T. Trinh, S. Kjelstrup, T. J. H. Vlugt, J. He, B. H. Skallerud and Z. Zhang, *Nat. Commun.*, 2015, **6**, 8743.
15 P. Cao, J. Wu, Z. Zhang, B. Fang and F. Ning, *J. Phys. Chem. C*, 2018, **122**, 29081–29093.
16 J. Jia, Y. Liang, T. Tsuji, S. Murata and T. Matsuoka, *Sci. Rep.*, 2017, **7**, 1–11.
17 J. Jia, Y. Liang, T. Tsuji, S. Murata and T. Matsuoka, *Sci. Rep.*, 2016, **6**, 23548.
18 M. Chaouachi, A. Falenty, K. Sell, F. Enzmann, M. Kersten, D. Haberthür and W. F. Kuhs, *Geochem., Geophys., Geosyst.*, 2015, **16**, 1711–1722.
19 L. Vanel, S. Ciliberto, P.-P. Cortet and S. Santucci, *J. Phys. D: Appl. Phys.*, 2009, **42**, 214007.
20 T. L. Anderson, *Fracture Mechanics: Fundamentals and Applications*, 3rd edn, 2005, p. 640.
21 H. W. Liu and K. J. Miller, *J. Glaciol.*, 1979, **22**, 135–143.
22 P. P. Benham, R. J. Crawford and C. G. Armstrong, *Mechanics of engineering materials*, Longman, Harlow, 1996.
23 L. C. Jacobson and V. Molinero, *J. Phys. Chem. B*, 2010, **114**, 7302–7311.
24 S. Plimpton, *J. Comput. Phys.*, 1995, **117**, 1–19.
25 J. W. Jung and J. C. Santamarina, *Geochem., Geophys., Geosyst.*, 2011, **12**, Q08003.
26 W. Xu and L. N. Germanovich, *J. Geophys. Res.*, 2006, **111**, B01104.
27 T. M. Vlasic, P. Servio and A. D. Rey, *AIP Adv.*, 2016, **6**, 085317.

Paper IV

Slow slip and the transition from fast to slow fronts in the rupture of frictional interfaces

Jørgen Kjoshagen Trømborg, Henrik Andersen Sveinsson, Julien Scheibert, Kjetil Thøgersen, David Skålid Amundsen, Anders Malthe-Sørenssen

In: *Proceedings of the National Academy of Sciences of the United States of America*, **111**, 24 (2014).
http://dx.doi.org/10.1073/pnas.1321752111

IV

Slow slip and the transition from fast to slow fronts in the rupture of frictional interfaces

Jørgen Kjoshagen Trømborg[a,b], Henrik Andersen Sveinsson[a], Julien Scheibert[b,1], Kjetil Thøgersen[a], David Skålid Amundsen[c], and Anders Malthe-Sørenssen[a,1]

[a]Department of Physics, University of Oslo, 0316 Oslo, Norway; [b]Laboratoire de Tribologie et Dynamique des Systèmes, Centre National de la Recherche Scientifique, Ecole Centrale de Lyon, 69134 Ecully, France; and [c]Astrophysics Group, School of Physics, University of Exeter, Exeter EX4 4QL, United Kingdom

Edited by Jay Fineberg, The Hebrew University of Jerusalem, Jerusalem, Israel, and accepted by the Editorial Board May 2, 2014 (received for review November 26, 2013)

The failure of the population of microjunctions forming the frictional interface between two solids is central to fields ranging from biomechanics to seismology. This failure is mediated by the propagation along the interface of various types of rupture fronts, covering a wide range of velocities. Among them are the so-called slow fronts, which are recently discovered fronts much slower than the materials' sound speeds. Despite intense modeling activity, the mechanisms underlying slow fronts remain elusive. Here, we introduce a multiscale model capable of reproducing both the transition from fast to slow fronts in a single rupture event and the short-time slip dynamics observed in recent experiments. We identify slow slip immediately following the arrest of a fast front as a phenomenon sufficient for the front to propagate further at a much slower pace. Whether slow fronts are actually observed is controlled both by the interfacial stresses and by the width of the local distribution of forces among microjunctions. Our results show that slow fronts are qualitatively different from faster fronts. Because the transition from fast to slow fronts is potentially as generic as slow slip, we anticipate that it might occur in the wide range of systems in which slow slip has been reported, including seismic faults.

friction | multiscale modeling | onset of sliding | stick–slip

The rupture of frictional interfaces is a central mechanism in many processes, including snow slab avalanches, human object grasping, and earthquake dynamics (1). Rupture occurs through the propagation of a crack-like microslip front—the rupture front—across the interface. This front represents the moving boundary between a stick region and a slipping region that coexist within the interface plane. In so-called partial-slip situations, fronts propagate quasistatically at a pace controlled by the external loading, as studied in mechanical engineering for decades (2, 3). Recently, fast cameras enabled the observation of much faster fronts, which are classified into three types: supershear fronts faster than the material's shear wave speed c_s, sub-Rayleigh fronts propagating at velocities close to c_s, and slow fronts much slower than c_s (4–8). Whereas the first two types have been predicted theoretically, the physical mechanisms underlying slow fronts are still debated.

A better understanding of slow fronts appears as a significant step toward an improved assessment of how frictional motion begins. It is also expected to shed light on the important topic of slow earthquakes, which have been increasingly reported in the last decade (1). In this context, an intense theoretical and numerical activity arose to investigate the origins and properties of rupture fronts. Two different approaches have been explored.

On the one hand, 2D or 3D elastodynamic models have been used to relate the macroscopic loading conditions to the stress field along the contact interface (9–13). These local stresses were indeed shown experimentally to play a role in the selection of the front type (6). However, the models were based on simple friction laws, e.g., Coulomb friction (11) or velocity-weakening friction (12, 13) and did not exhibit slow fronts. On the other hand, fronts much slower than the speed of sound were produced by 1D friction models using improved local friction laws involving an intrinsic time-scale: either (*i*) an aging scale related to the long-time strengthening of an interface at rest (14, 15) as is classically considered in rate-and-state theories (16, 17), or (*ii*) a dynamic scale related to the short-time collective dynamics of formation and rupture of a statistical number of microjunctions during the rupture of the interface (18, 19). Time scales *i* and *ii* were shown, in the same experiment (20), to control the recovery of contact area after slip arrest and the transition between a fast and a slow regime for the slip motion triggered by the front passage, respectively. However, because 1D models are unable to reproduce realistic stress distributions at the interface, they do not allow for quantitative comparison with experiments. Here we combine both 2D elastodynamics and time-dependent friction into a multiscale model for rupture fronts. We demonstrate that the model simultaneously reproduces two separate, unexplained experimental observations: the transition between fast and slow front propagation during a single rupture event, and the transition from fast to slow slip motion at the interface shortly after rupture. In addition, through a more general study of the model, we show that slow slip occurring immediately after a fast front's arrest is a sufficient phenomenon for the front to propagate further as a slow front, and we identify parameters involved in front type selection.

Model Description

The frictional stability of a system made of two solids in contact depends on the level of normal and shear stresses at the contact interface. These interfacial stresses result from the external

Significance

Relative motion between solids in frictional contact is known to start progressively, with a slipping zone growing along the interface. The propagation of the front separating the stuck and slipping zones is usually very fast, but it can also slow down considerably. This transition is not yet understood. Using a multiscale model, we demonstrate how the transition to slow fronts is the direct consequence of slow slip motion at the interface, and that slow fronts are qualitatively different from faster fronts. Because the transition to slow fronts is enabled by slow slip, we expect that it can occur in the wide range of systems in which slow slip has been reported, from engineering to seismology.

Author contributions: J.K.T., H.A.S., J.S., and A.M.-S. designed research; J.K.T., H.A.S., and K.T. performed research; J.K.T., H.A.S., J.S., K.T., D.S.A., and A.M.-S. analyzed data; and J.K.T., J.S., and A.M.-S. wrote the paper.

The authors declare no conflict of interest.

This article is a PNAS Direct Submission. J.F. is a guest editor invited by the Editorial Board.

[1]To whom correspondence may be addressed. E-mail: julien.scheibert@ec-lyon.fr or malthe@fys.uio.no.

This article contains supporting information online at www.pnas.org/lookup/suppl/doi:10.1073/pnas.1321752111/-/DCSupplemental.

forces applied at the boundaries of the solids, transmitted through the bulk. Slip motion will in general be triggered when the local interfacial shear stress reaches a threshold, the level of which crucially depends on the interface behavior law at the microscale.

The net contact between two solids generically consists of a large number of stress-bearing microjunctions whose nature depends on the type of interface. For rough solids, each microjunction corresponds to a microcontact between antagonist asperities, whereas for smoother surfaces the junctions can be solidified patches of an adsorbate layer (21). The three physical aspects of the junction behavior that we consider to be essential are as follows. (*i*) A microjunction in its pinned state can bear a shear force f_T, provided it remains smaller than a threshold f_{thres}. When f_{thres} is reached, a local fracture-like event occurs, and the junction enters a slipping state. (*ii*) In the slipping state, the microjunction can let the interface slip, either through the microslipping of microasperities in contact or through the fluidization of an adsorbate layer. During slip, the microjunction sustains some residual force $f_T = f_{\text{slip}}$, with f_{slip} smaller than f_{thres}. (*iii*) Slipping microjunctions have a certain probability to disappear or relax. For example, a microcontact disappears when an asperity moves away from its antagonist asperity by a typical distance equal to the mean size of microcontacts, as classically considered for slow frictional sliding, e.g., in rate-and-state friction laws. However, another picture may arise as a consequence of the sudden release of energy when pinned junctions break. This energy will transiently heat the region around the microjunction (20). The rise in temperature will significantly increase the rate of a thermally activated relaxation of the slipping microjunction during the time necessary for the interface to cool down (21). The frictional consequences of such temperature rises have recently received renewed attention (e.g., ref. 22), but remain poorly understood. In an attempt to include such thermal processes in our model, we recognize that they will lead to time- rather than distance-controlled relaxations, so that the shear force drop will be distributed in time. In order for the interface to continue bearing the normal forces applied to it, the microjunctions that relax are replaced by new, pinned junctions bearing a small tangential force f_{new}.

The physical aspects described above have been modeled in a simple way using the following assumptions (*Methods*). We consider the rough frictional interface between a rigid track and a thin linear elastic slider of length L and height H (Fig. 1*A*). The bulk elastodynamics of the slider are solved using a square lattice of blocks connected by internal springs (11, 23) (Fig. 1*B*). The multicontact nature of the interface is modeled through an array of N_s tangential springs representing individual microjunctions, attached in parallel to each interfacial block (Fig. 1*C*) (18, 19, 21). The individual spring behavior is as follows (Fig. 1*F*) (24). A spring pinned to the track stretches linearly elastically as the block moves, acting with a tangential force f_T on the block. When the force reaches the static friction threshold f_{thres} (we neglect aging, so that f_{thres} is time independent), the microjunction ruptures and the spring becomes a slipping spring acting with a dynamic friction force $f_T = f_{\text{slip}}$. [f_{thres} and f_{slip} are taken proportional to the normal force p on the corresponding block (*Methods*). This assumption ascribes the pressure dependence of the forces on a block to the individual forces bore by a constant number N_s of springs, rather than to a pressure dependent number of springs per block.] After a random time t_R drawn from a distribution $T(t_R)$, the slipping spring relaxes. It is replaced immediately by a pinned, unloaded spring ($f_{\text{new}} = 0$) and a new cycle starts. Here we use $T(t_R)$ as a simplified way of modeling the distribution of times after which microjunctions relax. Due to the variety and the complexity of the underlying thermal processes, we did not try to derive $T(t_R)$ for a specific situation. Rather, we chose to model $T(t_R)$ in the simplest way, as a Gaussian with average time $\langle t_R \rangle$ and width δt_R. The shape of

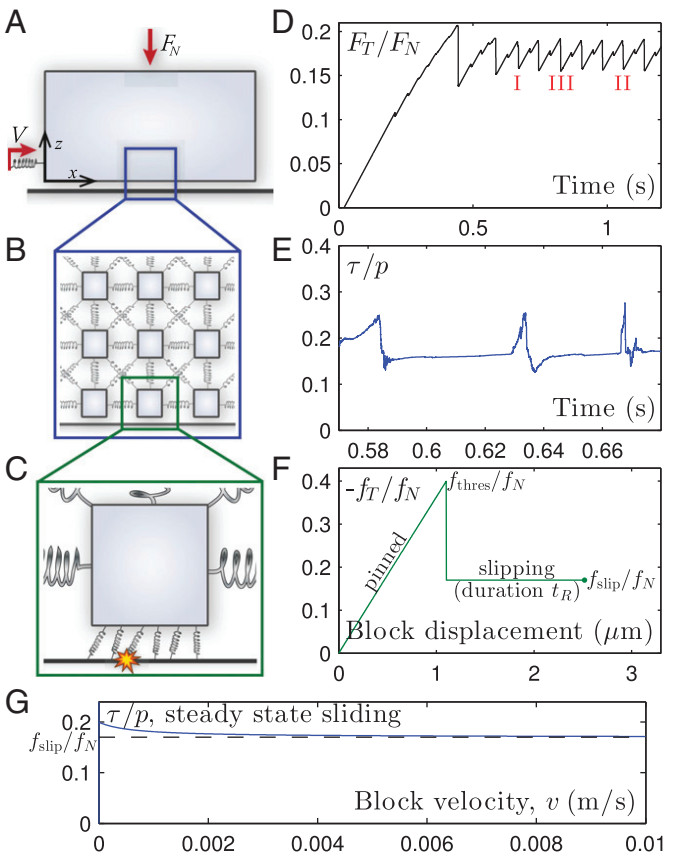

Fig. 1. Sketch and behavior of the multiscale model. (*A*) Slider and external loading conditions. (*B*) Spring-block network modeling elastodynamics. (*C*) Surface springs modeling friction on a block. (*D*) Macroscopic loading curve, the ratio F_T/F_N of driving shear force to total normal force. (*E*) Mesoscopic loading curve, the ratio τ/p of shear to normal stress on a block. (*F*) Microscopic friction model for the spring loading curve, the ratio f_T/f_N of friction to normal force for one spring ($f_N = p/N_s$). (*G*) Steady-state friction force on a block vs. sliding velocity.

$T(t_R)$ is not crucial: We obtain qualitatively similar results with an exponential distribution. The width of $T(t_R)$ is the only source of randomness in our model and causes the interface springs of a block to evolve differently from each other.

The Model Reproduces Rupture Front Observations

In this section we use the model to reproduce unexplained experimental observations made in polymethylmethacrylate by Fineberg and coworkers (4, 20). We use the loading conditions and material constants of ref. 4, as done in ref. 11. We then select the parameters of the friction law to reproduce both the complex space–time evolution of the front velocity reported in ref. 4 and the time-dependent interfacial slip history reported in ref. 20.

The slider is first submitted to normal load F_N only. Then, a slowly increasing tangential load F_T is applied on its left side, at height h above the interface (*SI Methods*). Macroscopically (Fig. 1*D*), the slider is first loaded elastically, yielding high shear stresses in the vicinity of the loading point. These growing stresses eventually trigger the slip of a first block, the motion of which increases the force on its neighbors (Fig. 1*E*) until they also start to slip, and so on. This mechanism results in the propagation of a rupture front across the interface. The first such events arrest before reaching the interface's leading edge and correspond to so-called precursors to sliding (11, 25–28). In the following, we will only consider interface-spanning events (Fig. 2) that are responsible for the large force drops in Fig. 1*D*. We

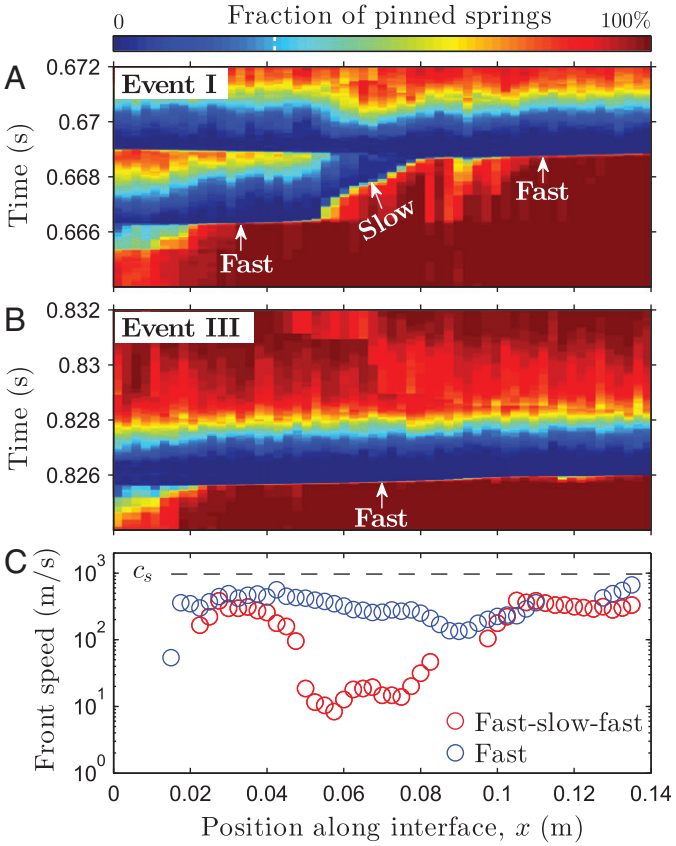

Fig. 2. Two interface-sized events. (*A*) A fast–slow–fast event (I in Fig. 1*D*). Spatiotemporal plot of the fraction of pinned springs. (*B*) A fast-only event (III in Fig. 1*D*) shown as in *A*. (*C*) Rupture front speed v_c vs. front location for both events. Block rupture is defined to occur when 70% of interface springs have broken (white dashed line in the colorbar). Front speed is measured as the inverse slope of the rupture line (indicated by arrows in *A* and *B*) using the endpoints in a five-point-wide moving stencil.

measure the front propagation speed v_c as a function of position x along the interface (Fig. 2*C*) by defining rupture at the block scale when the fraction of pinned springs drops below a threshold value (Fig. 2 *A* and *B*).

Fig. 2*A* shows an event starting as a fast front ($v_c \approx c_s/3$), then turning into a slow front ($v_c \approx c_s/100$) at $x \approx 0.4L$, before turning back into a fast front at $x \approx 0.6L$. This space–time development is in excellent agreement with the experiments from which the model parameters were taken (4). In particular, the locations of the transitions between fast and slow fronts, the duration of the slow front (~1 ms), and the velocity ratio between fast and slow fronts are all matching the experimental observations. Other events are fast across the whole interface (Fig. 2*B*). We emphasize that such spatially heterogeneous dynamics arise spontaneously in our model. This success is presumably due to the two-dimensionality of the model, which allows it to reproduce interfacial stress heterogeneities arising from macroscopic sample geometry and external loading (11) (Fig. S1).

Fig. 3*C* shows the slip experienced by an interfacial block during an event, the time-evolution of which exhibits two distinct regimes. A fast slip regime is followed by a roughly linear slow slip regime, in good agreement with the slip history reported in ref. 20. Notably, both the ratios of slip distances and of slip velocities experienced in either regime are matching the experimental observations.

The simultaneous agreement found with two independent measurements—reproducing the fronts' spatiotemporal dynamics at the slider scale and the slip dynamics at the block scale—indicates that our model can provide insight into the set of experiments reported by Fineberg and coworkers (4, 6, 20, 25). Because the basic ingredients of the model represent general features of frictional interfaces, we expect the model to be applicable to a larger class of systems.

Relationship Between Slow Slip and the Transition to Slow Fronts in the Model

From this section forward we change the scope from reproducing particular experiments to performing a systematic study of the model. We begin by varying select model parameters to unravel the mechanisms underlying slow fronts.

Fig. 3*C* (reference curve) shows the slip history of a block during an event with a slow front (Fig. 3*A*); it has both fast and slow slip regimes. Fast slip initiates with the passage of the rupture front and is independent of $\langle t_R \rangle$ (the three curves in Fig. 3*C* overlap during fast slip). It is followed by a short period of arrest. Then, slow slip originates from the following mechanism: For each spring leaving the slipping state after t_R the friction force on the block is

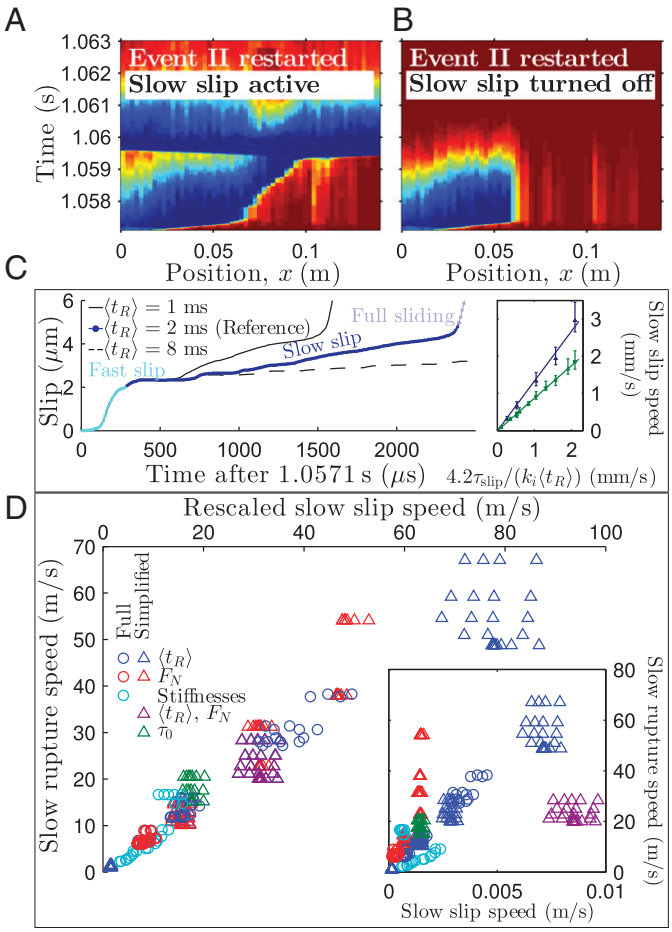

Fig. 3. Slow rupture is governed by slow slip. (*A* and *B*) Event II restarted at 1.0571 s with driving speed $V = 0$, shown as in Fig. 2*A*. Slow slip is either active (*A*) or turned off (*B*). (*C*) Slip profiles for block at $x = 0.34L$ under varying $\langle t_R \rangle$ (*A* uses the reference $\langle t_R \rangle$). The fast slip part is not affected. (*Inset*) Measured slow slip speed $v_{\text{slow slip}}$ matches $v_{\text{slow slip, estimate}} = 4.2\tau_{\text{slip}}/k_i\langle t_R \rangle$ (*SI Equations*). Blue represents data from full simulation and green the data for prepared homogeneous interfaces. k_i is the block–interface stiffness, $\tau_{\text{slip}} = N_s f_{\text{slip}}$. Error bars represent minimum and maximum values. Markers represent the mean (*SI Equations*). The line represents linear fit to mean values, through origin. (*D*) Data collapse of slow rupture speed vs. $v_{\text{slow slip}} k_i l_0/(\tau_{\text{thres}} - \tau_0)$ along prepared homogeneous interfaces, for full and simplified models, and for wide variations in input parameters (see key within the graph). l_0 is a characteristic length (*SI Equations*), $\tau_{\text{thres}} = N_s f_{\text{thres}}$. (*Inset*) Unscaled data.

reduced. As a result the block moves a small distance, driven by the forces from the neighboring blocks. Slow slip results from the succession of such incremental block movements. A scaling analysis of this mechanism (*SI Equations*) yields a prediction for the slow slip velocity $v_{\text{slow slip}}$, which quantitatively captures the data (Fig. 3*C*, *Inset*).

The fast–slow–fast front in Fig. 3*A* becomes an arrested front in Fig. 3*B* when we restart the simulation in the same state, but with slow slip turned off. We do this by setting $f_{\text{new}} = f_{\text{slip}}$ so that springs leaving the slipping state no longer relax, but return to the pinned state bearing the same force as during slip. The front in Fig. 3*B* arrests where the fast-to-slow transition used to take place. These results support the following scenario: Slow fronts are fronts that would arrest in the absence of slow slip, but are pushed further by the increasing loading due to slow slip behind the front tip.

To show that slow slip occurring immediately after front arrest is a sufficient condition for the transitions to slow fronts to be allowed, we consider the following simplified model. We leave microscale dynamics out by replacing the ensemble of springs connecting each block to the track with a single spring: The spring breaks when reaching the force $N_s f_{\text{thres}}$, it slides with a force $N_s f_{\text{slip}}$, and it returns to the pinned state still bearing the force $N_s f_{\text{slip}}$ when the block velocity vanishes. Slow slip is introduced directly as a small velocity applied to the spring attachment point (*SI Methods*). The transition from fast to slow fronts is indeed observed in this simplified model (Fig. S2), and disappears if slow slip is turned off.

To characterize the relationship between slow slip velocity and slow front velocity, we consider both the complete and simplified models and use interfaces prepared as follows (*SI Methods*). We choose the normal force $p(x)$ on each block from the substrate to be uniform in space and constant in time, and the shear force profile $\tau(x)$ to have initial values $\tau_0(x)$ uniform in space except in a region used to initiate front propagation (Fig. S3). We vary different model parameters, keeping the front initiation region unchanged, and systematically measure the slow front velocity $v_{c,\text{ slow}}$ as a function of $v_{\text{slow slip}}$ (Fig. 3*D*, *Inset*). Suitable rescaling (*SI Equations*) of $v_{\text{slow slip}}$ allows all points to collapse on a single straight line (Fig. 3*D*). This collapse shows that $v_{c,\text{ slow}}$ is proportional to $v_{\text{slow slip}}$, with the same conversion factor for both models. We conclude that even though $v_{\text{slow slip}}$ depends on the interfacial dynamics, the conversion factor does not; it mainly depends on the way stresses are transferred from the slowly slipping region to the rupture tip. Similar linear relationships between slip and front velocities were found in previous models (14, 15, 29).

Selection of the Front Type in the Model

We now turn to the question of front type selection. Ben-David et al. (6) showed that slow (fast) fronts correlate locally with small (high) shear to normal stress ratio $\tau_0(x)/p(x)$ just before the event. In equilibrium, τ is the sum of the spring forces f_T for each block. Due to the randomness in the slip times t_R, the individual f_T will be different. As in previous works (21, 24, 30), it is useful to define a distribution ϕ (f_T) of the forces in the springs attached to each block. ϕ is a dynamical quantity evolving with both the loading on and the motion of blocks. Note that in general ϕ will be different for every block.

We find that the width σ of the distribution ϕ is as important as the stress ratio for front type selection. To demonstrate this we take event II as a reference and modify it by changing σ for all blocks at $x > 0.25L$. To isolate the effect of σ from the effect of the stress ratio on front propagation, we increase σ but keep $\tau_0(x)$ unchanged. We do this by making each block's $\phi(f_T)$ a uniform distribution while keeping its average unchanged (Fig. S4). We then restart the simulation and observe that the front has changed from a fast–slow–fast one (Fig. 4*A*) to a fast one across the whole interface (Fig. 4*B*). The reason for this behavior is that increasing σ from Fig. 4*A* to Fig. 4*B* weakens the interface, which enables the fast rupture to reach the leading edge without stopping and becoming a slow front. The weakening can be understood from Fig. 4*C*, which shows the effective static friction coefficient $\mu_s^{\text{eff}} = \tau_{\max}/p$ of an interface block, with $\tau_{\max}$ the maximum friction force on the block before it starts to slip. Small (large) σ correspond to large (small) $\tau_{\max}$ (Fig. S5), i.e., a locally stronger (weaker) interface, consistent with the fact that points corresponding to slow fronts cluster at low σ in Fig. 4*C*.

Fig. 4 *A* and *B* indicates that, besides τ_0/p, σ is involved in front type selection. Using interfaces prepared as in Fig. 3*D*, we systematically vary the values of τ_0 and σ and observe which front type is selected (Fig. 4*D*). The effect of τ_0 agrees with experiments (6), but is modulated by the effect of σ. Low τ_0 and σ lead to fronts that arrest before spanning the whole interface. Large τ_0 and σ yield fast fronts. Global events containing a slow part are found in a region of intermediate τ_0 and σ. These results are found qualitatively robust not only against changes in sample geometry or energy stored in the nucleation region, but also against changes in the individual behavior of the interfacial springs (Fig. S6). We therefore expect the main features of Fig. 4*D* to be widely relevant.

Discussion

The present model differs from classical rate-and-state friction laws (16, 17), which are empirical laws based on experimental results obtained for small sliding velocities ($\lesssim 100$ μm/s), for which self-heating of the interface is negligible. In rate-and-state models the relevant timescale is that of aging, i.e., the slow (logarithmic) recovery of contact area at rest. The relevant slip distance is the average microcontact size, after which all junctions are renewed. Here, we focus on a different friction regime, with a microsecond-long fracture process, followed by large slip velocities in the fast slip regime (~100 mm/s in ref. 20), both

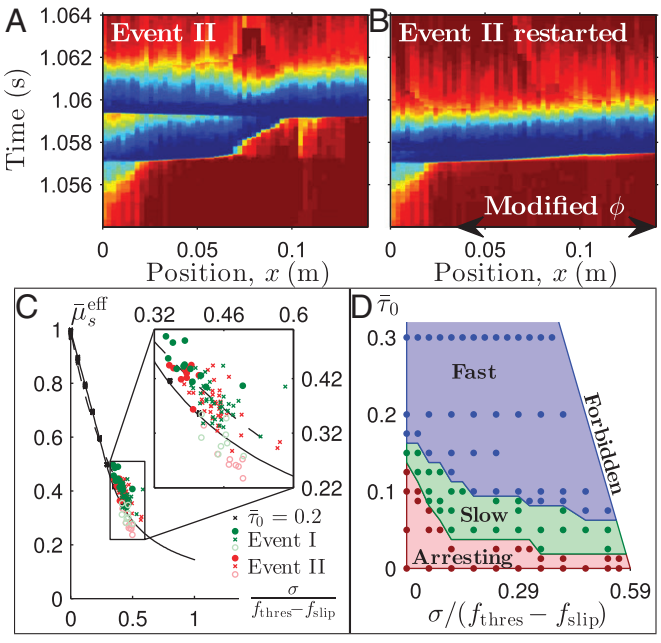

Fig. 4. Role of microscopic force distributions in rupture dynamics. (*A*) Event II shown as in Fig. 2*A*. (*B*) Event II restarted at 1.054 s with wider $\phi(f_T)$ in the region $x > 0.25L$ (arrow) results in a fast-only event. (*C*) $\bar{\mu}_s^{\text{eff}} = ((\tau_{\max}/p) - (f_{\text{slip}}/f_N))/((f_{\text{thres}}/f_N) - (f_{\text{slip}}/f_N))$ vs. $\tilde{\sigma} = \sigma/(f_{\text{thres}} - f_{\text{slip}})$ for all blocks in events I (green) and II (red), and for prepared events (black) with homogeneous $\bar{\tau}_0 = ((\tau_0/p) - (f_{\text{slip}}/f_N))/((f_{\text{thres}}/f_N) - (f_{\text{slip}}/f_N))$. ●, slow front; ×, fast front; ○, loading zone ($x < 2$ cm). Solid (dashed) line is for uniform (bell-shaped) $\phi(f_T)$ (Fig. S4). (*D*) Observed front type for prepared interfaces vs. both $\bar{\tau}_0$ and $\tilde{\sigma}$. Dots represents data points.

phenomena contributing to a significant temperature increase at the interface. Our model thus considers the relevant timescale t_R to be the one of thermally activated relaxations during the period needed for the interface to slowly slip and stop (we neglect aging). The corresponding slip distance is the one allowed by junction relaxations during the same period.

In the context of rate-and-state friction, it was recently suggested that slow slip velocity corresponds to the sliding speed at which the interface's steady-state friction laws reaches a minimum (14, 15, 31). In our model, however, slow slip has a completely different origin, related to the intrinsic relaxation dynamics of the interface after a fast slip period (Fig. 3*C* and *SI Equations*). As a matter of fact, the steady-state friction law that emerges from the microjunction dynamics at the block scale is purely monotonic and decreasing (Fig. 1*G*) (24). To what extent the slow fronts related to both types of slow slip share similar properties remains to be investigated.

Up to now, the term slow front has been used in the literature to name any front propagating at least 1 order of magnitude slower than the material's wave speeds. Our results allow for a tentative definition of the slow fronts first observed in ref. 4. They are fronts that would arrest in the absence of slow slip, but are pushed further by the increasing loading due to slow slip behind the front tip. Importantly, the motion results from the intrinsic relaxation dynamics of the interface and not from an external driving. A direct consequence is shown in Fig. 5*A*, where the increase in tangential load is stopped during the propagation of the slow front of Fig. 2. We observe that the slow front is not affected and propagates exactly like in the original event, which indicates that the front is truly dynamic. This contrasts with the behavior of the event shown in Fig. 5*B*, where the loading is applied to the bottom left-most block. Extremely slow fronts are then observed, similar to the ones reported in, e.g., refs. 15, 18, 19, and 32, which propagate over the timescale of the interval between two dynamic events. These fronts stop when the driving stops, indicating that they are of a different, quasistatic nature.

This distinction sheds light on the difference between our model and recent models for the onset of sliding of extended interfaces. Urbakh and coworkers (18, 19) have used 1D spring-block models with an interfacial behavior also based on microjunctions having two possible states. However, they used $f_{\text{slip}} = 0$, which prevented slow slip to occur. As a consequence, they observed fast and quasistatic fronts, but did not observe dynamic slow fronts like those reported here. Bouchbinder and coworkers (14, 15, 32) have developed an improved rate-and-state law and used it in 1D. They consider the classical aging timescale whereas we consider a dynamic healing timescale relevant during the short-lived rupture-induced temperature rise of the interface. They observed the transition from quasistatic to fast dynamic rupture, but no fast-to-slow dynamic front transition. Other works considered 2D models, but with velocity-weakening local friction laws (12, 13). Although they observed fast and quasistatic fronts, they did not report any transition from fast to slow dynamic fronts.

Our results make a direct bridge between the separate observations of a transition from fast to slow fronts and of slow slip in recent experiments (4, 20). As slow slip was observed in many systems from geoscience (1, 33, 34) to materials science (20, 35), we expect the transition to slow fronts to be possible in these systems, too. The physical process underlying slow slip, e.g., thermal softening in glassy polymers (20), thermal creep in paper (35), and dilatant strengthening in subduction zones (36) differs from system to system (22). The present model does not aim at modeling one particular process. Rather, through the time distribution $T(t_R)$, we introduce the minimal generic ingredient necessary to yield a slow interfacial slip motion.

Using the simplified model, we demonstrated that slow fronts can in principle exist even if only one microjunction is kept per block, i.e., the force distribution ϕ has width $\sigma = 0$, provided slow slip is introduced in another way. However, we believe that virtually all frictional interfaces are of the multijunction type at the relevant scale, e.g., microcontact or molecular scale. Due to random physical properties or stochastic pinning/relaxation events combined with the previous sliding dynamics, there will always be some disorder in the forces bore by the junctions, as recognized in various friction models (e.g., refs. 18, 21, 24, and 30). The disorder was shown to control, e.g., the steady sliding friction force and the transition between smooth sliding and stick–slip regimes (30). Here we showed that the force distribution is also a key parameter in front type selection. It appears as a state parameter that, by controlling the effective friction threshold μ_s^{eff} at the block scale (24), is able to affect interfacial rupture in a way analogous to but different from the usual age state used in rate-and-state friction laws.

We believe that all our results are relevant to a large class of systems with a random population of stress-bearing entities having both a threshold-like rupture behavior and a time-dependent healing process, such as nanoscience (37), polymer science (38), and seismology (39).

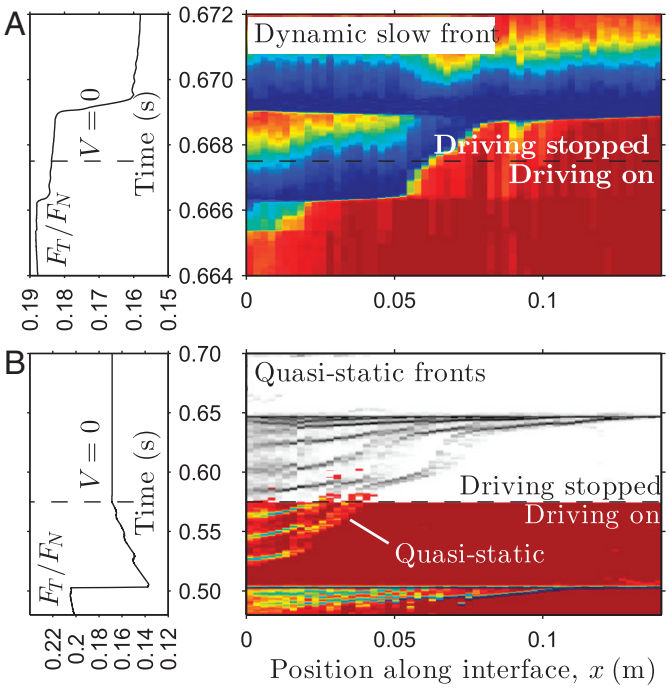

Fig. 5. Dynamic vs. quasistatic slow fronts. (*Upper* and *Lower Left*) Macroscopic loading curves. (*Upper* and *Lower Right*) Fraction of pinned springs shown as in Fig. 2*A*. (*A*) Event I restarted. (*B*) Data from a simulation where driving is applied at $h = 0$. Gray scale represents the original data with no change to V. Color represents the data in which the driving speed is set to $V = 0$ during front propagation. After setting $V = 0$, we only show color when at least 5% of a block's springs are slipping.

Methods

Parameters are in Table S1. Spring j of block i has strength $f_{\text{thres}} = \mu_s p_i / N_s$ and stiffness $k_{ij} \propto \sqrt{p_i / N_s}$. The force on block i from spring j is $f_{Tij} = k_{ij}(x_{ij} - x_i)$, where x_{ij} is the attachment point of the spring to the track and x_i is the block's position. While slipping, the spring trails the block with x_{ij} adjusted in every time step to ensure $|f_{Tij}| = f_{\text{slip}} = \mu_d p_i / N_s$. Note that if the block motion reverses, x_{ij} stops changing and remains fixed while $|f_{Tij}| \leq f_{\text{slip}}$. The probability distribution $T(t_R)$ is based on a Gaussian $T_G(t_R) = (1/(\sqrt{2\pi}\delta t_R))$ $\exp(-(t_R - \bar{t}_R)^2/(2\delta t_R^2))$, modified so that negative lifetimes are forbidden: $T(t_R) = T_G(t_R) + T_G(-t_R), t_R \in [0,\infty]$. With the parameter values we use, $\langle t_R \rangle \cong \bar{t}_R$. In the simulations behind Fig. 3 *C* and *D*, the ratio $\delta t_R / \bar{t}_R$ is maintained. Details on initialization and nonfrictional boundary conditions are in *SI Methods*. The motion is found using a velocity Verlet scheme with $\Delta t = 2 \times 10^{-7}$ s.

ACKNOWLEDGMENTS. We thank C. Caroli and G. Debrégeas for their comments on an early version of the manuscript and D. Bonamy, A. Le Bot, and S. Nielsen for their comments. This work was supported by a Center of Excellence grant to Physics of Geological Processes from the Norwegian Research Council. This work was supported by the bilateral researcher exchange program Aurora (Hubert Curien Partnership), financed by the Norwegian Research Council and the French Ministry of Foreign Affairs and International Development (Grant 27436PM, 213213). J.S. acknowledges support from the People Programme (Marie Curie Actions) of the European Union's 7th Framework Programme (FP7/2007-2013) under Research Executive Agency Grant Agreement 303871. K.T. acknowledges support from VISTA, a basic research program funded by Statoil, conducted in close collaboration with The Norwegian Academy of Science and Letters.

1. Peng Z, Gomberg J (2010) An integrated perspective of the continuum between earthquakes and slow-slip phenomena. *Nat Geosci* 3(9):599–607.
2. Johnson KL (1985) *Contact Mechanics* (Cambridge Univ Press, Cambridge, UK).
3. Prevost A, Scheibert J, Debrégeas G (2013) Probing the micromechanics of a multicontact interface at the onset of frictional sliding. *Eur Phys J E Soft Matter* 36(2):17.
4. Rubinstein SM, Cohen G, Fineberg J (2004) Detachment fronts and the onset of dynamic friction. *Nature* 430(7003):1005–1009.
5. Xia K, Rosakis AJ, Kanamori H (2004) Laboratory earthquakes: The sub-Rayleigh-to-supershear rupture transition. *Science* 303(5665):1859–1861.
6. Ben-David O, Cohen G, Fineberg J (2010) The dynamics of the onset of frictional slip. *Science* 330(6001):211–214.
7. Nielsen S, Taddeucci J, Vinciguerra S (2010) Experimental observation of stick-slip instability fronts. *Geophys J Int* 180(2):697–702.
8. Audry MC, Fretigny C, Chateauminois A, Teissere J, Barthel E (2012) Slip dynamics at a patterned rubber/glass interface during stick-slip motions. *Eur Phys J E Soft Matter* 35(9):83.
9. Ben-Zion Y (2001) Dynamic ruptures in recent models of earthquake faults. *J Mech Phys Solids* 49:2209–2244.
10. Di Bartolomeo M, Meziane A, Massi F, Baillet L, Fregolent A (2010) Dynamic rupture at a frictional interface between dissimilar materials with asperities. *Tribol Int* 43(9): 1620–1630.
11. Trømborg J, Scheibert J, Amundsen DS, Thøgersen K, Malthe-Sørenssen A (2011) Transition from static to kinetic friction: Insights from a 2D model. *Phys Rev Lett* 107(7):074301.
12. Kammer DS, Yastrebov VA, Spijker P, Molinari J-F (2012) On the propagation of slip fronts at frictional interfaces. *Tribol Lett* 48(1):27–32.
13. Otsuki M, Matsukawa H (2013) Systematic breakdown of Amontons' law of friction for an elastic object locally obeying Amontons' law. *Sci Rep* 3:1586.
14. Bar Sinai Y, Brener EA, Bouchbinder E (2012) Slow rupture of frictional interfaces. *Geophys Res Lett* 39:L03308.
15. Bouchbinder E, Brener EA, Barel I, Urbakh M (2011) Slow cracklike dynamics at the onset of frictional sliding. *Phys Rev Lett* 107(23):235501.
16. Baumberger T, Caroli C (2006) Solid friction from stick-slip down to pinning and aging. *Adv Phys* 55(3-4):279–348.
17. Marone C (1998) Laboratory-derived friction laws and their application to seismic faulting. *Annu Rev Earth Planet Sci* 26:643–696.
18. Braun OM, Barel I, Urbakh M (2009) Dynamics of transition from static to kinetic friction. *Phys Rev Lett* 103(19):194301.
19. Capozza R, Urbakh M (2012) Static friction and the dynamics of interfacial rupture. *Phys Rev B* 86(8):085430.
20. Ben-David O, Rubinstein SM, Fineberg J (2010) Slip-stick and the evolution of frictional strength. *Nature* 463(7277):76–79.
21. Persson BNJ (1995) Theory of friction: Stress domains, relaxation, and creep. *Phys Rev B Condens Matter* 51(19):13568–13585.
22. Di Toro G, et al. (2011) Fault lubrication during earthquakes. *Nature* 471(7339): 494–498.
23. Yim H, Sohn Y (2000) Numerical simulation and visualization of elastic waves using mass-spring lattice model. *IEEE Trans Ultrason Ferroelectr Freq Control* 47(3):549–558.
24. Thøgersen K, Trømborg JK, Sveinsson HA, Malthe-Sørenssen A, Scheibert J (2014) History-dependent friction and slow slip from time-dependent microscopic junction laws studied in a statistical framework. *Phys Rev E Stat Nonlin Soft Matter Phys* 89(5):052401.
25. Rubinstein SM, Cohen G, Fineberg J (2007) Dynamics of precursors to frictional sliding. *Phys Rev Lett* 98(22):226103.
26. Scheibert J, Dysthe DK (2010) Role of friction-induced torque in stick-slip motion. *EPL* 92(5):54001.
27. Maegawa S, Suzuki A, Nakano K (2010) Precursors of global slip in a longitudinal line contact under non-uniform normal loading. *Tribol Lett* 38(3):313–323.
28. Amundsen DS, Scheibert J, Thøgersen K, Trømborg J, Malthe-Sørenssen A (2012) 1D model of precursors to frictional stick-slip motion allowing for robust comparison with experiments. *Tribol Lett* 45(2):357–369.
29. Ohnaka M, Yamashita T (1989) A cohesive zone model for dynamic shear faulting based on experimentally inferred constitutive relation and strong motion source parameters. *J Geophys Res* 94(B4):4089–4104.
30. Braun OM, Peyrard M (2010) Master equation approach to friction at the mesoscale. *Phys Rev E Stat Nonlin Soft Matter Phys* 82(3 Pt 2):036117.
31. Kaproth BM, Marone C (2013) Slow earthquakes, preseismic velocity changes, and the origin of slow frictional stick-slip. *Science* 341(6151):1229–1232.
32. Bar-Sinai Y, Spatschek R, Brener EA, Bouchbinder E (2013) Instabilities at frictional interfaces: Creep patches, nucleation, and rupture fronts. *Phys Rev E Stat Nonlin Soft Matter Phys* 88(6):060403.
33. Hirose H, Obara K (2005) Repeating short-and long-term slow slip events with deep tremor activity around the Bungo channel region, southwest Japan. *Earth Planets Space* 57(10):961–972.
34. Ohnaka M, Kuwahara Y (1990) Characteristic features of local breakdown near a crack-tip in the transition zone from nucleation to unstable rupture during stick-slip shear failure. *Tectonophysics* 175(1-3):197–220.
35. Heslot F, Baumberger T, Perrin B, Caroli B, Caroli C (1994) Creep, stick-slip, and dry-friction dynamics: Experiments and a heuristic model. *Phys Rev E Stat Phys Plasmas Fluids Relat Interdiscip Topics* 49(6):4973–4988.
36. Segall P, Rubin AM, Bradley AM, Rice JR (2010) Dilatant strengthening as a mechanism for slow slip events. *J Geophys Res* 115:B12305.
37. Li Q, Tullis TE, Goldsby D, Carpick RW (2011) Frictional ageing from interfacial bonding and the origins of rate and state friction. *Nature* 480(7376):233–236.
38. Cordier P, Tournilhac F, Soulié-Ziakovic C, Leibler L (2008) Self-healing and thermoreversible rubber from supramolecular assembly. *Nature* 451(7181):977–980.
39. McLaskey GC, Thomas AM, Glaser SD, Nadeau RM (2012) Fault healing promotes high-frequency earthquakes in laboratory experiments and on natural faults. *Nature* 491(7422):101–104.

Supporting Information

Trømborg et al. 10.1073/pnas.1321752111

SI Methods

This section supports the model description found in the main text and *Methods* with detailed information on how we initialize the system and apply the boundary conditions. We also provide some additional information on the simplified model.

The slider is initialized with full normal load F_N and no tangential load F_T by gradually applying F_N without allowing springs to break, a technicality required because the normal forces on the springs, f_{Nij}, start at zero and therefore the springs, if allowed to, would break under any stretching. We distribute the load F_N uniformly on the top blocks; apart from this we use the same nonfrictional boundary conditions as in ref. 1. The unique equilibrium is found through damped relaxation of typical duration 10 ms. After relaxation, we check that no spring is stretched beyond its strength and introduce the driving spring starting from zero applied driving force F_T. Then F_T, which acts on the block on the left side of the slider situated at height h above the interface, through the driving spring, increases as the driving point moves to the right with speed V.

In the simplified model used for Fig. 3*D*, we disregard the microscopic state by using a single friction spring per block. Taking parameters from the microscopic reference model described in the main text (*Model Description*), each block's spring now has a strength $\tau_{\text{thres}} = \mu_s p_i = N_s f_{\text{thres}}$. The stiffness k_i of a block's friction spring equals the combined stiffness of the springs per block in the reference model. The force on block i from its friction spring is $f_{Ti} = k_i(x_{is} - x_i)$, where x_{is} is the attachment point of the spring to the track. Upon breaking, the spring becomes a slipping spring and its behavior starts to differ from that of the springs in the microscopic model. We impose a slow slip by letting x_{is} move with a velocity $v_{\text{slow slip spring}}$ for a time $t_{\text{slow slip spring}} = \bar{t}_R$. This process competes with the dynamic friction law where the spring trails the block with x_{is} adjusted in every time step to ensure $|f_{Ti}| \le \mu_d p_i$, so that the spring attachment point moves with the highest of $v_{\text{slow slip spring}}$ and v_{xi}, the speed of the block in the x direction. When the block motion reverses (v_{xi} changes sign), the spring returns to the pinned state, but x_{is} continues to move at $v_{\text{slow slip spring}}$ until a time $t_{\text{slow slip spring}}$ later than when the spring was broken.

The systematic studies leading to Figs. 3 *C* (*Inset* , green) and *D* and 4*D* were done with different normal forces and different initialization from the other simulations. The normal force boundary conditions on the top and bottom were exchanged: This simplifies the analysis by setting a constant normal force $p_i = F_N/N_x$ on all blocks i at the interface. To maintain stability against global rotation, the top blocks interacted with an elastic ceiling with the same properties as the elastic foundation used in ref. 1 and the other simulations presented here.

To obtain an initial state with a prescribed interfacial shear stress profile we turned the interface springs off during the initialization. In their place we added to each bottom block the force corresponding to the shear stress to be prescribed. We also introduced the driving spring, but let $V = 0$. During relaxation, the sample moved along the x axis until the force in the driving spring balanced the net force from the interfacial shear stress. To get rid of oscillations more efficiently, we added damping forces $-\alpha(\vec{v}_i)$ on the blocks' motion. After relaxation, the extra forces and the extra damping were turned off and the interfacial springs were introduced, with their attachment points x_{ij} chosen such that the net force on each block was unchanged and the desired distribution of spring forces, $\phi(f_T)$, appeared. We then waited a few time steps to ensure that the transition from pre- to postrelaxation involved no force discontinuities. Next, instead of driving the system with $V \neq 0$ until rupture is triggered, we started fronts by simultaneously depinning all springs for all blocks to the left of x_{trigger}. The shear stress in the triggering region has a strong influence on the rupture fronts; to compare results between simulations, we used a constant value $\bar{\tau}_{\text{trigger}}$.

SI Equations

Estimate of $v_{\text{slow slip}}$ from Model Parameters. Here we provide the arguments behind the slow slip speed estimate used in Fig. 3*C*, *Inset*.

The mechanism for slow slip in our model is the force drop when slipping junctions relax and repin at zero force. To determine the slip speed (block motion per unit time) associated with the relaxation of junctions, we identify the net slip caused by this change and the time over which the change happens. To do this, we assume that each time a junction relaxes, the block moves forward just enough to return to the force it was bearing just before relaxation. Thus, the force reduction $-f_{\text{slip}}$ in the junction is matched by an equivalent net force increase in the junctions that are already pinned and in the coupling to the neighboring blocks. The effective stiffness of these interface and bulk terms depends on the fraction of junctions that are pinned and on the motion of the neighboring blocks, respectively.

A careful look at the motion of blocks during their slow slipping regime proved that neighboring blocks move essentially at the same slow slip speed. This means that the force changes on a block due to relative motion with respect to its neighbors remain negligible. We can therefore assume in this calculation that the only contribution to force restoring after junction relaxations is due to the pinned interfacial junctions.

We now assume that all junctions start in the slipping state. After the first junction relaxes and repins, the effective stiffness of the interface is just the stiffness of this single junction, k_{ij}. The force drop $-f_{\text{slip}}$ must be compensated by stretching this (now pinned) junction by moving the block a distance $\delta_1 = f_{\text{slip}}/k_{ij}$. For the second junction the force drop is again $-f_{\text{slip}}$, but the stiffness of the interface has increased to $2k_{ij}$ and the required slip is $\delta_2 = f_{\text{slip}}/(2k_{ij})$. If no junction would reach its breaking threshold f_{thres} during the whole relaxation process, then we would find $x_{\text{slow slip}} = \sum_{j=1}^{N_s} \delta_j = \sum_{j=1}^{N_s} f_{\text{slip}}/(jk_{ij})$. Because the k_{ij} are independent of j, this is just $\delta = f_{\text{slip}}/k_{ij} \sum_{n=1}^{N_s} 1/n$ with n as the dummy index. For $N_s = 100$ used in the model, the sum evaluates to 5.2. However, for $f_{\text{thres}}/f_{\text{slip}} = 40/17$ used in the model, some junctions do break again before all slipping junctions relax. The force drop associated with the transition from pinned to slipping state is $f_{\text{slip}} - f_{\text{thres}}$, and acts in the same way as the force drop when junctions leave the slipping state. Taking this into account and evaluating the return to the pinned state more carefully, we find the net block slip to be $8.5 f_{\text{slip}}/k_{ij}$.

With the slipping time standard deviation $\delta t_R = 0.3\bar{t}_R$ used in the model, the time for all of the junctions to return to the pinned state is found to be close to $2\langle t_R \rangle$.

Combining these slip distance and slip time values, and defining $\tau_{\text{slip}} = N_s f_{\text{slip}}$ and $k_i = N_s k_{ij}$, we use

$$v_{\text{slow slip, estimate}} = 4.2 \frac{\tau_{\text{slip}}}{k_i \langle t_R \rangle}. \qquad \text{[S1]}$$

Fig. 3*C*, *Inset* plots the slow slip speed measured in the simulations against this estimate. The markers indicate when we have varied τ_{slip} (■), k_i (◀), and $\langle t_R \rangle$ (▲). "●" uses our reference parameters. The blue data are based on restarting event II. Because

τ_{slip} and k_i enter in the elastic state of the slider, only $\langle t_R \rangle$ could be varied for these simulations. The green data are for prepared homogeneous interfaces, where parameters can be varied freely. (When f_{slip} is varied, f_{thres} is varied proportionally to keep the fast–slow–fast nature of the rupture front. For the same reason, when k_i is varied, the prestress in the triggering region is also varied slightly.)

When slow slip speed is measured in the simulations based on event II (blue data in Fig. 3*C*, *Inset*), some deviation from $v_{\text{slow slip, estimate}}$ is observed. There are several possible reasons for such a deviation. First, the assumption of comoving neighbors is only approximately correct (near the front tip, the neighbors to the right are stuck until the rupture front passes them). The actual motion of the neighbors also depends on the stress state and the triggering of the event. Second, the assumption of force rebalancing every time a junction changes state is probably too strong.

Scaling of $v_{c,\text{ slow}}$ with $v_{\text{slow slip}}$. The data collapse in Fig. 3*D* is obtained by plotting the slow rupture speed $v_{c,\text{ slow}}$ against the quantity $v_{\text{slow slip}} k_i l_0/(\tau_{\text{thres}} - \tau^0)$, where $v_{\text{slow slip}}$ is the slow slip speed, k_i is the stiffness of the connection between a block and the interface (a single spring in the simplified model and a parallel connection in the reference microscopic model), l_0 is a characteristic length, $\tau_{\text{thres}} = N_s f_{\text{thres}}$ is the maximum shear strength of a block, and τ^0 is the shear force in the propagation region before the event is started. In this section we provide a crude argument for this scaling.

When a region of initially homogeneous prestress is being stressed further by block motion on the left, the decaying shear force profile can be written on the form

$$\tau(x) = Af\left(\frac{x - x_0}{l_0}\right) + \tau^0, \qquad \textbf{[S2]}$$

where A is an amplitude and $f()$ is a function that has magnitude 1 at $x = x_0$ and decays over a characteristic length l_0 that depends on the bulk to interfacial stiffness ratio k/k_i. The function $f()$ is known in 1D (equation 46 in ref. 2). In 2D it can be measured in an elastostatic model, but its exact form is not required for the present argument.

In a static situation, $\tau(x)$ is balanced by the friction forces in the interfacial springs. Ignoring the width of the spring force distribution, the block at x_0 is at its static friction threshold when the force on it from its neighboring blocks is $\tau(x_0) = \tau_{\text{thres}}$, which gives $A = (\tau_{\text{thres}} - \tau^0)$. The next block to the right, at position $x = x_0 + \mathrm{d}x$, then has

$$\tau(x_0 + \mathrm{d}x) = Af[x_0 + \mathrm{d}x] + \tau^0. \qquad \textbf{[S3]}$$

Here we have used the short-hand notation $f[x] = f((x - x_0)/l_0)$.

As the front tip moves from the block at x_0 to the block at $x_0 + \mathrm{d}x$, the force on this block from its neighbors increases to $\tau'(x_0 + \mathrm{d}x) = \tau_{\text{thres}}$. It will be useful to rewrite this as $\tau'(x_0 + \mathrm{d}x) = \tau_{\text{thres}} = \tau(x_0) = Af[x_0] + \tau^0$. The change in force on the block at $x_0 + \mathrm{d}x$ is

$$\Delta\tau(x_0 + \mathrm{d}x) = \tau'(x_0 + \mathrm{d}x) - \tau(x_0 + \mathrm{d}x) \qquad \textbf{[S4]}$$

$$= A(f[x_0] - f[x_0 + \mathrm{d}x]). \qquad \textbf{[S5]}$$

Assuming the change in force from the block's neighbors is balanced by an equal change in the friction force on the block allows us to relate the force change to a displacement of the block, namely

$$\Delta u(x_0 + \mathrm{d}x) = \frac{\Delta\tau(x_0 + \mathrm{d}x)}{k_i}. \qquad \textbf{[S6]}$$

In the next step we will need the displacement of the block at x_0 during the same time interval. As the blocks are at closely spaced points in a deforming elastic medium we will assume $\Delta u(x_0) = \Delta u(x_0 + \mathrm{d}x)(1 + O(\mathrm{d}x)) \approx \Delta u(x_0 + \mathrm{d}x)$.

Now we make the approximation that after breaking, the blocks move at a constant speed $v_{\text{slow slip}}$. It follows that the time it takes from when the block at x_0 breaks and until when the block at $x_0 + \mathrm{d}x$ breaks is

$$\mathrm{d}t = \frac{\Delta u(x_0)}{v_{\text{slow slip}}}. \qquad \textbf{[S7]}$$

During this time the front tip has moved the distance dx from one block to the next, and the front speed is

$$v_{c,\text{ slow}} = \frac{\mathrm{d}x}{\mathrm{d}t} = v_{\text{slow slip}} \frac{\mathrm{d}x}{\Delta u(x_0)} \qquad \textbf{[S8]}$$

$$= v_{\text{slow slip}} \frac{k_i}{\tau_{\text{thres}} - \tau^0} \frac{dx}{f[x_0] - f[x_0 + \mathrm{d}x]}. \qquad \textbf{[S9]}$$

Here we recognize an approximation to the spatial derivative of the unknown function $f()$, evaluated at $x = x_0$. We will use the chain rule to separate the nondimensional and dimensional parts of this derivative, and therefore we define $X(x) = (x - x_0)/l_0$ so that $f[x] = f(X(x))$. With this notation,

$$\frac{\mathrm{d}f}{\mathrm{d}x} = \frac{\mathrm{d}f}{\mathrm{d}X}\frac{\mathrm{d}X}{\mathrm{d}x} = \frac{\mathrm{d}f}{\mathrm{d}X}\frac{1}{l_0}, \qquad \textbf{[S10]}$$

we arrive at

$$v_{c,\text{ slow}} = v_{\text{slow slip}} \frac{k_i}{\tau_{\text{thres}} - \tau^0} \frac{l_0}{\left(-\frac{\mathrm{d}f}{\mathrm{d}X}\right)_{x = x_0}}. \qquad \textbf{[S11]}$$

This argument provides a rationale for the linear relationship observed in Fig. 3*D*, but with the function $f()$ unknown we are not able to predict the value of the coefficient of proportionality. From the shear force profiles we estimate the decay length $l_0 = 7$ mm, a value shared between simulations because we keep k/k_i the same, and rescale $v_{\text{slow slip}}$ with $k_i l_0/(\tau_{\text{thres}} - \tau^0)$. Note that in the model, $\tau_{\text{thres}} = N_s f_{\text{thres}} = \mu_s p$ with μ_s the threshold force coefficient and p the normal force on the block, which means that the normal force enters in the scaling.

1. Trømborg J, Scheibert J, Amundsen DS, Thøgersen K, Malthe-Sørenssen A (2011) Transition from static to kinetic friction: Insights from a 2D model. *Phys Rev Lett* 107(7):074301.

2. Amundsen DS, Scheibert J, Thøgersen K, Trømborg J, Malthe-Sørenssen A (2012) 1D model of precursors to frictional stick-slip motion allowing for robust comparison with experiments. *Tribol Lett* 45(2):357–369.

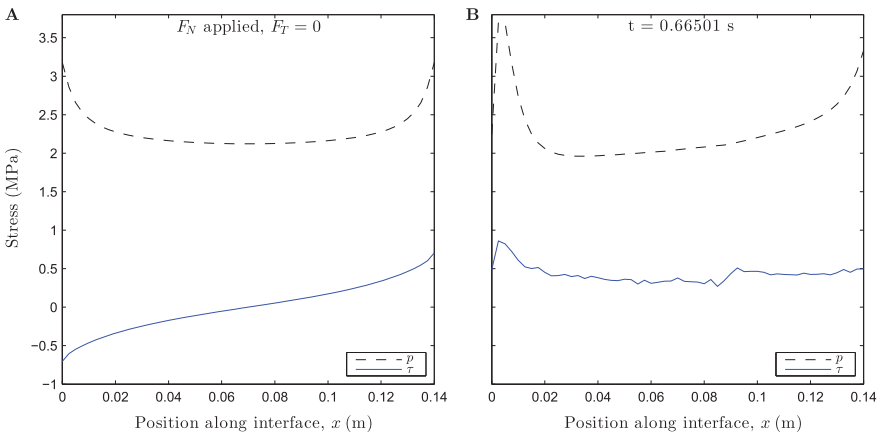

Fig. S1. Spatial distributions of normal (p) and shear (τ) stresses from the simulation behind events I–III. (*A*) The initial state with full normal load F_N and no tangential load F_T (*SI Methods*). The normal stress $p(x)$ is symmetric, with edge effects related to the flat punch geometry of the contact. The shear stress $\tau(x)$ is antisymmetric, due to Poisson expansion being restricted at the interface by friction. (*B*) The state just before event I. The application of F_T has modified both the shear stress profile and the normal stress profile (due to the friction-induced torque arising when F_T is applied at a finite height h above the interface).

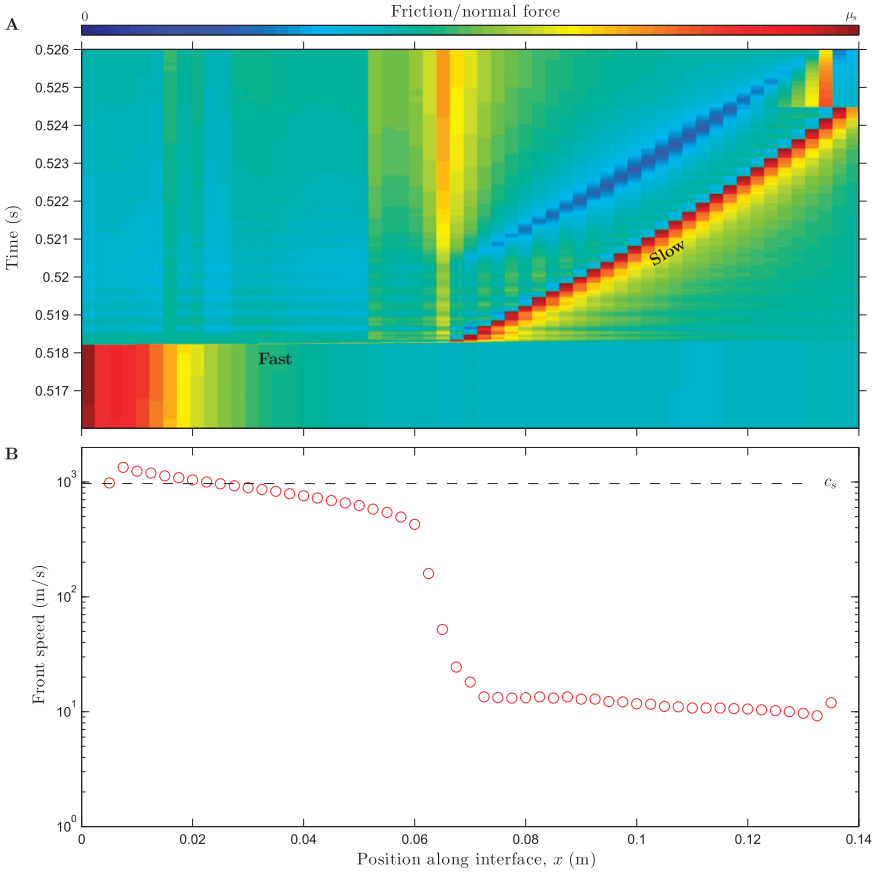

Fig. S2. A fast–slow event arising spontaneously in a simulation using the simplified friction law with a single interface spring per block. The parameter $v_{\text{slow slip spring}} = 1.5$ mm/s (*SI Methods*). (*A*) Spatiotemporal plot of the instantaneous friction to normal force ratio. (*B*) Rupture front speed v_c. Block rupture is defined to occur when the interface spring depins. Front speed is measured as in Fig. 2.

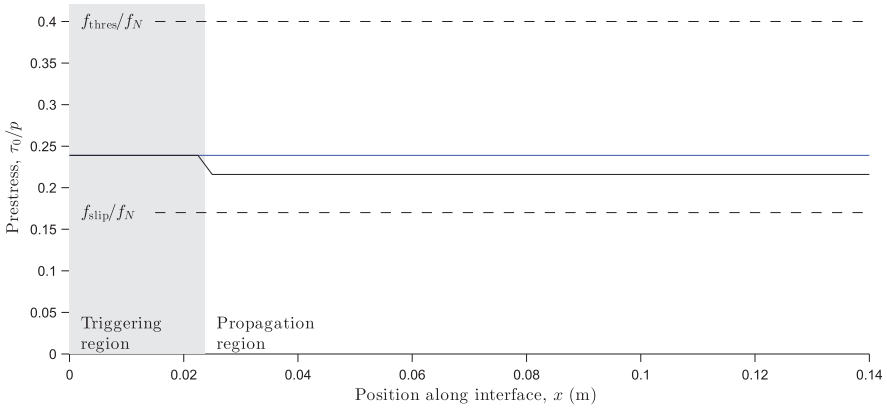

Fig. S3. Spatial distributions of prestress τ_0/p for prepared states of the interface. In the front triggering region on the left, the prestress is $\overline{\tau}_0 = ((\tau_0/p) - (f_{\text{slip}}/f_N))/((f_{\text{thres}}/f_N) - (f_{\text{slip}}/f_N)) = 0.3$ for all prepared states used in Figs. 3*D* and 4 *C* and *D*. In the front propagation region, the prestress is homogeneous along the interface, at a value varied between prepared states, here $\overline{\tau}_0 = 0.2$ (black) and $\overline{\tau}_0 = 0.3$ (blue). After initialization, all springs in the triggering region are depinned simultaneously. Initiating the events in this way, rather than by driving the system until rupture is triggered, ensures that the force drop/energy release in the triggering region remains the same between simulations. The nondimensional form $\overline{\tau}_0$ of the prestress represents the ratio between (*i*) the stress in excess of the stress obtained during sliding and (*ii*) the maximum dynamic stress drop that results from rupture. It is analogous to the so-called *S* classically used in seismology and to the form defined in ref. 1.

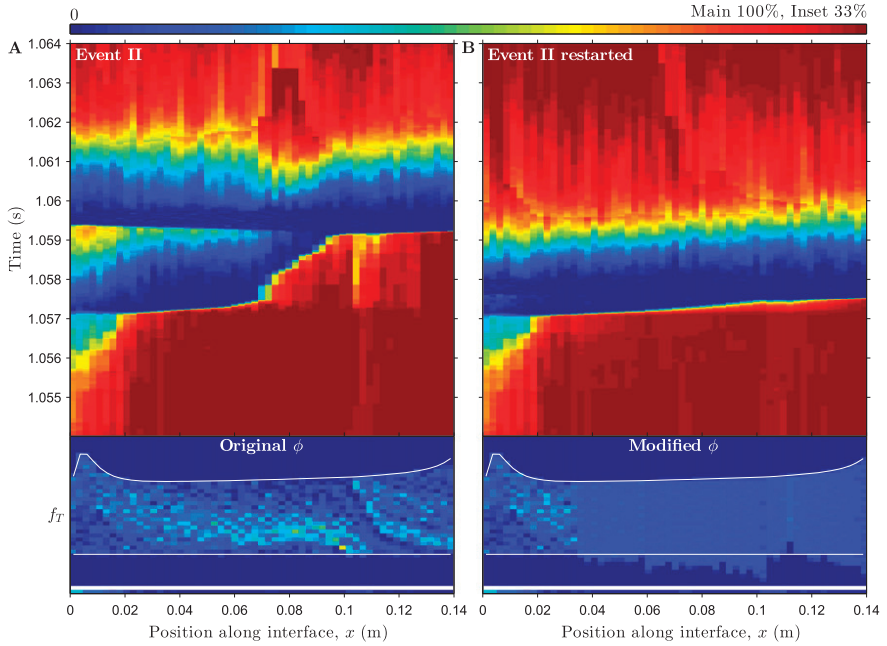

Fig. S4. Microscopic force distributions significantly affect rupture fronts. The data in Fig. 4 *A* and *B* repeated with spring force distributions shown in detail. (*A*) Event II shown as in Fig. 2. (*B*) Simulation behind *A* restarted at 1.054 s with a wider distribution $\phi(f_T)$ of shear forces results in a fast-only event. To isolate the effect of $\phi(f_T)$ on front propagation from the influence of front initiation and stress state we leave the loading zone on the left unmodified (it is the same in both *Insets*) so that the restarted event begins like the original. We also let the modified $\phi(f_T)$ have the same mean value as the original $\phi(f_T)$ for all blocks. Thus, the stress state is the same and the only change is in the width of ϕ. (*Insets*) For each block along the interface, a color-coded histogram of $\phi(f_T)$ at 1.054 s. The vertical axis shows the force level in individual springs, which extends up to f_{thres}. The level f_{thres} is shown by the upper white line; it is different for each block because it varies with normal force. The lower white line corresponds to $f_T = 0$ N. Color denotes the fraction of springs found at each value of f_T using an arbitrary bin width. This means that (apart from normalization) each vertical slice in the *Insets* shows the same type of data as Fig. S5*A*. Offset data represents the fraction of slipping springs at 1.054 s.

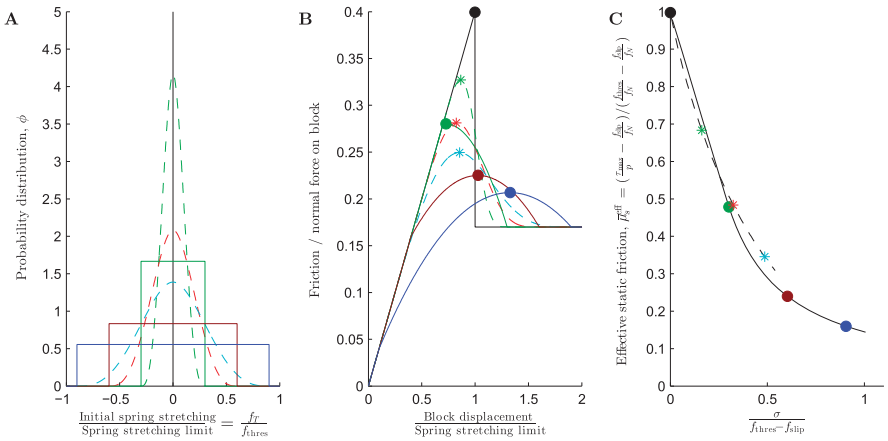

Fig. S5. Dependence of effective static friction coefficient $\mu_s^{\text{eff}} = \tau_{\text{max}}/p$ on the distribution ϕ of forces in the interface springs. (*A*) Uniform and bell-shaped initial distributions of various widths. The bell-shaped distributions are polynomials with roots at $\pm a$ and the functional form $\phi(\xi) = 5/(4a)(1+3|\xi/a|)(1-|\xi/a|)^3, \xi \in [-a,a]$. (*B*) Friction to normal force ratio vs. block displacement for a block having the spring force distributions in *A* (corresponding colors). Spring relaxation during slip is excluded from the calculation, a valid assumption when the passage of the rupture front is quick compared with the mean slipping time $\langle t_R \rangle$. Markers are located at maxima, which define τ_{max}/p. (*C*) Effective static friction coefficient vs. σ, the standard deviation of ϕ. Each marker takes its abscissa from the data in *A* and its ordinate from *B*. Continuous and dashed lines connect markers corresponding to uniform and bell-shaped ϕ, respectively. They are used in Fig. 4*C* as reference lines for simulation data. For clarity, only a few of the ϕ that were used to determine the lines are shown on this figure. The form $\overline{\mu}_s^{\text{eff}}$ is analogous to $\overline{\tau}_0$ introduced in Fig. S3, and represents the ratio of (*i*) the dynamic stress drop from the effective static friction level to the stress obtained during sliding and (*ii*) the maximum value this stress drop can attain.

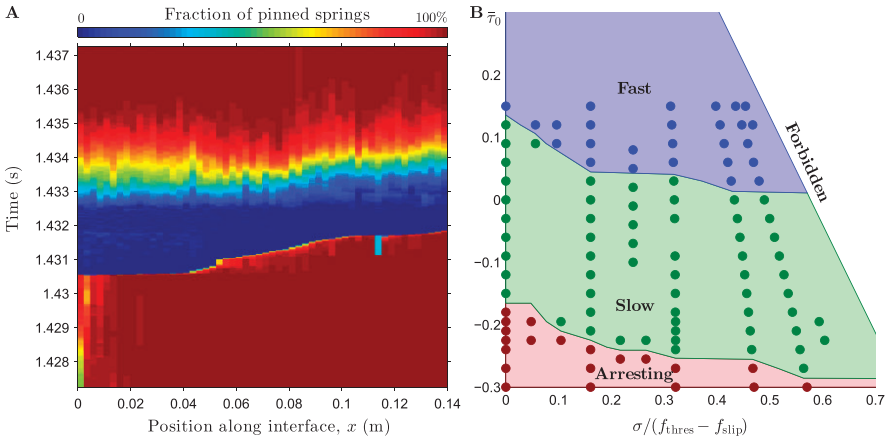

Fig. S6. Results from an alternative model with a different individual behavior of the interface springs, showing the robustness of our results against changes in the interfacial law. (*A*) A spontaneously arising fast–slow–fast event, analogous to that in Fig. 2*A*. (*B*) Observed front type for prepared interfaces, analogous to Fig. 4*D*. All data in this figure come from simulations with a model in which the slipping force f_{slip} decreases linearly with time. This microscopic friction law modifies the slow slip mechanism with respect to the reference microscopic model. Until depinning, the springs have the same behavior in both models. Upon entering the slipping state, the force from each spring on the block immediately drops to the level $f_{\text{slip}}^0 = \mu_d f_{N,ij}$, as in the reference model. Then the slipping force decays linearly in time with a decay rate depending on the slipping time and the force level at repinning f_{new}; that is, $f_{\text{slip}} = f_{\text{slip}}^0 - (f_{\text{slip}}^0 - f_{\text{new}})t_s/t_R$, with t_s measured from the time the spring entered the slipping state. The slipping time distribution is the same as in the reference model. The decay in the friction coefficient enables a slow slip motion after the initial rapid slip, which allows this model to sustain slow fronts for a relatively wide range of initial spring stretching configurations and stress states, as seen in *B*. The parameters used with this model are the same as in the reference model (Table S1), except for $k_{ij} = \sqrt{54.1\ \text{GN/m}^2 f_{N,ij}}$, $\mu_d = 0.28$ and the new parameter $\mu_{\text{new}} = 0.7\mu_d \approx 0.2$ used to determine $f_{\text{new}} = \mu_{\text{new}} f_{N,ij}$.

Table S1. Model parameters

Name	Symbol	Value
Slider, mm		
Length, x	L	140
Height, z	H	75
Width, y	B	6
No. of blocks	N_x	57
	N_z	31
Slider mass, g	M	75.6
Block mass	m	$M/(N_xN_z)$
Young's modulus, GPa	E	3
Bulk spring modulus	k	$3BE/4$
Bulk spring length	l	$L/(N_x-1)=H/(N_z-1)$
Damping coefficient	η	$\sqrt{0.1km}$
Normal load, N	F_N	1,920
Elastic foundation modulus	k_f	$k/2$
Driving		
Spring modulus, MN/m	K	4
Height, mm	h	5
Speed, mm/s	V	0.4
Threshold force coefficient	$\mu_s=f_{\text{thres}}/f_N$	0.4
Slipping force coefficient	$\mu_d=f_{\text{slip}}/f_N$	0.17
No. of interface springs per block	N_s	100
Interface spring stiffness	k_{ij}	$\sqrt{39.2\ \text{GN/m}^2 f_{N,ij}}$
Slipping time, ms		
Mean	$\bar{t}_R$	2
Standard deviation, ms	δt_R	0.6
Triggering region width, mm	x_{trigger}	22.5
Triggering region prestress	$\bar{\tau}_{\text{trigger}}$	0.3
Time step duration, s	Δt	2×10^{-7}
Extra damping coefficient	α	$\eta/40$

Parameters above the empty row (from slider length to driving speed inclusive) are used in the same way as in ref. 1.

Paper V

Direct atomic simulations of facet formation and equilibrium shapes of SiC nanoparticles

Henrik Andersen Sveinsson, Anders Hafreager, Rajiv Kalia, Aiichiro Nakano, Priya Vashishta, Anders Malthe-Sørenssen

In review in *Crystal Growth and Design*

Direct atomic simulations of facet formation and equilibrium shapes of SiC nanoparticles

Henrik Andersen Sveinsson,[†] Anders Hafreager,[†] Rajiv K. Kalia,[‡] Aiichiro Nakano,[‡] Priya Vashishta,[‡] and Anders Malthe-Sørenssen[*,†]

[†]*Njord Center, Department of Physics, University of Oslo, Sem Slands vei 24, NO-0316, Oslo, Norway*

[‡]*Collaboratory for Advanced Computing and Simulations, University of Southern California, Los Angeles, CA 90089-0241, USA*

E-mail: malthe@fys.uio.no

Abstract

Understanding the shapes of nanoparticles is an important interdisciplinary problem because particle shapes can affect their properties, functionality and applications. Advances in nanoscale imaging probes have revealed exquisite details of nano-faceting phenomena. However, quantitative theoretical predictions have not kept up pace with experimental advances, and the atomic pathways of facet formation are largely unknown due to a lack of direct observations and simulations. Here we examine facet formation in spherical and cubic SiC nanoparticles and in SiC nanowires using molecular dynamics simulations reaching microseconds. We characterize layer-by-layer formation, diffusional motion along edges and corners, and determine energy barriers. We find that the equilibrium shapes are identical regardless of the initial shape of SiC nanoparticles or nanowires. For spherical and cubic nanoparticles, (110) facets form within 10 ns by lateral liquid-like diffusion of atoms. In contrast, faceting in SiC nanowires also involves normal diffusional motion with a higher energy barrier and hence much longer faceting times. These results have important implications for molecular-level understanding of the synthesis and stability of ceramic nanocrystals and nanowires.

Introduction

Ceramic nanocrystals such as SiC are widely used in electronics,[1] photonics,[2] biosensors, drug delivery[3,4] and in structural applications.[5] The shape of nanocrystals directly affect their propeties,[6–9] but despite advances in nanoscale imaging[10–14] and modeling, the detailed atomic mechanisms of nanocrystal formation has not been directly observed in experiments or simulation.[10,15,16] The transformation of a crystalline particle from any initial shape to its equilibrium crystal shape involves a series of complex processes.[17–20] The final equilibrium shape has facets resulting from the minimization of surface free energy for a given volume.[21] The equilibrium shape of a nanocrystal is uniquely determined by the Wulff construction[22] according to the surface free energy associated with all crystal directions, resulting in certain planes being preferred. For instance, the expected equilibrium shape for a crystal with (110) planes having the lowest surface energy is a rhombic dodecahedron, possibly truncated by other facets if they have sufficiently low surface energy to intersect at the edges or corners. At finite temperature, a facet can grow either in the lateral or normal direction via the formation of steps and kinks. The latter results from the diffusion of adatoms from edges and corners.[23] The edges and corners between facets

can become rounded, but the dominant facets remain intact.[24]

The formation of a fully-grown step or layer may require multiple events to occur, and involve energy barriers that prevent the particle from reaching its equilibrium shape if the surface area of the facet is sufficiently large.[25,26] In the absence of step-producing defects, Mullins[26] has shown that the nucleation energy for growing layers on a facet is prohibitively large and the particle may become kinetically immobilized if the facet is larger than a nanometer. However, the detailed atomic mechanisms of facet formation in nanocrystals have not yet been observed experimentally or computationally.

Results and Discussion

Here we examine how volume-preserving spherical, cubic and cylindrical silicon carbide nanoparticles reach the same equilibrium shape by different dynamical mechanisms, crossing significantly different energy barriers over time scales varying by three orders of magnitude. Figure 1 shows how a (110) facet forms in an SiC particle that was initially a sphere of diameter 8 nm. Figure 1(a) shows the onset of facet formation in the spherical SiC nanoparticle at $T = 2,200$K after 0.02 ns. The different colors indicate the layer depth: atoms in the first five layers from the top are colored blue, red, yellow, purple and green. In the early stages, Si and C atoms diffuse in these layers to expose (110) facets. The diffusion coefficients for Si and C atoms in the early stages of facet formation are close to 7×10^{-6}cm^2/s and 1.0×10^{-5} cm^2/s, respectively. Figures 1(d) and (e) indicate that the participation of the topmost layer (green) in the facet growth ceases after a short duration of less than 10 ns. The snapshot in Fig. 1(b) shows partial formation of a (110) facet after 139 ns. Atoms in the second layer (purple) participate in the facet growth for another 125 ns and subsequently their participation tails off to zero after 265 ns. These atoms are mostly in the central part of the facet, and they are surrounded by atoms in the third layer. Atoms in the bottom two layers (red and blue) participate in the edges between facets. The snapshot in Fig. 1(c) shows a fully grown (110) facet after 400 ns. Atoms in the bottom two layers (blue and red) continue to diffuse, mostly at the edges and corners of the facet, even after the facet growth stops. The participation of atoms from the bottom three layers remains nearly constant over the entire duration of the facet formation, see Fig. 1(e). After 400 ns, the SiC nanoparticle is transformed from a sphere to faceted nanocrystal with twelve (110) and eight (111) facets. Between the facets, there are edges and corners along which surface Si and C diffuse with diffusion constants around $3.1(2) \times 10^{-6}$ cm^2/s and $4.4(3) \times 10^{-6}$ cm^2/s, respectively.

To examine the effect of the initial nanocrystal shape, we also simulated a cubic nanocrystal with length 8 nm and faces in the (001) directions, and a cylindrical nanocrystal of diameter 4 nm and length 8 nm along the [011] crystal direction. These were also performed at $T = 2,200$K. The particle shapes are nearly identical for the sphere and the cube after 1 μs, but the cylindrical particle differs. Figure 2 shows the initial shapes (a-c), final shapes (d-f) and the fraction of the surface area being (110) or (111) facets (g) for the sphere, the cube and the cylinder. Just like the sphere, the cube transforms into a nanocrystal with twelve (110) and eight (111) facets. In Figure 2(g) we use the facet area fraction as an indication of the facet formation. We observe that this fraction stabilizes in 0.1 μ for the cube and 0.6 μ for the sphere. The cylindrical nanoparticle also develops (110) and (111) facets, and its facet area fraction stabilizes after 0.3 μ, but the shape of this nanoparticle is different from the other ones even after 1 μ. Note that the faceting times are not directly comparable since the nanoparticles have different volumes.

To investigate the faceting of the cylindrical nanocrystal in more detail, we plot the distance between opposing (110) planes. This, along with snapshots of the particle at various stages of the facet formation is shown in Figure 3. We again observe the initial faceting phase of 0.3 μs. During this time, pairs of facets inclined

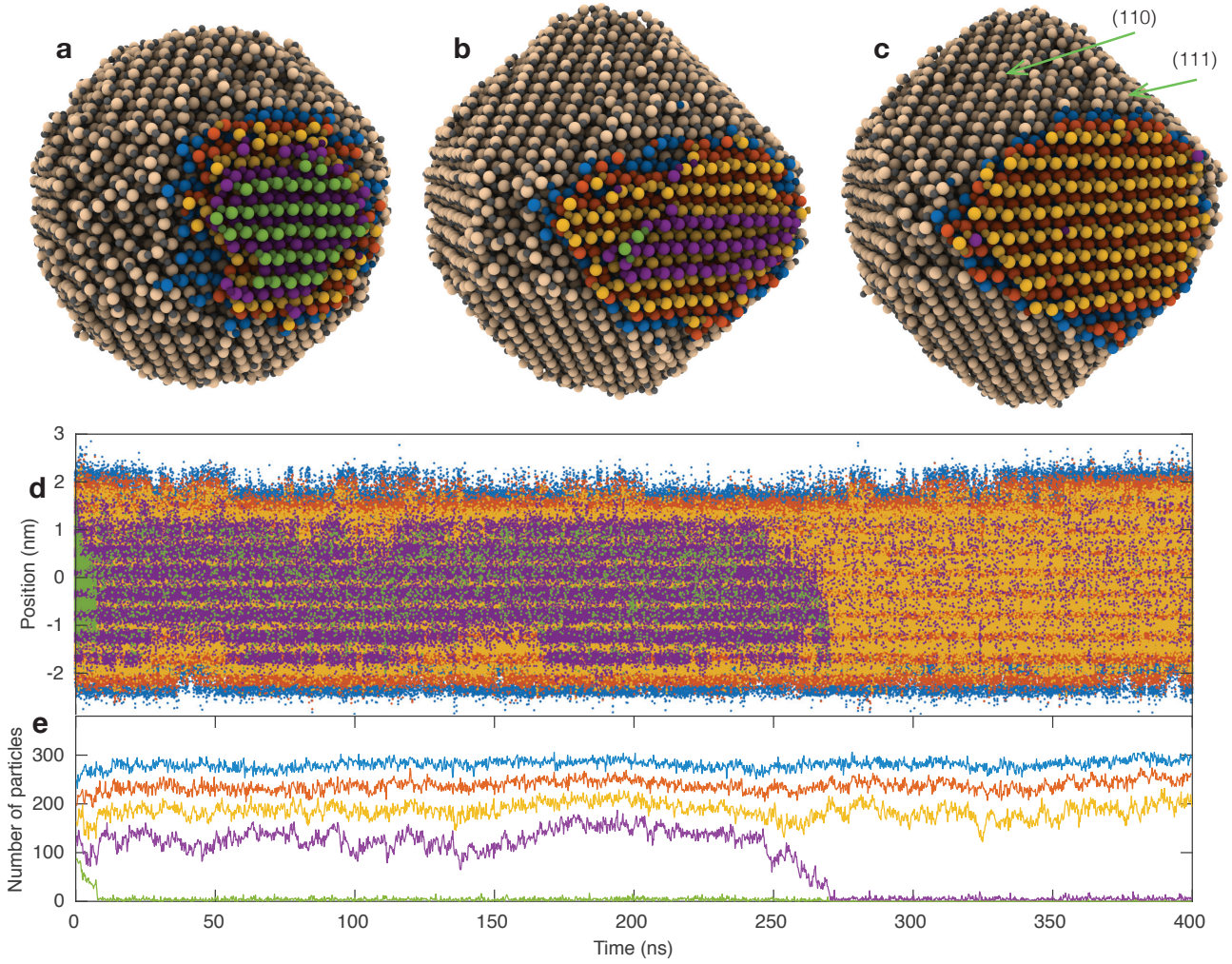

Figure 1: Faceting of silicon carbide nanoparticles. (a-c) Snapshots of silicon carbide nanoparticle (n-SiC) with diameter 8 nm faceting during a molecular dynamics simulation. (a) Initial configuration taken at 0.02 ns, (b) partly faceted particle after 139 ns and (c) fully faceted particle after 400 ns. In (b) and (c) we see (110) facets, and also island-like (111) facets. In the final configuration, the mean distance from the center of the particle to the (110) planes is 3.73 nm and to the (111) plane 3.90 nm, which by Wulff construction gives the ratio of surface energies $E_{110}/E_{111} = 0.956$, and that the equilibrium shape is a rhombic dodecahedron truncated by a regular octahedron. Colours in (a-c) indicate layer depth on one of the (110) facets, and correspond to the colours in (d-e). (d) scatters the height distribution of particles in the 5 top layers of the crystal through time, and shows that the interplay between rows on the facet is important in the faceting process. (e) shows the numbers of particles in each layer of the coloured facet through time, and guides the interpretation of (d).

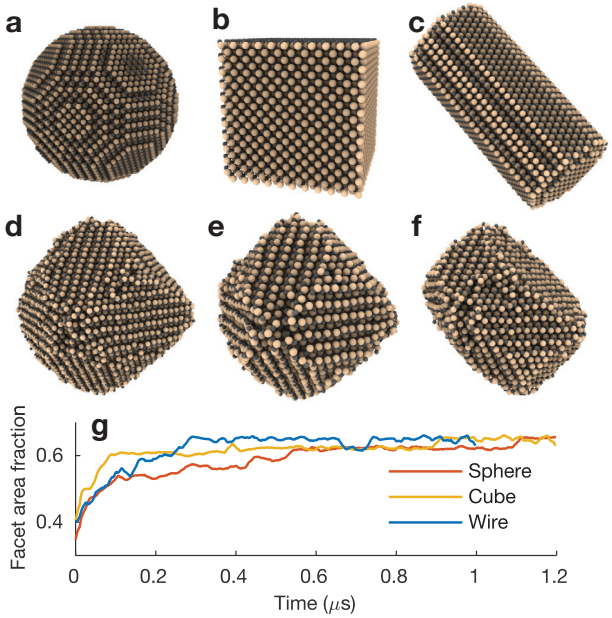

Figure 2: Effects of changing the initial shape of n-SiC. A spherical particle (a) and a cubic particle (b) facets to the same shape (d-e), during simulation at 2200 K. A cylindrical particle (c) does not reach the same shape, and is locked into a metastable shape (f). (g) shows the evolution of the sum of the (110) and (111) facet area through time, and shows that all particles have reached a steady state during the simulation time.

with respect to the major axis move closer to each other, reaching approximately the same value (5.5 nm) after 0.1 μs. The planes normal to the major axis converge to a higher separation distance (6.3 nm) after 0.3 μs. However, the distance between the facet pair parallel to the major axis remains constant through 1 μs at 2,200 K. These are the largest facets. The volume freed by facet pairs only moving towards each other is taken up as lateral growth of facets, ultimately resulting in the formation of corners. Lateral movement and facet area growth results in the formation of two relatively sharp (100) corners, which can be seen in the snapshot after 1 μs.

The oblate shape of the nanocrystal has to be metastable because it is asymmetric in the (110) planes. In order to kick the system out of its metastable shape, the temperature is raised to 2,361 K to see whether it reaches the equilibrium shape. This heating causes shape-change, as can be seen in the shaded part of Figure 3. After 200 ns at 2,361 K, all facet pairs converge to same separation distance, and the particles reach the equilibrium shape. The dark blue facet pair takes about 0.2 μs before it also converges to the same separation distance 5.5 nm. The nanocrystal shape is monitored for 0.6 μs at 2,361 K, and we do not observe any changes in the shape of the nanocrystal. The final shape resembles the final shapes of nanocrystals with spherical and cubic initial configurations.

The oblate shape is metastable due to an energy barrier to the normal motion of sufficiently large facets. To estimate the magnitude of this barrier, we measure the growth rate in 63 simulations at varying temperatures between 2275 K and 2385 K. These simulations were run between 200 and 500 ns depending on the time needed to grow new layers. We monitor the time dependence of the number of atoms on top of the largest (110) facet in all of these simulations to determine the nucleation time for new layers on the facet as function of layer depth and temperature. This number abruptly grows when a new layer is nucleated, so it is sharply defined. Figure 4(a-b) shows how this number develops for four layers growing in a simulation at 2295 K. Figure 4(c) shows the waiting

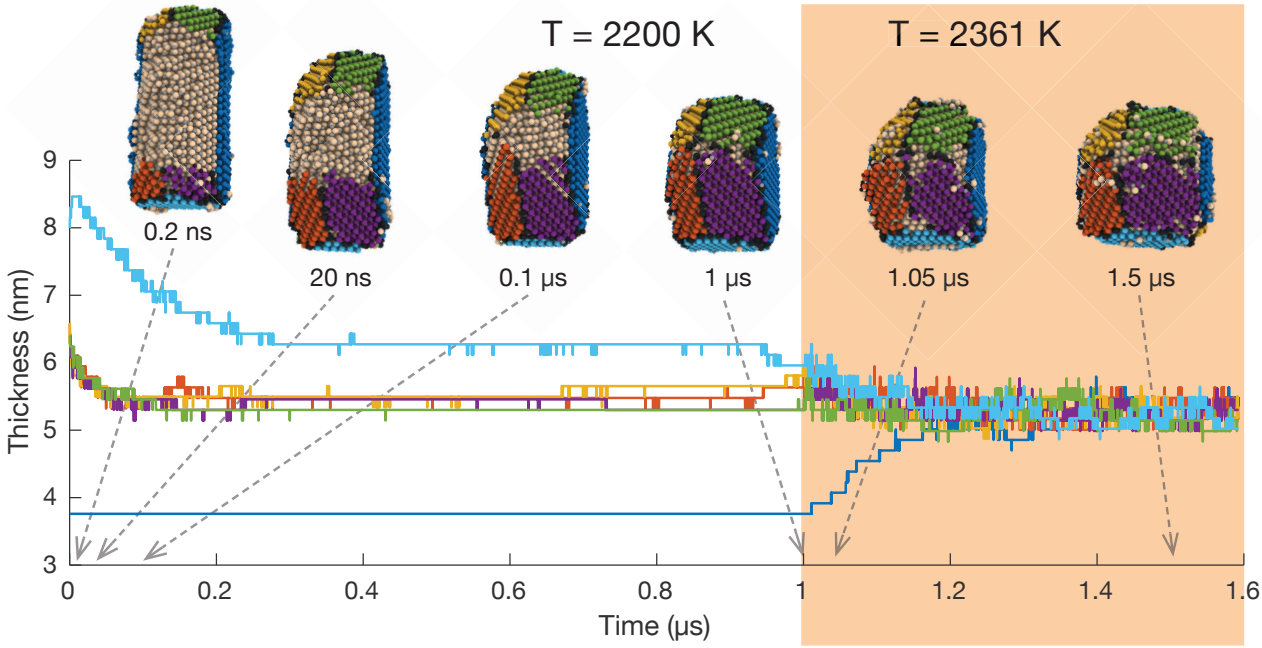

Figure 3: Distance between facet pairs. Snapshots of (110) facets in different directions during a simulation taken at 0.2 ns, 20 ns, 0.1 μs, 1.05 μs and 1.5 μs. Lines show the distance between opposing facets, and line colours correspond to the colours indicated on the snapshots. The lines are step-like because the removal or addition of a layer results in a discontinuous change in the distance between facets. During the first 1 μs of the simulation the distance between most facet pairs decreases, but for the major facet pair (dark blue) we do not observe any layer growth nor shrinking, although their areas have increased. Upon heating, new layers grow on the major (110) facet, and the particle reaches its equilibrium shape. The distance between the major planes is constant throughout the first 1 μs, whereas both the cap plane distance and the minor facet distance are decreasing. In the final state, the distance between all pairs of parallel facets converge to the same value. The yellow, green, red and purple facets are the inclined, the light blue are the normal and the dark blue are the parallel facets with respect to the cylinder major axis.

times for a single layer height for all simulations. From this Arrhenius plot, we estimate the energy barrier for each layer height; see Figure 4(d). This barrier is estimated to 14 eV for the first four layer heights on top of the metastable oblate shape.

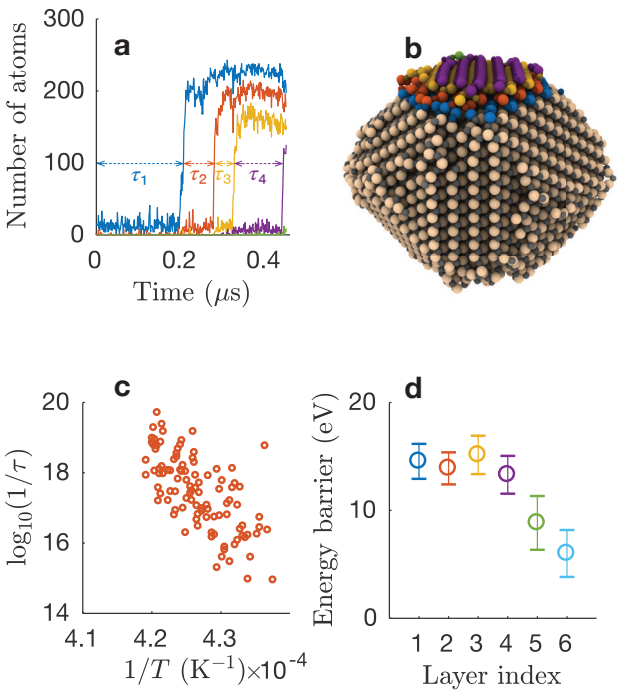

Figure 4: Facet layer growth on the major (110) plane of heated metastable silicon carbide nanoparticles. (a) Layer growth, i.e. the number of atoms, in the first four layers after heating the metastable particle achieved after 1 μs at $T = 2200$ K to $T = 2295$ K. The waiting times $\tau_1, \ldots, \tau_4$ for the four layers are indicated in the figure. The colours in (a) correspond to the layers indicated in (b). (c) $\log(1/\tau)$ vs. $1/T$ gives the Arrhenius plot for the growth of the second (red) layer. Each marker in (c) corresponds to a full simulation of 200-500 ns. A linear fit to this Arrhenius plot gives the energy barrier for the second layer. Following the same procedure, we obtain the energy barrier for layer formation for the first six layers (d). Error bars in (d) indicate 67% confidence bounds of linear fits to Arrhenius plots.

Conclusions

This study demonstrates that processes such as faceting and crystal growth can be within the reach of microsecond molecular dynamics simulations. Here, we have provided insights into the detailed faceting mechanisms of SiC. The results and methods are of general importance in the synthesis of nanocrystals and nanowires. Other materials and processes should be studied using similar approaches to gain insight into what mechanisms are general and what are specific to SiC. Molecular dynamics studies of faceting also open up more detailed studies of crystal growth procedures and how they are related to the resulting nanocrystal geometry,[10,15] and to address competing processes between crystal growth and deformation during healing and recrystallization.

Methods

SiC-3C was prepared with a lattice constant of 4.358 . To prepare initial nanocrystals, we created a block of bulk SiC-3C in a cubic simulation box of (40 nm)3 (sphere), (30 nm)3 (cube) or (23.4 nm)3 (cylinder), and then deleted atoms that were outside the region defined by the geometrical shape of that initial nanocrystal. This method can lead to non-stoichiometry, which we amended by adding particles to the void to regain stoichiometry. We used a force field consisting of two-body and three-body terms.[27] All simulations were run with periodic boundary conditions using a NVT NosHoover thermostat with a damping time of 1 ps. Equations of motion were integrated with the Velocity Verlet scheme using a timestep of 2 fs. The simulation box sizes were such that the nanocrystal didnt interact with its periodic image. All simulations were run on NVIDIA P100 computing cards using the GPU package in LAMMPS.[28] Diffusion coefficients were calculated using the mean squared displacement of the top three surface layers over 100 ps.

Acknowledgement R.K., A.N. and P.V. were supported by the U.S. Department of Energy, Office of Science, Basic Energy Sciences,

100

Materials Science and Engineering Division, Grant DE-SC0018195. The simulations were performed at the Argonne Leadership Computing Facility under the DOE INCITE program, at the Center for High Performance Computing of the University of Southern California, and at the University of Oslo. Researcher exchange was financed by the Norwegian Research Council.

Supporting Information Available: Brief descriptions of how the energy barriers for normal growth on facets were measured, and details of facet evolution on cylindrical n-SiC. This material is available free of charge via the Internet at `http://pubs.acs.org/`.

References

(1) Capano, M. A.; Trew, R. J. Silicon Carbide Electronic Materials and Devices. *MRS Bulletin* **1997**, *22*, 19–23.

(2) Song, B.-S.; Yamada, S.; Asano, T.; Noda, S. Demonstration of two-dimensional photonic crystals based on silicon carbide. *Optics Express* **2011**, *19*, 11084–11089.

(3) Yakimova, R.; Jr, R. M. P.; Yazdi, G. R.; Vahlberg, C.; Spetz, A. L.; Uvdal, K. Surface functionalization and biomedical applications based on SiC. *Journal of Physics D: Applied Physics* **2007**, *40*, 6435.

(4) Saddow, S. E. In *Silicon Carbide Biotechnology (Second Edition)*; Saddow, S. E., Ed.; Elsevier, 2016; pp 1–25.

(5) Zhao, J.-C.; Westbrook, J. H. Ultrahigh-Temperature Materials for Jet Engines. *MRS Bulletin* **2003**, *28*, 622–630.

(6) Kinnear, C.; Moore, T. L.; Rodriguez-Lorenzo, L.; Rothen-Rutishauser, B.; Petri-Fink, A. Form Follows Function: Nanoparticle Shape and Its Implications for Nanomedicine. *Chemical Reviews* **2017**, *117*, 11476–11521.

(7) Murphy, C. J.; Sau, T. K.; Gole, A. M.; Orendorff, C. J.; Gao, J.; Gou, L.; Hunyadi, S. E.; Li, T. Anisotropic Metal Nanoparticles: Synthesis, Assembly, and Optical Applications. *The Journal of Physical Chemistry B* **2005**, *109*, 13857–13870.

(8) Bruchez, M.; Moronne, M.; Gin, P.; Weiss, S.; Alivisatos, A. P. Semiconductor Nanocrystals as Fluorescent Biological Labels. *Science* **1998**, *281*, 2013–2016.

(9) Burda, C.; Chen, X.; Narayanan, R.; El-Sayed, M. A. Chemistry and Properties of Nanocrystals of Different Shapes. *Chemical Reviews* **2005**, *105*, 1025–1102.

(10) Liao, H.-G.; Zherebetskyy, D.; Xin, H.; Czarnik, C.; Ercius, P.; Elmlund, H.; Pan, M.; Wang, L.-W.; Zheng, H. Facet development during platinum nanocube growth. *Science* **2014**, *345*, 916–919.

(11) Hansen, P. L.; Wagner, J. B.; Helveg, S.; Rostrup-Nielsen, J. R.; Clausen, B. S.; Topse, H. Atom-Resolved Imaging of Dynamic Shape Changes in Supported Copper Nanocrystals. *Science* **2002**, *295*, 2053–2055.

(12) Zheng, H.; Smith, R. K.; Jun, Y.-w.; Kisielowski, C.; Dahmen, U.; Alivisatos, A. P. Observation of Single Colloidal Platinum Nanocrystal Growth Trajectories. *Science* **2009**, *324*, 1309–1312.

(13) Evans, J. E.; Jungjohann, K. L.; Browning, N. D.; Arslan, I. Controlled Growth of Nanoparticles from Solution with In Situ Liquid Transmission Electron Microscopy. *Nano Letters* **2011**, *11*, 2809–2813.

(14) Fei, L.; Ng, S. M.; Lu, W.; Xu, M.; Shu, L.; Zhang, W.-B.; Yong, Z.; Sun, T.; Lam, C. H.; Leung, C. W.; Mak, C. L.; Wang, Y. Atomic-Scale Mechanism on Nucleation and Growth of Mo2C Nanoparticles Revealed by in Situ Transmission Electron Microscopy. *Nano Letters* **2016**, *16*, 7875–7881.

(15) Fichthorn, K. A.; Balankura, T.; Qi, X. Multi-scale theory and simulation of shape-selective nanocrystal growth. *CrystEngComm* **2016**, *18*, 5410–5417.

(16) Sawada, K.; Iwata, J.-I.; Oshiyama, A. Magic angle and height quantization in nanofacets on SiC(0001) surfaces. *Applied Physics Letters* **2014**, *104*, 051605.

(17) Herring, C. Some Theorems on the Free Energies of Crystal Surfaces. *Physical Review* **1951**, *82*, 87–93.

(18) Einstein, T. L. In *Handbook of Crystal Growth (Second Edition)*; Nishinaga, T., Ed.; Elsevier: Boston, 2015; pp 215–264.

(19) Kitayama, M.; Narushima, T.; Carter, W. C.; Cannon, R. M.; Glaeser, A. M. The Wulff Shape of Alumina: I, Modeling the Kinetics of Morphological Evolution. *Journal of the American Ceramic Society* **2000**, *83*, 2561–2531.

(20) Ozdemir, M.; Zangwill, A. Morphological equilibration of a facetted crystal. *Physical Review B* **1992**, *45*, 3718–3729.

(21) Gibbs, J. W. *The Collected Works of J. Willard Gibbs*; Yale University Press, 1948; Google-Books-ID: SvQyAQAAIAAJ.

(22) Wulff, G. Zur Frage der Geschwindigkeit des Wachstums und der Auflsung der Krystallflagen. *Zeitschrift fr Krystallographie und Mineralogie* **1901**, *34*, 449–530.

(23) Pimpinelli, A.; Villain, J. *Physics of Crystal Growth by Alberto Pimpinelli*; Cambridge Core - Statistical Physics; Cambridge University Press, 1998.

(24) Rottman, C.; Wortis, M. Statistical mechanics of equilibrium crystal shapes: Interfacial phase diagrams and phase transitions. *Physics Reports* **1984**, *103*, 59–79.

(25) Mullins, W. W.; Rohrer, G. S. Nucleation Barrier for Volume-Conserving Shape Changes of Faceted Crystals. *Journal of the American Ceramic Society* **2000**, *83*, 214–16.

(26) Rohrer, G. S.; Rohrer, C. L.; Mullins, W. W. Nucleation Energy Barriers for Volume-Conserving Shape Changes of Crystals with Nonequilibrium Morphologies. *Journal of the American Ceramic Society* **2001**, *84*, 2099–2104.

(27) Vashishta, P.; Kalia, R. K.; Nakano, A.; Rino, J. P. Interaction potential for silicon carbide: A molecular dynamics study of elastic constants and vibrational density of states for crystalline and amorphous silicon carbide. *Journal of Applied Physics* **2007**, *101*, 103515.

(28) Plimpton, S. Fast Parallel Algorithms for Short-Range Molecular Dynamics. *Journal of Computational Physics* **1995**, *117*, 1–19.

Supporting Information for Direct atomic simulations of facet formation and equilibrium shapes of SiC nanoparticles

Henrik Andersen Sveinsson,[†] Anders Hafreager,[†] Rajiv K. Kalia,[‡] Aiichiro Nakano,[‡] Priya Vashishta,[‡] and Anders Malthe-Sørenssen[*,†]

[†]*Njord Center, Department of Physics, University of Oslo, Sem Slands vei 24, NO-0316, Oslo, Norway*

[‡]*Collaboratory for Advanced Computing and Simulations, University of Southern California, Los Angeles, CA 90089-0241, USA*

E-mail: malthe@fys.uio.no

Measuring the energy barrier for normal growth on facets

To quantify the energy barrier for normal growth on the major facets, we performed 62 simulations at higher temperatures continuing from the metastable shape achieved after 1 s at 2200 K to collect statistics on the layer growth process over the subsequent 0.2 μs to 0.5 μs in the temperature range 2275 K2385 K. We measured the waiting time for each new layer to grow on the major facets as a function of temperature (Figure 4a). We performed an additional 57 simulations at 2360 K with random initial velocities to demonstrate that the waiting time was exponentially distributed. This validates the use of Arrhenius equation to calculate the energy barrier. Figure 4c is an Arrhenius plot of the layer growth waiting times as a function of system temperature. The rate $(1/\tau)$ in the Arrhenius plot shows a

linear dependency with a slope that is proportional to the energy barrier E_b. We find an energy barrier of 15 eV for the first four layers on the facet. We estimate the energy barrier to be 0.5 eV per atom by dividing the 15 eV by the maximum number of atoms on the top layer during an unsuccessful attempt to grow a layer, which is a reasonable estimate for the number of atoms on the newly formed layer.

Supplementary material 2: Details of facet evolution on a cylindrical n-SiC

S2. Details of facet evolution on a cylindrical n-SiC

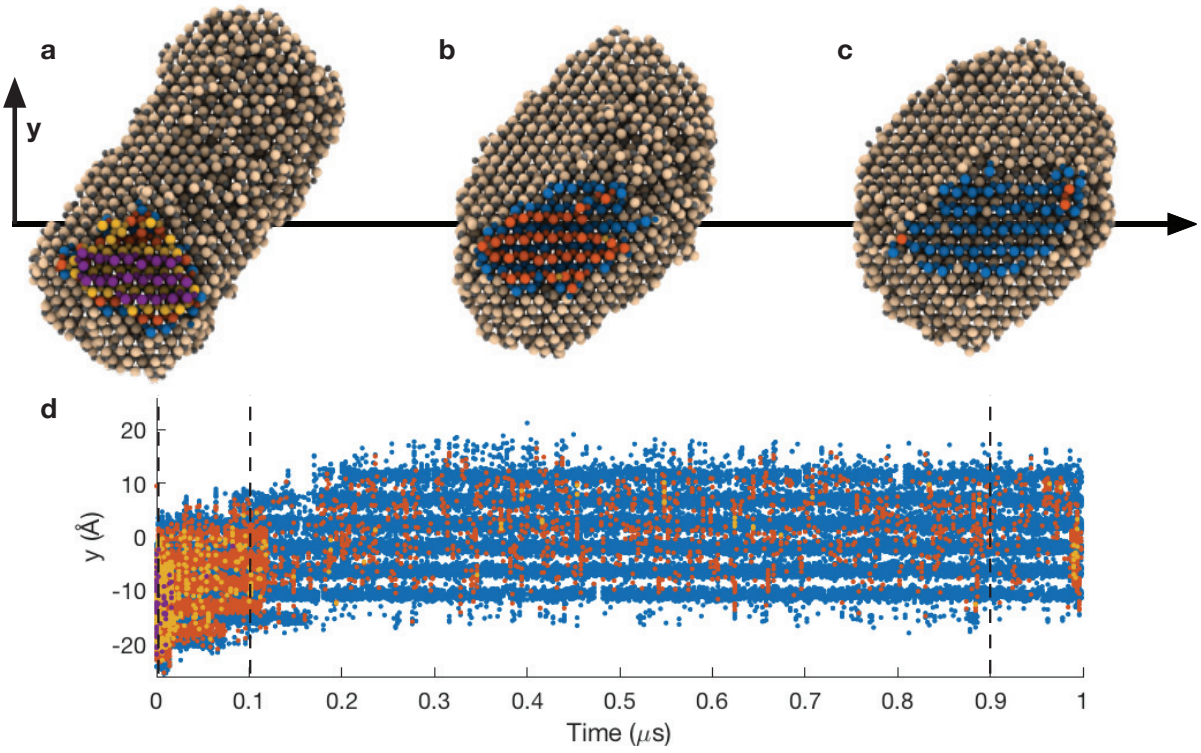

Figure S1. Facet evolution on a cylindrical n-SiC during a 1 μs simulation. (**a**) Cylindrical n-SiC after 200 ps simulation time. Coordinate system is chosen so that positive y-direction is orthogonal to the steps on the facet. Colors indicate different atomic layers normal to one of the (110) facets. (**b**) Intermediate state after 100 ns where the facet has lost all but two atomic layers. The two layers have moved in-plane by developing new steps in the positive y-direction. (**c**) Metastable state after 0.9 μs, where the (110) facet has been essentially constant for 0.7 μs. (**d**) y-coordinate of all particles on the (110) facet as a function of time. Color indicate the layer of that atom matching (**a**). Snapshot time for figures (**a**), (**b**) and (**c**) are marked as vertical dashed lines. The different rows form *bands* with edge bands being the steps on the facet. These are rather stable since removing such a step costs energy due to the creation of kinks.

S3: Row-push mechanism on (110) facet

Supplementary material 3: Row-push mechanism on (110) facet

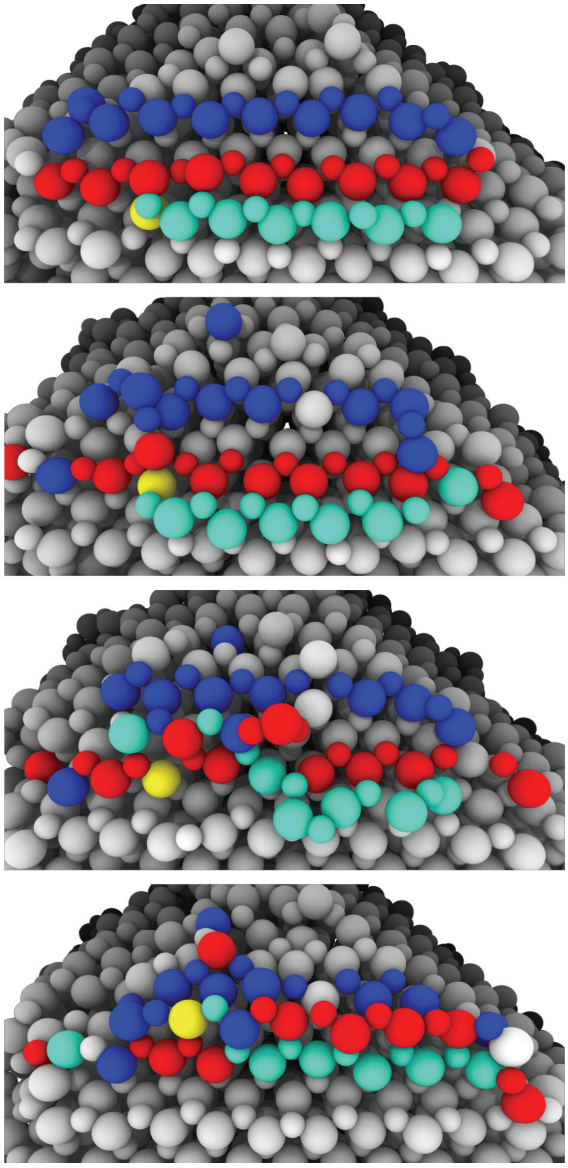

Figure S2. Row push mechanism on a (110) facet. (**a**) Configuration where two in-layer rows (red, blue) and one elevated row (cyan). (**b**) The yellow particle pushes one of the red particles out of position, and thus creates a closer connection between the red and blue rows. This connection mediates the subsequent "row-push" of red particles by cyan particles (**c-d**).

Figure 2: Row push mechanism on a (110) facet. (a) Configuration where two in-layer rows (red, blue) and one elevated row (cyan). (b) The yellow particle pushes one of the red particles out of position, and thus creates a closer connection between the red and blue rows. This connection mediates the subsequent row-push of red particles by cyan particles (c-d).